EXPERIMENTAL AND NUMERICAL STUDY OF POLYMER SCRATCH BEHAVIOR

A Dissertation

by

HAN JIANG

Submitted to the Office of Graduate Studies of
Texas A&M University
in partial fulfillment of the requirements for the degree of

DOCTOR OF PHILOSOPHY

August 2009

Major Subject: Mechanical Engineering

EXPERIMENTAL AND NUMERICAL STUDY OF POLYMER SCRATCH BEHAVIOR

A Dissertation

by

HAN JIANG

Submitted to the Office of Graduate Studies of
Texas A&M University
in partial fulfillment of the requirements for the degree of

DOCTOR OF PHILOSOPHY

Approved by:

Chair of Committee,	Hung-Jue Sue
Committee Members,	John D. Whitcomb
	Christian J. Schwartz
	Chii-Der Suh
Head of Department,	Dennis O'Neal

August 2009

Major Subject: Mechanical Engineering

ABSTRACT

Experimental and Numerical Study of Polymer Scratch Behavior. (August 2009)

Han Jiang, B.Eng., Chongqing University, P. R. China;

M. Eng., Chongqing University, P. R. China

Chair of Advisory Committee: Dr. Hung-Jue Sue

As part of a larger effort to understand the fundamental knowledge of polymer scratch behavior, this dissertation is focused on both experimental study and numerical analysis of scratch deformation of a broad range of polymers, with an emphasis on the mechanical understanding of how the scratch-induced damage is formed. An instrumented progressive load scratch method recommended by ASTM/ISO standards was adopted for the experimental work. The commercial finite element (FE) method package ABAQUS® was employed as a numerical simulation tool to describe the stress-strain fields, and it analyzes the deformation mechanisms during the scratch process. A thorough parametric study has been performed to assess the influence of material parameters and surface properties, such as Young's modulus, yield strength, and friction coefficient, on the polymer scratch behavior.

Upon investigation of the scratch behaviors of a broad range of polymer materials, various kinds of scratch damage features are identified and correlated with the mechanical characteristics of the polymers. A generalized scratch damage mechanism map for polymers is presented. Correlation between different material types and scratch

damage mechanisms is made. It is found that both the material characteristics and the stress state exerted on the scratched surface are responsible for the observed scratch damage mechanisms. The phenomenological deduction of the scratch damage process based on the stick-slip mechanism is established. A more realistic material law for the scratch analysis is also provided.

To evaluate the polymer resistance against scratch visibility quantitatively, an entirely new automated on-set scratch visibility determination methodology is developed based on typical visual characteristics of human eyes. Its application on the evaluation of mar and abrasion of polymer is also explored. This new methodology can quantify polymer scratch resistance consistently and reliably regardless of the sample surface characteristics and color.

ACKNOWLEDGEMENTS

Pursuing a degree in an American school has been the most challenging task I have ever taken by far. I dedicate this work to the following individuals who have greatly influenced my life along this journey.

I would like to thank my parents, sister and lovely wife. Their unconditional support is the reason for me to move on no matter what the circumstances are.

I would like to give my most sincere thanks to Prof. H.-J. Sue, who has provide valuable guidance and served as a role model as a person as well as a researcher, and to Prof. J.D. Whitcomb, who has patiently offered me advice in pursuing my passion for science and engineering.

I also want to extend my gratitude to Prof. C. Schwartz whose academic enthusiasm always inspired me, and to Prof. S. Suh whose encouraging words have never failed to motivate me.

Special thanks are also given to Mr. R. Browning, who has challenged me to think better and differently in life and academia, and to my fellow colleagues and friends, Dr. G.-T. Lim, Mr. E. Moghbelli, Miss Y.-S. Song and Miss A. O'Reilly who have worked with me passing through various obstacles.

Finally, thanks to professors, colleagues and friends at Texas A&M University who have shown me by example that researcher never stop learning.

TABLE OF CONTENTS

CHAPTER Page

LIST OF FIGURES

FIGURE Page

FIGURE Page

FIGURE Page

LIST OF TABLES

CHAPTER I

INTRODUCTION

In this chapter, a comprehensive review is given to highlight the importance of polymer scratch research and to review its state of the art research. Important factors and considerations are described in detail. Finally, an outline is given to describe the dissertation research focuses and their arrangement.

1.1 Background of polymer scratch research

Impressive advances toward the development of engineering polymers that meet specific long-term application requirements have been achieved by the polymer industry [1-6]. Consequently, surface quality of polymers has gained more and more attention for applications where durability is essential, such as automotive, coatings, bioengineering and optics industries. Good surface quality is one of the primary desirable attributes of most engineering polymers either for their functionality or aesthetics. A better understanding and control of the surface mechanical and tribological properties are important concerns in the use of engineering polymers.

For polymer applications, surface quality can be classified into surface aesthetics, surface integrity, and durability. Surface aesthetics are important in many areas, such as automotive parts, electronics, and telecommunication devices, where surface scratches reduce the original product attractiveness while their functionality is still generally

---

This dissertation follows the style of Applied Surface Science.

unaffected. Surface integrity can be a major concern for applications like food packaging. Scratches can cause the package to lose its functionality prematurely leading to spoilage of foods. Surface durability is appreciated in the coating and data storage industries in which the surface must remain intact during the service life of the product. As for structural concerns, scratches can trigger stress concentration and ultimately initiate premature fracture and failure. Scratch study is also important in micro- and nano-devices where unintended scratches can easily result in loss of functionality. It is evident that surface scratch is an important concern for polymeric materials [7-29].

Although scratch is one of the common phenomena in the engineering application of polymers, most of the work in this field is largely subjective and qualitative in nature, which makes meaningful correlation difficult. Contradictory conclusions and errors in relative ranking of different polymers often occur. The goal of polymer scratch study is either to find the optimal material for a given application or to predict the possible scratch damage events for a polymer material. It is important to understand how polymers are susceptible to scratch and a fundamental knowledge of the scratch process in polymers is necessary. It is expected that the current research can provide a better understanding of polymer scratch behavior for engineering applications and material development.

1.2 Overview of research plan

Unlike research on traditional materials such as metals and ceramics, ongoing scientific investigation of polymer scratch is a relatively recent phenomenon. This

research field is in its infant stage where rigorous analytical concepts have not yet been established to provide a clear guide to the complex characteristics of scratch. While little research effort on polymer scratch existed before the 1980s, this research area is gaining its importance together with advances in polymer science and technology. Many analytical and experimental works of polymer scratch have been completed over the past two decades, indicating the recent shift of emphasis on polymer scratch study [1-38].

Scratch loading can usually be considered as the superposition of an indentation test on a sliding test. Most indentation studies only considered static linear elastic solutions of the indentation problem [37-38]. Some researchers extended their work to sliding friction [8,9]. However, these analyses are still confined to linear elastic and static conditions. Recent research efforts consider the dynamics of the scratch problem but are limited in analysis to linear elastic study [10-13]. While the above studies are valuable, the fact that the material will undergo large deformation with extensive straining cannot be disregarded in the scratch analysis.

With the recent establishment of the new ASTM/ISO standard for polymer scratch and its wide applications [1,2], it is possible to carry out systematic experimental study and mechanical modeling simultaneously to establish a fundamental understanding of the scratch behavior of polymeric materials [12-29]. Numerical modeling has been adopted by researchers to describe the scratch behavior of polymers [17-19]. Although research efforts on this topic using finite element methods (FEM) remain scarce and are mostly restricted to over-simplified assumptions [35-38], recent three dimensional (3D)

FEM analyses have illustrated the usefulness of numerical simulation to study polymer scratch [17-19,27-29].

To conduct fundamental study of the scratch behavior of polymers, it is necessary to examine its complexity both from material science and mechanics points of view. Due to the nature of the problem, the scratch response of a polymer requires a rigorous treatment from several research concerns, *i.e.*, material behavior, damage mechanism, and mechanics analysis technique.

During the scratch process, polymeric materials usually undergo highly localized large-scale deformation that requires the characterization of material response in the large deformation regime. Depending on the types of polymers and the extent of deformation, polymers respond to deformation differently with time, temperature, stress state (tension or compression; uni-axial or multi-axial), strain rates, etc. Hence, from the material perspective, the scratch analysis should cover material non-linearity, thermo-elasticity, and viscoplasticity [41-42]. The viscoelasticity issues of polymeric material can always be addressed by correct material description if the study of instantaneous scratch response is not adequate. In this work, due to the large 1 mm diameter spherical geometry of the scratch tip and the moderate scratch speed outlined in the ASTM/ISO standards, the heat generation and temperature effect can be neglected.

The next important factor of scratch research is an adequate description of material damage. It is well-known that bulk polymers will undergo damage modes like yield or crazing/cracking, depending on the type and extent of deformation [41-46]. Making the study more challenging is that these two damage modes generally coexist in

scratch-induced damage. The ability to identify these failure mechanisms is crucial when attempting to describe and predict the polymer scratch behavior.

The large scale deformation and complex material characteristics of polymers significantly complicate the analysis of polymer scratch. Consequently, no analytical solutions are available for modeling the polymer scratch behavior. The numerical technique such as FEM has been shown to be an effective research approach since it possesses a mathematical framework that allows the integration of physical phenomena and material response in the simulation [47]. One drawback of numerical simulations is its approximation to the exact solution. Fine discretization must be introduced to obtain close approximation, resulting in the requirement of long computational time and prolonged consumption of computer resources.

Scratch behavior of polymers is determined both by material properties and the stress field induced by scratch. Using both experimental work and numerical analysis, the primary objective of the current research is to gain an insight into the fundamental understanding of polymer scratch behavior. The research efforts will make it possible to establish the correlation between the scratch phenomena and material properties, thus providing the guidelines for development of scratch resistant polymer materials.

1.3 Dissertation layout

As mentioned earlier, both experimental work and numerical simulation are employed in this dissertation to help understand polymer scratch behavior. To further develop the background of scratch research, a compendious literature review of both

topics is given in Chapter II. An integrated research road-map is highlighted to describe the research strategy for the dissertation in this chapter as well. In Chapter III, following the ASTM and ISO test standards, a series of scratch tests are carried out on a broad range of polymers. Various kinds of scratch damage features have been characterized and identified for four different categories of polymers. The effect of testing rate on material properties and thus on scratch damage mechanisms is also studied. Chapter IV gives the assessment of various physical and computational considerations for implementing a FEM analysis of the scratch problem; two effective remeshing algorithms to improve the computational efficiency are introduced and implemented in a commercial finite element software package ABAQUS [47]. Next, in Chapter V, a parametric study is presented to examine the influence of material and surface properties on scratch performance of polymers. In Chapter VI, the scratch behavior of polymeric coatings on soft and hard substrates is studied experimentally and numerically. The mechanistic insights for the observed polymer coating deformation mechanisms and failure modes are provided. In Chapter VII, using the experimental and numerical findings from above chapters, a generalized scratch damage mechanism map for polymers and a phenomenological deduction of the scratch damage mechanism are presented. Correlation between different material types and scratch damage mechanisms is made. It is found that both the material characteristics and the stress state exerted on the scratched surface are responsible for the various scratch damage mechanisms observed. Concluding remarks to summarize scratch research works and an introduction of the future research direction is given in Chapter IX. Finally, citation of referred

literature in the dissertation is documented. As for future work, it is necessary to obtain a more realistic material law to capture the the two essential polymer damage modes: shear yielding and crazing/cracking. The mechanical modeling of stick-slip phenomena should be carried out. An objective automated method of evaluating polymer scratch resistance based on the human visual biology and the nature of polymer scratch should be developed. Possible extension of the present research to address the mar and abrasion behaviors should also be pursued.

CHAPTER II

LITERATURE REVIEW AND RESEARCH STRATEGY

Polymer scratch behavior has gradually become an important research topic over the last two decades. To identify the key research considerations and scopes in the field, it is essential to familiarize with the current state of knowledge, as well. This chapter provides a review of the fundamental concepts in polymer scratch behavior. To apply the existing knowledge to address the scratch research needs, a cohesive research strategy adopted for this dissertation is introduced accordingly.

2.1 Literature review

Essentially, the scratch process involves a hard indenter being placed in contact with a surface and traversing across on a substrate, as shown in Fig. 2.1[5]. The scratch process herein is defined as a mechanical deformation process where a controlled force or displacement is exerted on a hard spherical tip to indent onto a surface and move across its surface at a prescribed speed. Scratch research belongs to the field of tribology, which is defined as the science and technology of interacting surfaces in relative motion. Other than the indentation in which the normal load is uniformly distributed beneath the indenter, the scratch process involves a friction-induced sliding process in which the indenter is supported by only a portion of material beneath the scratch tip.

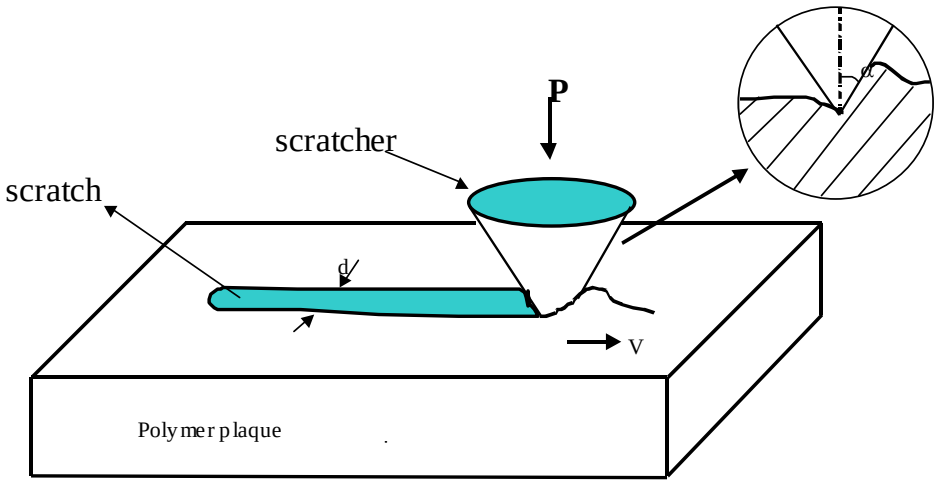

Fig. 2.1. Schematic of scratch process.

The need to understand scratch behavior in polymers prompts the development of suitable scratch test methods. A wide variety of test methods have been utilized for polymer scratch such as: Ford five-finger test, Taber scratch test, Pencil hardness, Rover test, Chrysler crocking, PSA test, Instrumented indentation test, DIN Abrasion [12-13]. Meanwhile, the nano-indenter and the nano-scratcher have been used to study nano-scale scratch behavior. Extensive research efforts have been dedicated to the development of an objective test methodology for polymer scratch and to assess the corresponding complex material behaviors [12-19]. This has led to the establishment of an ASTM and ISO standard for scratch testing of polymers [1, 2]. This progressive scratch load test appears to be a promising quantitative method for systemically evaluating the polymer scratch behavior.

A photograph of the ASTM scratch tester (Surface Machine Systems, LLC) is shown in Fig. 2.2. It is utilized to perform the scratch tests at ambient conditions. The

machine is capable of recording tangential and normal forces as well as scratch distance and instantaneous depth experienced by the scratch stylus, which can be easily replaced for various geometrical shapes and sizes as needed.

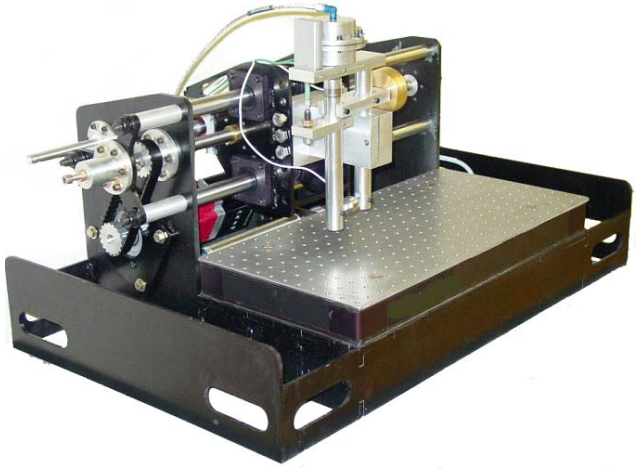

Fig. 2.2. A custom-built scratch machine (ASTM/ISO standard based).

A literature review of scratch research efforts reveals that, intuitively, the early stage of research often heavily relies on accumulated knowledge from indentation studies and scratch research methodologies were proposed accordingly. The closed-form linear elastic solutions were developed for the static indentation problem which marks the emergence of the area now commonly known “contact mechanics” [7]. The scope of the indentation problem has been extended to consider the effect of tangential force due to sliding friction between isotropic bodies [4, 7, 32]. However, these analyses are essentially linear elastic and hence cannot describe the large scratch deformation experienced by the material, especially for polymeric materials. Moreover, those static analyses results at most can be applied to the instant when sliding of the scratch tip is about to occur. Research efforts on dynamic aspects of the scratch problem are mostly

limited to a linear elastic study of isotropic materials [8-10]. For viscoelastic materials, the Hertzian indentation problem for a rigid spherical punch was considered [12, 35].

Unlike ceramics and metals, polymers are particularly susceptible to surface deformation and damage, even under low contact loads. During a scratch process, plastic flow may occur under extensive straining and such plastic deformation must be considered in the analysis. In addition, a polymer can consecutively or simultaneously undergo various modes of material damages like plastic yielding, crazing, and microcracking. Due to the inherent material nonlinearity, there has been no analytical work for polymeric material under indentation or sliding. The nonlinear material characteristics and complex scratch-induced stress fields have made it extremely difficult for polymer scratch study. While the above works provide valuable knowledge within their own merits, their limitation in the material description and analysis scope requires a more comprehensive study of polymer scratch behavior. It should also be noted that the scratch tip geometry, tip material, surface characteristics, and rate of testing can all significantly affect the scratch performance of polymers.

Generally speaking, polymer damage includes two main types, ductile damage (e.g., shear yielding and ironing) and brittle damage (e.g., crazing and cracking), depending on the material characteristics and the stress state and magnitude induced [41-46,48-49]. As has been demonstrated in the past [17-19], scratch-induced deformation of polymers is a complex mechanical process. Since the scratch process involves generation of complex stress states at different locations near the scratch tip, the occurrence of scratch-induced damage mechanisms cannot easily be predicted.

Numerical analysis can be utilized to investigate the damage features incurred during polymer scratch.

For numerical techniques, while the molecular dynamics (MD) simulations have been tested for understanding of nano-scale scratch phenomena [50-53], the computational approach commonly adopted on the micro- or macro- level of polymer scratch is the finite element method (FEM). FEM has been shown to be an efficient tool for gaining insight into the complex mechanical behavior and damage mechanisms [31, 42, 54-61]. It has been shown to be effective for modeling polymer scratch deformation even when there is significant material and geometric non-linearity [11, 17-19]. Previous research efforts on this topic using FEM remain scant and most works are restricted to indentation, linear plastic material, or the two-dimensional plane-strain problem [11, 42, 53]. Only until recently, with the emergence of powerful computation sources, three-dimensional (3D) FEM analysis becomes possible for polymer scratch research [17-19, 27-29, 62-67].

2.2 Research strategy

From the accumulated knowledge of earlier research efforts and the discussion of various requirements of polymer scratch research from Chapter I, there are several attributes that the analysis of the scratch problem should possess for a comprehensive study. For this scratch study, the research emphasizes:

- Examining phenomenological scratch damage processes and mechanisms.
- Implementing efficient FEM numerical modeling for polymer scratch.

- Understanding how testing conditions affect scratch behavior.
- Assessing the effect of material and surface properties on the scratch response.

The various scratch-induced damage features, e.g., mar, fish-scale, parabolic crack, and material removal (these terms will be defined later), will occur according to the material characteristics and resulting stress state and magnitude imposed. Correlation between the material properties and mechanics during scratch must be established to allow for prediction of scratch-induced damage mechanisms and their evolution process. The research strategy used in this work is illustrated in Fig. 2.3.

To aid the design of scratch-resistant polymers, knowledge regarding the scratch behavior of a wide variety of polymers and its evolution process is essential and has been obtained as the first priority. Scratch damage characterization is also needed. Presented in Chapter III, extensive scratch tests have been performed on a wide range of polymer materials which are classified as four general types of polymers: (I) ductile and strong, (II) ductile and weak, (III) brittle and weak, and (IV) brittle and strong. To investigate how the damage process is affected by scratch testing rate, the scratch tests were also conducted at different rates on ethylene-propylene rubber (EPR) rich soft thermoplastic olefins (TPO). The resultant scratch damage mechanisms were carefully investigated. The observed damage features were identified and classified according to material type.

As the literature review shows, a numerical approach is more suitable to perform the scratch analysis than an analytical approach. FEM is selected for the current study due to its versatility to accommodate various physical phenomena like surface contact,

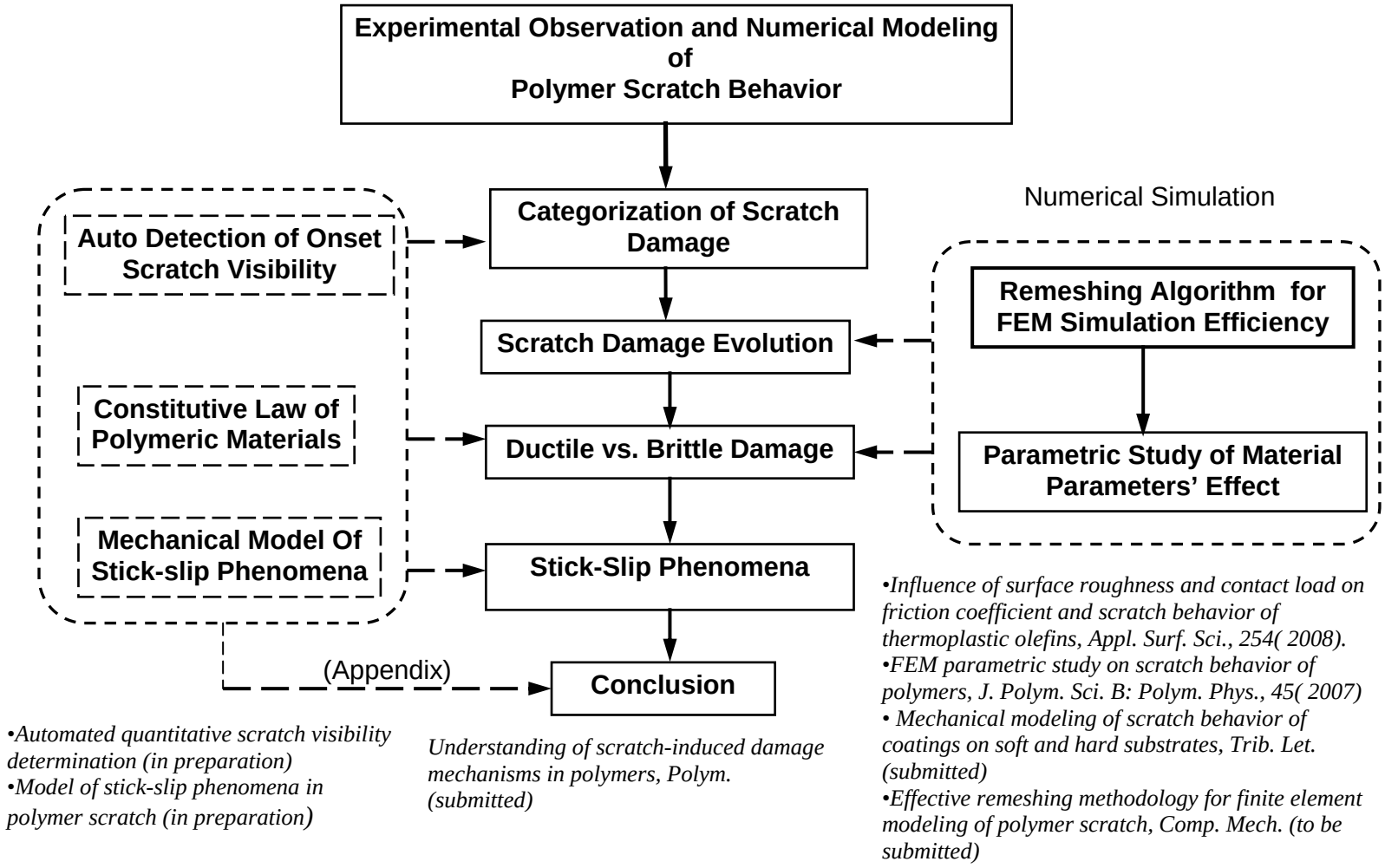

Fig. 2.3. Flow chart of research strategy.

frictional interaction, and atypical material responses. There is an additional challenge for numerical modeling of polymer scratch to explore the mechanistic reasons responsible for the observed damage mechanisms. The high computational cost caused by the vast number of small elements which are necessary to capture the nonlinear and heavily localized geometrical distortion is slowing efforts toward in-depth study of polymer scratch behavior. Chapter IV presents two new modeling algorithms in an effort to improve computational efficiency. A comparative study is performed and shows that using the proposed algorithms, better computation efficiency can be achieved without comprising simulation accuracy.

It is of great interest to learn how to increase scratch resistance of polymers. With the help of the proposed FEM algorithms, parametric studies could be performed to learn how material properties such as Poisson's ratio, Young's modulus, and yield strength affect scratch behavior. These useful suggestions are then obtained and presented in Chapter V. Meanwhile, frictional interaction between contacting surfaces is another important integrated phenomenon in the scratch process. Surface properties such as roughness and friction coefficient have also been studied. Approach to design scratch-resistant polymers is discussed accordingly.

Using the ASTM scratch test method and numerical modeling, the scratch behavior of polymeric coatings on soft and hard substrates has been studied and presented in Chapter VI. The analysis provides mechanistic insights for the observed polymer coating deformation mechanisms and failure modes.

Using the highlighted material science and mechanics tools, it has been found that both the material characteristics and the complex stress state exerted on the scratched surface are responsible for the various scratch damage mechanisms observed. The “stick-slip” phenomenon has been adopted to explain the periodic feature of scratch damage. A better understanding of the correlation between the scratch damage process and material properties is obtained. A generalized scratch damage mechanism map for polymers is presented in Chapter VII and can be used to predict the material properties needed to prevent the formation of undesirable scratch damage mechanisms.

Selection of an appropriate material constitutive model is a key factor in the analysis of any deformation process. The constitutive law adopted in this work uses the experimental stress-strain curves which take into account strain-softening and strain-hardening of the material. It may still be insufficient to respond to a complex mode of deformation like a scratch. To address this issue, additional research effort has been placed in the appendix to look into the constitutive modeling of polymers. The knowledge gained from this effort lays the foundation for future development of polymer surface study as well as constitutive modeling of amorphous polymers.

The analytical mechanical model of scratch stick-slip phenomena and an automatic method to objectively evaluate the scratch visibility are also provided in the appendix.

The current study is part of a larger effort to gain an insight into the fundamentals of scratch behavior in polymers. The scratch behavior of a wide variety of polymers is investigated to allow determination of the most important material parameters that affect

scratch resistance. It is hoped that this research will be a useful contribution to understand scratch behaviors in polymers and could provide useful guidelines for other researchers to design polymeric material with good scratch resistance.

CHAPTER III

CHARACTERIZATION OF POLYMER SCRATCH DAMAGE

A fundamental understanding of the occurrence of scratch damage and their evolution process is needed for successful design of scratch resistant polymers. The goal of this chapter is to identify the typical polymer scratch damage features and understand their evolution process. Following the ASTM and ISO test standards, a series of scratch tests were carried out on four categories of polymers: I) ductile and strong, II) ductile and weak, III) brittle and weak, and IV) brittle and strong.

3.1 Experimental observation

3.1.1 Materials

To study the scratch behavior of polymers, five typical commercially available polymers were chosen for the present study and are categorized as: (I) ductile and strong (polycarbonate (PC); Lexan 9034, GE Plastics); (II) ductile and weak (TPO with 70% polypropylene and 30% ethylene–propylene rubber (EPR), Advanced Composites); (III) brittle and weak (polystyrene (PS), Styron 685D, Dow Chemical); (IV) brittle and strong (epoxy, DER 332, Dow Chemical). The typical stress-strain curves of the four categories of polymers are illustrated in Fig. 3.1.

All samples possess smooth surface with dimensions of 100 mm x 150 mm x 3 mm. The sample surfaces were cleaned by an air duster prior to the scratch tests.

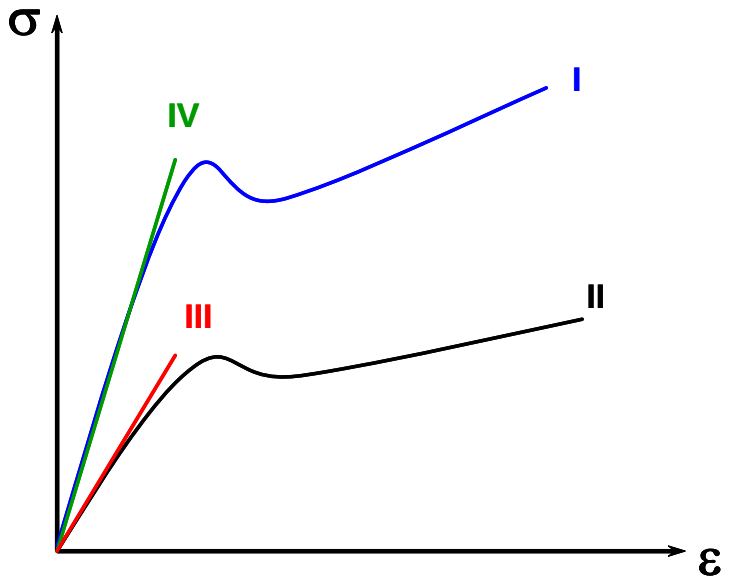

Fig. 3.1. Four categories of polymers: I) ductile & strong; II) ductile & weak; III) brittle & weak; and IV) brittle & strong.

3.1.2 Scratch tests

Following the ASTM and ISO testing standard for polymer scratch [1,2], a custom-built scratch machine (Surface Machine Systems, LLC) was utilized to perform the scratch tests at ambient condition (Figure 2.2). The machine is capable of recording tangential and normal forces as well as scratch distance and instantaneous depth experienced by the stylus.

A stainless steel spherical tip with 1 mm in diameter was used for the weak polymers and soft TPO while a tungsten carbide spherical tip with 1 mm in diameter was adopted for the strong polymers. The scratch length was set at 100 mm. A linearly increasing normal load was imposed on the scratch tip at a scratch velocity of 100 mm/s for all rigid polymers.

3.1.3 Scratch damage investigation

For the purpose of promptly assessing the various surface scratch damage features, the images of scratched samples were acquired using the Epson 4870 Perfection Photo flatbed PC scanner at 3200 dpi resolution. The study of scratch surface features in polymers using scanning electron microscopy (SEM) has been widely reported [13-16,20-25]. In this study, SEM (JEOL JSM-6400) was adopted to investigate the detailed scratch damage mechanisms. All samples were coated with Au-Pd and studied using SEM, operated at an accelerating voltage of 15 kV.

For optical microscopy (OM, Olympus BX60) investigation of the subsurface damage in scratched samples, thin sections were cut from the longitudinal scratch directions. Using diamond saw with cooling water, samples were carefully cut about 3 mm away from the scratch path ensuring no additional damage during cutting. Then each sample was attached to a glass slide with an epoxy adhesive and polished to a thickness of approximately 100 μm with low applied pressure and flowing cooling water. The samples were viewed using OM under both bright field and cross-polarized lights.

3.2 Damage mode categorization

The polymer scratch damage mechanisms are quite different for the four polymer types at different load levels. To assist fundamental understanding of polymer scratch behavior, phenomenological categorization of the scratch damage modes is necessary.

3.2.1 Initial damage zone

For all materials tested, there is only a small amount of deformation observed under a low load and stress level. This includes fully recoverable elastic deformation, time-dependent viscoelastic deformation, and a small amount of non-recoverable plastic deformation resulting from compressive indentation, tentatively termed “mar”. It is noticed that for polymers such as epoxy and PC, the initial damage induced by scratch is practically undetectable until a relatively high normal load is applied because of their high strength and elastic recovery against deformation. On the other hand, polymers such as PS and TPO may exhibit various forms of scratch-induced localized small scale damage in this zone, including ironing and surface roughening, etc.

3.2.2 Fish-scale zone

With an increasing scratch normal load, the TPO substrate begins to undergo plastic deformation, forming a periodic concave damage feature pointing toward the scratch direction. Fig. 3.2(a) illustrates this scratch damage mechanism at the transition from the initial damage zone to the fish-scale damage of TPO. If the normal load is further increased, the fish-scale damage can become a well-developed, repeatable pattern as presented in Fig. 3.2(b). The fish-scale damage is dominated mostly by the plastic drawing of substrate material under the tip and is one of the most widely observed phenomena for polypropylene-based polymers [20-25, 33-35].

For PS, a barely detectable pseudo fish-scale pattern is found to coexist with micro-scale cracks or voids. This damage feature is shown in Fig. 3.2(c).

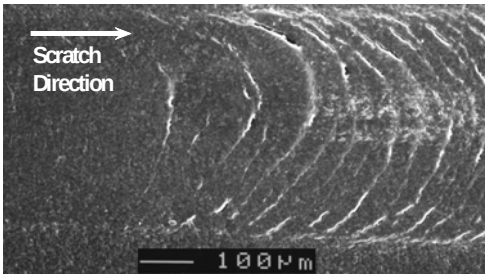

a)

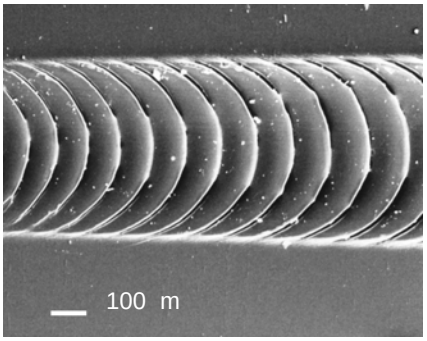

b)

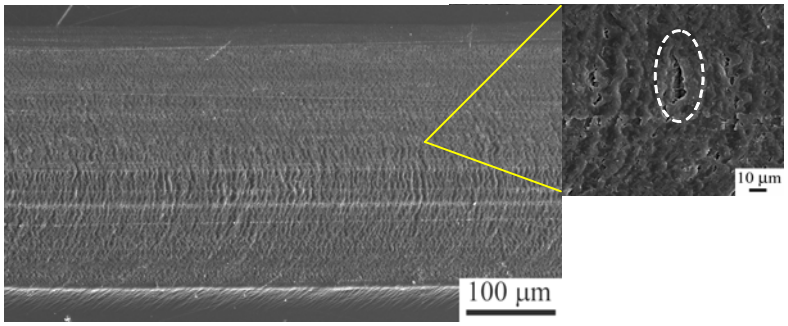

c)

Fig. 3.2. Fish-scale damage using SEM: a) onset of fish-scale formation for TPO; b) well-developed fish-scale for TPO; and c) pseudo fish-scale pattern mixed with crazes/voids for PS.

3.2.3 Parabolic crack zone

For PC and epoxy, except for the initial localized damage, there is no other observable scratch-induced damage to form until a high normal load of 70 and 75 N for

PC and epoxy, respectively. At this point, parabolic cracks form and become the dominant damage mode. This kind of periodic convex damage feature pointing opposite the scratch direction can be easily identified as a typical brittle damage feature. Fig. 3.3(a) illustrates the transitions from mar deformation to the parabolic crack zone for epoxy. One can clearly find that the parabolic crack becomes more regular and dense with an increasing scratch load. The transition from mar damage to the parabolic crack zone for PC is shown in Fig. 3.3(b). Similar parabolic cracks are also observed in ceramics, glass, and even metal [32, 48-51].

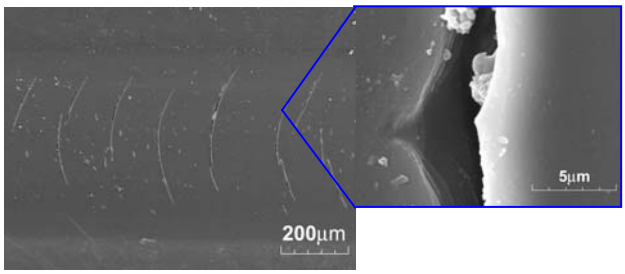

a)

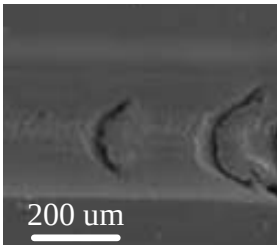

b)

Fig. 3.3. SEM of parabolic crack pattern in: a) epoxy; and b) PC.

3.2.4 Material removal zone

Ultimately, material removal will occur when the scratch load continues to increase. In the material removal zone, the tip penetrates through the top surface of the

substrate and the significant material is removed from the surface. Fig. 3.4(a) shows the transition from the well-developed fish-scale zone to the rupture of this repeated fish-scale pattern, leading to material removal of TPO. Fig. 3.4(b) shows the transition from the pseudo fish-scale pattern mixed with crazes/voids to the material removal of PS. For PC, the transition from the parabolic crack zone to the material removal zone is shown in Fig. 3.4(c). Although this type of damage was not observed in epoxy in the current test condition, it is expected that material removal will occur if the applied load is high enough.

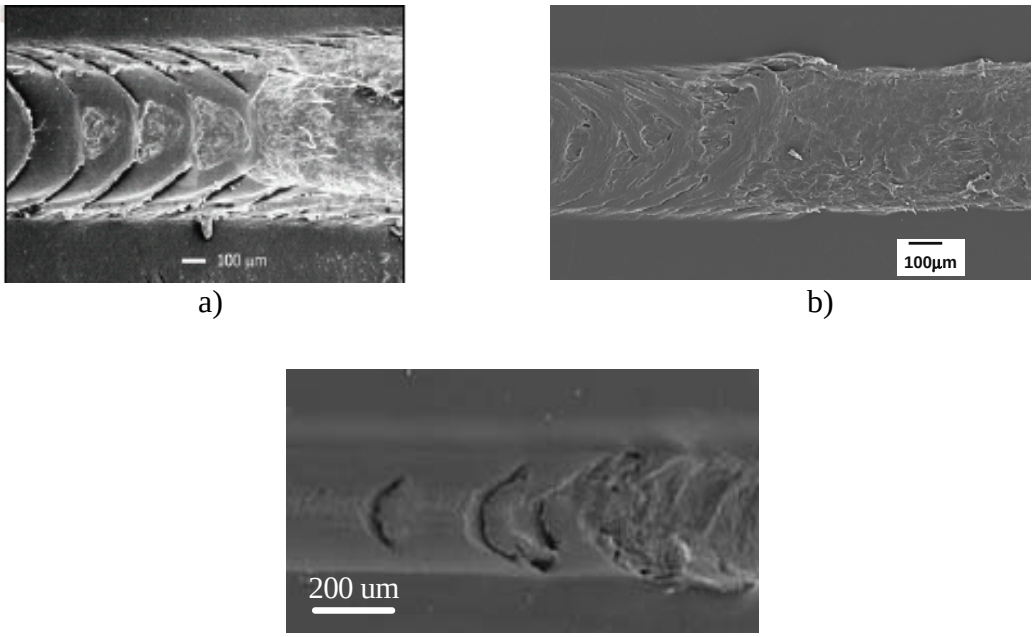

a) b)

c)

Fig. 3.4. SEM of the material removal region in: a) TPO; b) PS; and c) PC.

3.3 Evolution of scratch damage modes

For the four categories of polymers, the evolution process of their damage with increasing normal load is quite different and is illustrated in Fig. 3.5. The detailed characteristics of these polymers are described below.

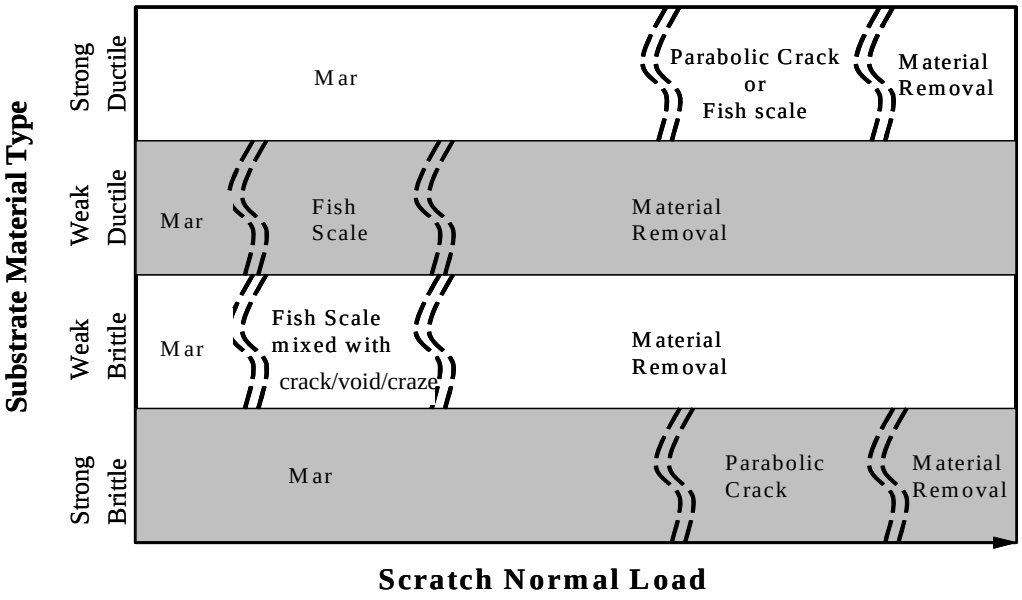

Fig. 3.5. Evolution map of polymer scratch damage.

3.3.1 Ductile and strong material

For ductile and strong polymers, which exhibit high tensile strength and high ductility, only minor mar damage has a chance to occur under a low scratch load. Since the modulus and yield strength of this category of polymer are generally high, the scratch penetration depth is low. As a result, the material resistance against the tip movement from the material pile-up in front of tip remains low, i.e., the scratch coefficient of friction (μ_s) stays low. From previous works [20, 26-27], the smaller μ_s is,

the better the scratch resistance is obtained. Not until an extremely high load is applied will the tip penetration become high enough to cause a dramatic increase in μ_s.

As observed, the occurrence of brittle damage, i.e., parabolic cracks, is the most prevalent damage mode under a high normal load for PC. For other strong polymers that are more ductile and exhibit milder strain hardening characteristics (see also FEM modeling analysis in following chapters), it is anticipated that the ductile-type fish-scale damage will prevail.

3.3.2 Ductile and weak material

For ductile and weak polymers, which exhibit low tensile strength but high ductility, mar damage will occur first under a low scratch load. Then, the ductile fish-scale damage becomes the most favorable damage mode and will become well developed with increasing scratching load. With further increase in scratching load level, material removal takes over to rupture the well-developed fish-scale pattern. Finally, significant material removal takes place from its surface.

3.3.3 Brittle and weak material

For brittle and weak polymers, which exhibit low tensile strength and low ductility, small-scale damage will occur even at low loads. As the scratching load level increases, scratch-induced damage will occur in the forms of a mixture of pseudo fish-scale and microcracks, crazes or voids. At a high level of scratch load, material removal takes place in an irregular manner.

3.3.4 Brittle and strong material

Similarly, mar damage occurs at a low load for this type of material. In spite of its brittleness, a high scratching load level is required to develop any detectable damage. Parabolic cracks will eventually form after the scratching load reaches a certain magnitude. Epoxy which exhibits low tensile ductility but high compressive strength and ductility is a good example of this type of material. As expected, ceramics and glass fall into this category of material type and similar scratch behaviors have been observed [48-51].

3.4 Test rate effect

To study how the rate of testing influences the scratch-induced damage mechanisms, a TPO with a high concentration of EPR (30 % PP +70% EPR, Sumitomo Chemical, Ltd.), also termed soft TPO, was investigated. For the soft TPO, scratch tests were performed at scratch velocities of 1 and 100 mm/s, respectively. The load range was from 1 N to 30 N and 1 N to 100 N for the weak and strong polymers, respectively; while a lower load range of 0.5–7 N was employed for the soft TPO to prevent penetration of the scratch tip through the substrate.

Soft TPO has been shown to exhibit high rate-sensitivity. Its apparent tensile strength increases from 0.75MPa to 1.78MPa and the elongation at break drops from 170% to 120% when the rate of tensile test increases from 0.083mm/s to 8.3mm/s [24]. The faster the rate of testing is, the more the scratch behavior will resemble a rigid brittle material.

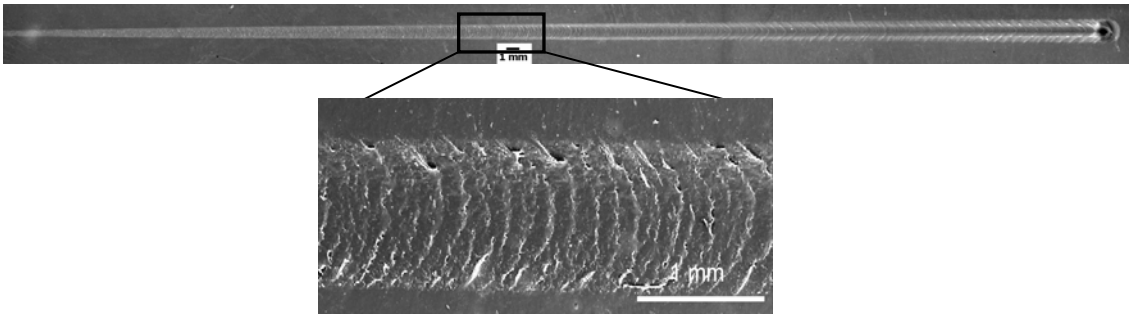

a)

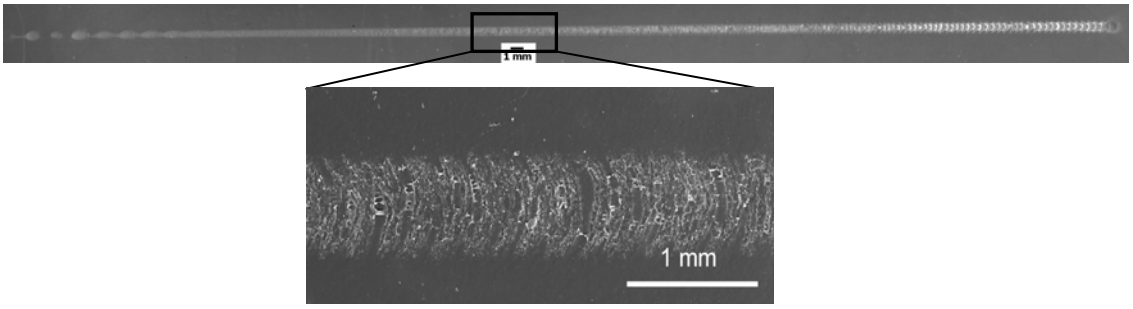

b)

Fig. 3.6. Scratch damage of soft TPO at different test rates of: a) 1mm/s; and b) 100mm/s.

The scratch-induced damage features of the soft TPO at different scratch rates are shown in Fig. 3.6. The soft TPO can be considered as ductile and weak material at 1 mm/s of testing rate. The fish-scale type of damage clearly exists and is well-developed (Fig. 3.6(a)). At 100 mm/s of scratch testing rate (Fig. 3.6(b)), only pseudo fish-scales mixed with micro-crazes or cracks are found, which is similar to what is observed in PS (Fig. 3.2(c)). The soft TPO can be categorized as brittle and weak at a high testing rate.

It is worth noting that both the testing rate and temperature can have significant influences on the scratch behavior of polymers. The testing rate dramatically affects

polymer scratch behavior through its effect on material mechanical responses. Similarly, the temperature effect should be considered, as well. A strong material could behave as a weak material at a higher temperature and its scratch damage mode could change accordingly.

CHAPTER IV

REMESHING ALGORITHM OF FINITE ELEMENT MODELING

Due to the large-scale localized deformation characteristics and complex material responses, fine meshes are necessary for finite element simulation of polymer scratch behavior. Consequently, analysis requires extremely long CPU time to accomplish the simulation, which is both costly and impractical. This chapter aims to overcome this obstacle by reducing the CPU time and increasing computational efficiency.

4.1 Introduction

Numerical simulation has been shown to be an efficient tool for gaining insight into the complex mechanical behavior and damage mechanisms experienced during the standardized scratch test [17-19]. To understand nano-scale scratch phenomena, molecular dynamics (MD) simulations have also been employed [50-53]. On the micro- or macro-scale level of polymer scratch, the finite element method (FEM) has been shown to be effective for modeling polymer scratch deformation even when there is significant material and geometric non-linearity [27-29].

However, FEM simulation still faces significant challenges for successful modeling of realistic polymer scratch behavior. In addition to the classical mechanics complexities, such as obtaining a realistic material constitutive model for polymers and choosing appropriate criteria for various damage mechanisms, additional challenges exist. A vast

number of small elements are necessary to capture the nonlinear and heavily localized geometrical distortion for three-dimensional (3D) FEM modeling of polymer scratch.

The numerical simulation of polymer scratch can be divided into three steps that correspond to the experimental process. The first step is the initial indention where the rigid indenter approaches the substrate with a small normal load of 1N to establish sufficient surface contact between scratch tip and substrate. The second step is the actual scratch where the indenter moves forward at a constant velocity and scratches the substrate with a linearly increasing normal load from 1N to 30N. Finally, the indenter stops and retracts from the substrate.

Fig. 4.1 shows a 50 mm x5 mm x3 mm computational half domain substrate and 1 mm diameter spherical scratch tip used as a model to estimate the computational time via the commercial FEM software ABAQUS [31]. For global fine mesh method, the whole simulation process along the scratch path, i.e., the path along which large-scale deformation occurs, a fine mesh is globally adopted (grey area in Fig. 4.2(a)). The typical size of an eight-node 3D linear brick element along the scratch path is 0.05 mm x0.05 mm x0.05 mm whose size is chosen to give converging simulation results and assure numerical accuracy. The adaptive remeshing module of ABAQUS/EXPLICIT was employed to overcome excessive element geometry distortion. The polymer was described by a piecewise linear elastic-plastic stress-strain curve similar to the one shown in [64]. Using an SGI Altix 3700 Distributed Shared Memory (DSM) architecture supercomputer [55], a typical 3D numerical stress analysis for modeling scratch requires about 139 CPU hours.

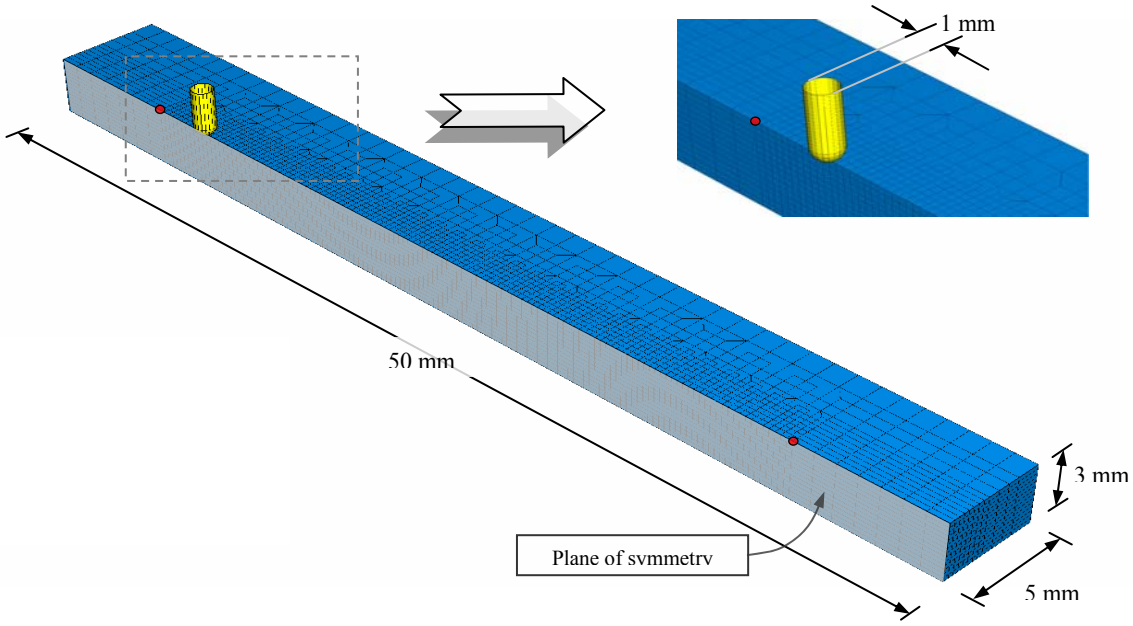

Fig. 4.1. FE model of polymer scratch using the global fine mesh method.

High computational cost caused by the needs for large amount of elements for accurate simulation is slowing efforts toward in-depth numerical modeling of polymer scratch behavior. In an effort to improve the modeling efficiency, this chapter presents two new modeling algorithms: the extended fine mesh (EFM) and the moving fine mesh (MFM) methods. Effectiveness of these approaches is assessed.

4.2 Extended fine mesh method

While fine meshes are crucial for the stability of the elements due to highly localized deformation of the material on the scratch path, they are only necessary in the region where large-scale localized deformation occurs. A coarse mesh can be employed throughout the rest of the model to save computational time [56-59].

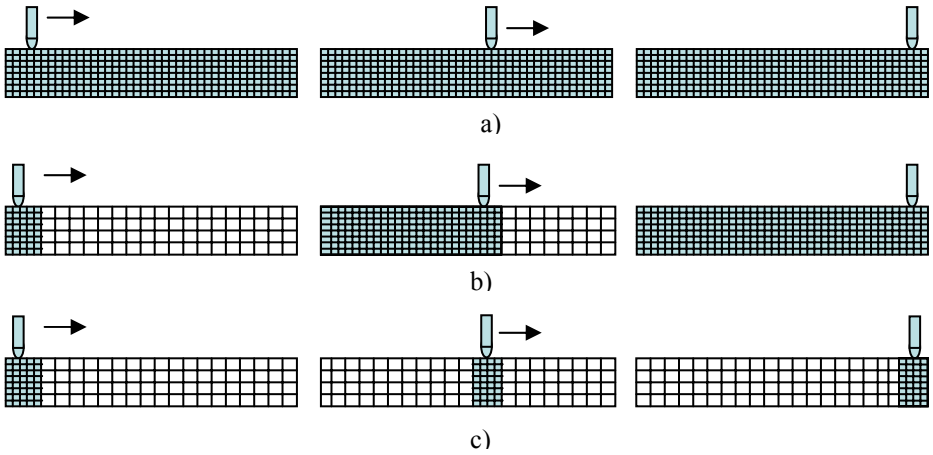

Fig. 4.2. Diagrams of the computation algorithms employed in this study: a) global fine mesh; b) extended fine mesh; and c) moving fine mesh.

4.2.1 EFM algorithm

For the scratch process, coarse meshes can be applied for regions where the material only undergoes small deformation (Fig. 4.2(b)). A fine mesh is used in the vicinity of the scratch tip and extended along with the moving tip. The EFM algorithm will follow this algorithm accordingly. As illustrated in Fig. 4.3, at the beginning step of simulation, a fine mesh is used for the beginning section of the scratch path. A coarse mesh is utilized for the region far from the scratch tip, thus little effect on the simulation accuracy. Less computation time is consumed due to the smaller elements number.

When the scratch tip moves forward and creates severe deformation, the fine mesh region is extended forward for the next calculation step. The tip moving distance is chosen as a guide to determine when a refinement is needed for the next step. If a total of N steps are applied, at the i^{th} step, the fine mesh domain covers i/N of the total scratch path. After the tip travels a scratch distance of i/N length, the fine mesh region is

extended to (i+1)/N of the total scratch path. A fine mesh process zone of 2mm, which is twice the tip diameter, is typically sufficient to cover the highly deformed region.

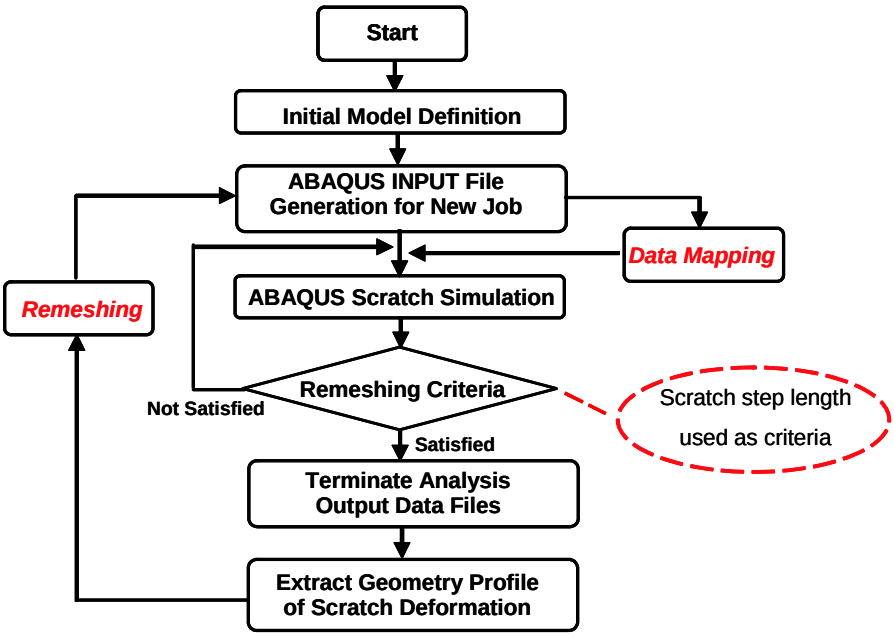

Fig. 4.3. Computation algorithm of the EFM method.

This fine mesh extension process is repeated until the designated scratch distance or load is reached. The total number of elements will be the same as the global fine mesh method only during the last calculation step.

4.2.2 Refinement and data-mapping

In the actual computation process, the element refinement and the data-mapping which transfers the necessary mechanical field information from the initially coarse elements to the new refined elements have to be conducted before the next calculation step begins.

The refinement procedure requires subdivision of the coarse mesh elements. The geometrical configuration of the refined elements needs to preserve the element shape

quality. The coarse eight-node 3D linear brick element can be uniformly refined to form fine elements in a fashion shown in Fig. 4.4. In this study, a coarse element with original size of 0.4 mm x0.4 mm x0.4 mm was subdivided into 8x8x8 fine mesh elements with a resultant size of 0.05x0.05x0.05 mm.

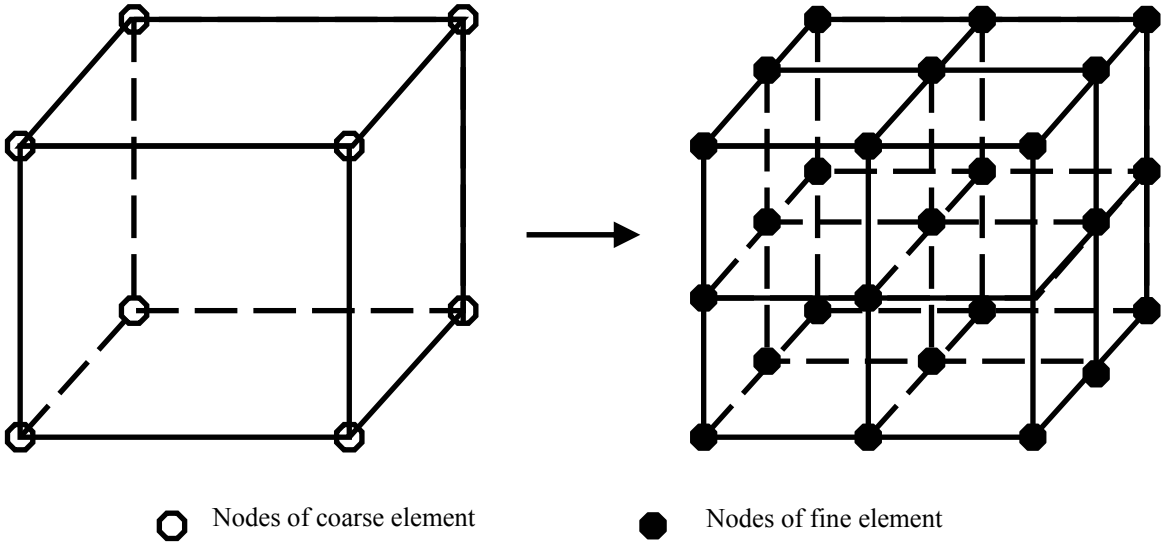

Fig. 4.4. Refinement of the 8-node block element.

The data-mapping, which transfers the field information from the coarse element to the new refined element, can be divided into two procedures. Fig. 4.5 shows similar procedures in the four-node 2D linear element case as an illustration in which not all transfer between integration points and nodes are plotted.

First, the field data values such as stresses and strains at nodal points in the old/coarse mesh are obtained by extrapolation from the values at integration points, where the accuracy is greatest, Fig. 4.5(a). After the extrapolation has been performed on an elemental basis, smoothing is achieved by calculating the mean value over all

elements attached to each node. ABAQUS automatically performs this step, so no coding is necessary.

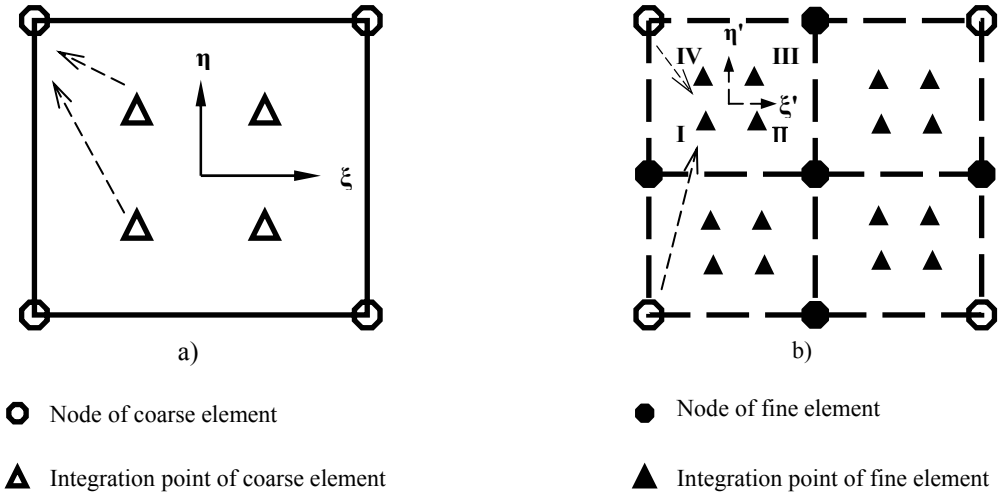

Fig. 4.5. Field data mapping: a) extrapolation from the integration points to the element nodes in an old mesh; and b) interpolation from the element nodes in an old mesh to the integration point in the refined mesh.

To obtain the field data values (σ) at integration point j in the refined mesh, after the subdivision of the coarse meshes, interpolation from the values at nodal points i in the old/coarse mesh is performed using

$$\sigma_j = \sum_{i=1,8} \varphi_i(\xi_j, \eta_j, \zeta_j)\sigma_i \tag{4.1}$$

here σ_i stands for the values at nodal points in the old/coarse mesh, ξ_j, η_j and ζ_j are local coordinates in the coarse element of integration point j in the new element ($-1 \leqslant \xi, \eta, \zeta \leqslant 1$). The interpolation functions φ_i have the same tri-linear form for the used eight-node 3D linear brick element [65]:

$$\varphi_1 = (1-\xi)\,(1-\eta)\,(1-\zeta)/8$$

$$\varphi_2 = (1+\xi)\,(1-\eta)\,(1-\zeta)/8$$

$$\varphi_3 = (1+\xi)\,(1+\eta)\,(1-\zeta)/8$$

$$\varphi_4 = (1-\xi)\,(1+\eta)\,(1-\zeta)/8$$

$$\varphi_5 = (1-\xi)\,(1-\eta)\,(1+\zeta)/8$$

$$\varphi_6 = (1+\xi)\,(1-\eta)\,(1+\zeta)/8$$

$$\varphi_7 = (1+\xi)\,(1+\eta)\,(1+\zeta)/8$$

$$\varphi_8 = (1-\xi)\,(1+\eta)\,(1+\zeta)/8 \qquad (4.2)$$

The local coordinates of integration points of the eight-node 3D linear brick element have the same form for both the coarse mesh and the fine mesh [65]:

$$(\xi,\eta,\zeta) = (\pm\frac{1}{\sqrt{3}},\pm\frac{1}{\sqrt{3}},\pm\frac{1}{\sqrt{3}}) \qquad (4.3)$$

With the known local coordinates of integration points (ξ', η' and ζ') in the new mesh, their local coordinates (ξ, η and ζ) in the old mesh can be calculated correspondingly. For instance, in the 2D case shown in Figure 4.5(b), the local coordinates of the integration point I in the fine element are ($\xi'_I = -1/\sqrt{3}$, $\eta'_I = -1/\sqrt{3}$) and its local coordinates in the coarse element are ($\xi_I = -½\,(1+1/\sqrt{3})$, $\eta_I = ½(1-1/\sqrt{3})$).

Then, by using equation (4.1), the field values at each integration point of all 512 fine elements are obtained by interpolation in matrix form:

$$\{\sigma\}_{\text{integration points in fine elements}} = [A]\,\{\sigma\}_{\text{8 nodes in old element}} \qquad (4.4)$$

here, [A] is a 4096x8 known matrix since the shape functions and the location of those 4096 integration points are known.

For this study, after extracting the field data from the output file from the previous step using a user-coded Python subroutine, a FORTRAN subroutine is programmed to conduct the geometry reconfiguration and data-mapping using the above algorithm. Then, another Python subroutine creates the input files of refined mesh for the next ABAQUS calculation step.

4.2.3 Estimation of computation efficiency

The improvement of computational efficiency for the EFM approach can be estimated. The execution time of the finite element method is primarily the equation-solution time of the linear system $A_{nxn}X=b$ in which n is the rank of the global stiffness matrix A. The cost for a general system of linear equations depends on the rank of the coefficient matrix and is approximately $O(n^3)$. For the FE method, a symmetrical, banded stiffness matrix exists whose bandwidth q is much smaller than n. For this type of linear system, its solution cost is significantly reduced to $O(q^2)$ [65-68]. Here the order in which the nodes or the elements are numbered greatly affects the bandwidth of stiffness matrix and, thus, the computation time. Although the internal numbering algorithm used to optimize the matrix bandwidth is not clear for the FEM program ABAQUS, it is not unreasonable to assume that the optimized bandwidth is somewhat proportional to the rank of the global stiff matrix ($q \propto n$).

The ratio of computational cost (C) for solving two linear systems (i, j) with symmetric banded coefficient matrix can be written as:

$$\frac{C_i}{C_j} = \frac{O(q_i{}^p)}{O(q_j{}^p)} = \frac{O(n_i{}^p)}{O(n_j{}^{p2})} = (\frac{n_i}{n_j})^p \ , \quad \text{p=2} \tag{4.5}$$

It is clear that the smaller n_i/n_j and the larger the p, the larger the reduction in cost by using option "i" versus option "j".

In this study, the improvement of calculation efficiency is from the reduction of the total degrees of freedom of the system. For the global fine mesh method with the total degrees of freedom n_g, T_0 is the total CPU cost of whole scratch process, T_0 /N is the CPU time of each step if the scratch procedure is divided into N steps. For the EFM approach with N steps, the total degrees of freedom at the k^{th} step can be taken as n_g *k/N since the rest of the computational domain is coarse-meshed. Using equation (4.5), the CPU time of the k^{th} step, T_k is:

$$T_k = (\frac{k}{N})^P \cdot \frac{T_0}{N} \tag{4.6}$$

The expected CPU time of EFM approach (T_{EFM}) which is the summation of the computational time over all N steps, is given by

$$T_{EFM} = \frac{T_0}{N} \sum_{k=1}^{N} (\frac{k}{N})^P \tag{4.7}$$

For an infinite amount of calculation steps,

$$T_{EFM} = \lim_{N \to \infty} \frac{1+N}{2N} T_0 = \frac{1}{2} T_0 \tag{4.8}$$

if p is taken as one for a conservative estimation. Equation (4.8) shows that the computational efficiency can be doubled using the EFM method.

The above estimation does not include the CPU time from the data-mapping which is a data and I/O intensive procedure. The additional CPU time used between

calculation steps could negate or even obliterate the benefit of this approach if too many calculation steps are involved.

4.3 Moving fine mesh method

In the EFM method, the fine mesh zone extends as the tip moves forward. After the scratch tip passes, the fine meshes are retained although no further large-scale deformation is expected. The remaining fine mesh regions behind the scratch tip become a computational burden. It is apparent that the computational efficiency can be further improved if the already scratched fine mesh regions can be replaced with the coarse mesh during the calculation steps.

4.3.1 MFM algorithm

Similar to the EFM method, the MFM adopts fine elements for the beginning section of the scratch path while a coarse mesh is utilized for the rest of the body. A buffer zone is also added in front of the moving fine mesh region, as discussed in the EFM method.

When the fine mesh zone is extended to the region in front of the scratch tip, the scratched fine mesh region behind the scratch tip is re-coarsened after the tip has passed. In other words, the fine mesh zone is moving along with the moving scratch tip (Fig. 4.2(c)).

Here the re-coarsening procedure is the reciprocal operation of the refinement discussed above. The process of the scratch tip moving forward along with the fine mesh

extension and the re-coarsening is repeated until the designated scratch distance is reached.

To determine the region needed to be re-coarsened, a vector component of strain gradient along the scratch direction is introduced in this simulation as a physical criterion. When the strain gradient falls below a preset physical criterion of 1% per mm, the scratched fine mesh region will be re-coarsened.

The idea of a moving fine mesh zone can be further improved by removing the scratched fine mesh zone rather than re-coarsening it. This improved MFM algorithm is illustrated in Fig. 4.6

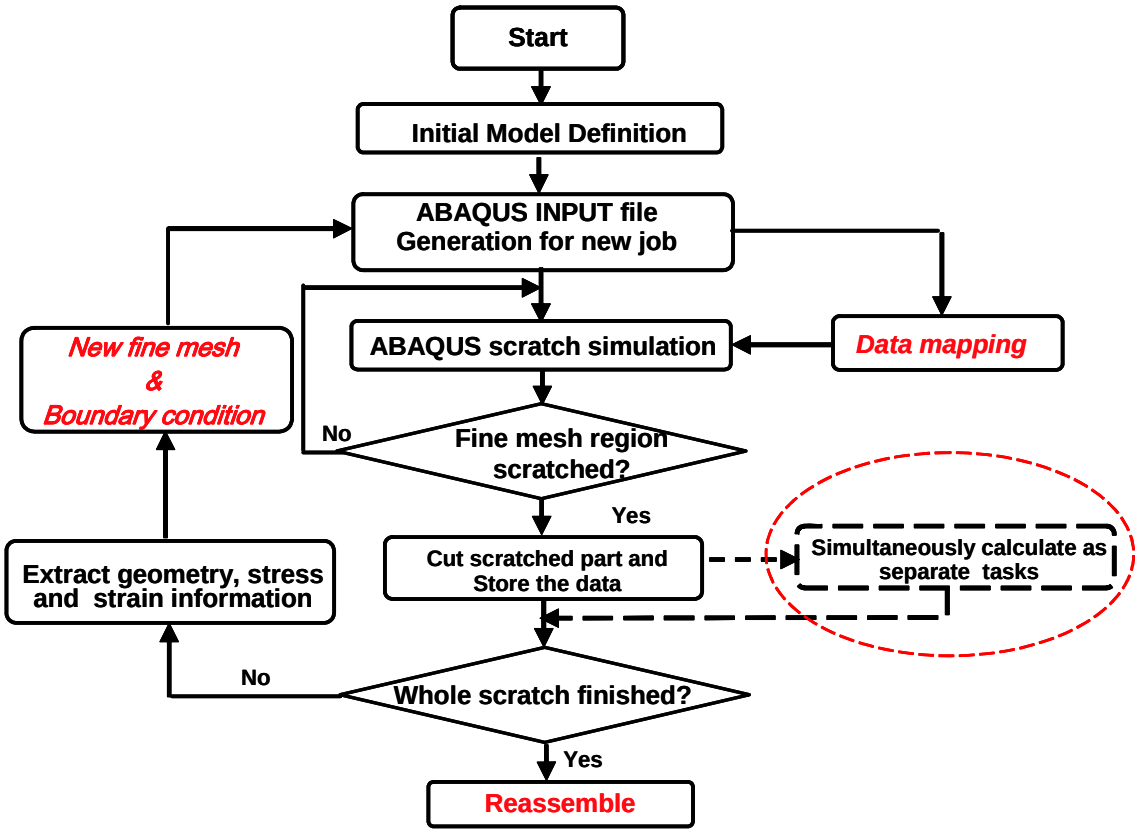

Fig. 4.6. Computational algorithm of the improved MFM method.

Instead of re-coarsening the scratched fine mesh, a virtual cut is made when the strain gradient along the scratch direction reaches the preset criterion. The cut-off region is virtually removed from the model and stored. If the study of visco-recovery phenomena is needed, the cut-off region can be analyzed using another CPU without re-coarsening, while the calculation of the scratch process on the remaining domain continues in separate CPUs. No additional numerical error is introduced since neither re-coarsening nor data-mapping are performed. Thus, the capability of multi-CPU system can be exploited while the level of numerical accuracy is maintained and the visco-recovery mechanisms captured without problems.

After the designated scratch distance or load is reached, a reassembling process is carried out, taking the whole scratched substrate into account. The virtual cutting and reassembling tasks are performed by user-coded Python and FORTRAN subroutines.

4.3.2 Estimation of computation efficiency

The computational efficiency of the MFM method can be estimated. If N steps are executed, the total degrees of freedom of system at the k^{th} step can be taken as n_g*1/N because only the region immediately undergoing the scratch will include fine mesh. Thus, the CPU time of the k^{th} step, T_k is given by

$$T_k = (\frac{1}{N})^P \cdot \frac{T_0}{N} \tag{4.9}$$

The total expected CPU time of MFM method (T_{MFM}) can be approximated by

$$T_{MFM} = (\frac{1}{N})^p \cdot T_0 \tag{4.10}$$

T_{MFM} is equal to T_0/N even if p is taken as one for a conservative estimation. Equation (4.10) shows that the computational efficiency increases significantly using the EFM method.

While the computational cost reduces with more calculation steps, the extra CPU time from data-mapping and I/O processing, which is neglected in the above equations, also accumulates rapidly. The frequency of the refinement operations should be chosen in such a way that the benefit from a large number of calculation steps will not be compromised by the additional CPU cost.

4.4 Efficiency evaluation

An evaluation of the above two new fine mesh methods was conducted using the same parameters for the global fine-mesh approach as defined in section 2.2. A 50 mm x5 mm x3 mm half model substrate and 1 mm diameter spherical tip were used with the solver ABAQUS/EXPLICIT. The same experimentally determined stress-strain curves were also used. For both methods, the fine elements (0.05 mm x0.05 mm x0.05 mm) were adopted for the fine mesh regions, while the remaining regions were generated with a coarse mesh of a typical element size of 0.4 mm x0.4 mm x0.4 mm. For the EFM method, a 3D stress analysis for the scratch numerical model with simulation steps of N=2, 4, 8 and 16 was performed. An evaluation using N =2, 4, 8 and 10 for the improved MFM was also conducted.

Using the relative change of the maximum principal stress at nodal points before and after refinement, the numerical error introduced from the refinement and data-

mapping procedure is evaluated. For the EFM method, the region nearest to the scratch tip experiences the most severe deformation and requires the greatest accuracy. In this study, no geometrical reconfiguration is needed for this region because the fine mesh already exists due to the imposed buffer zone in front of the scratch tip. The maximum error of less than 2.5% actually occurs at the area in front of scratch tip in which the element subdivision procedure is conducted. The error is well within an acceptable range considering the relatively small deformation in that region. For the improved MFM method, due to the virtual cutting process which introduces error near the cut-off line, the maximum error is slightly lager at 4.0%, but still acceptable. One possible solution to reduce the error is to choose a stricter preset criterion of strain gradient.

The result of the benchmark simulation is presented in Fig. 4.7. The estimated computational time with p=1 is also shown in the same plot. The improvement of computational efficiency is significant for both methods and follows the trend of the estimated curves. The actual CPU time of the EFM method rapidly approaches its predicted value, i.e., half of the global fine mesh CPU time, with increased amount of calculation steps. The MFM method shows a better computational efficiency resulting in an actual CPU time of only 41 hours with N=10. This execution time is acceptable for such a complicated 3D FEM simulation and is a vast improvement over the original 139 CPU hours needed for the simulation.

Discrepancies between the estimated and actual CPU execution time are observed for both EFM and MFM algorithms. There are several factors from which the longer CPU hours are needed to complete the tasks. First of all, the computational time

needed to extract the field data information for data-mapping from the output data file of the previous step and construction of the data files for the next step are not included in the estimation. Additionally, extra hard disk I/O process time, which is also nontrivial, has not been included in the estimation. Furthermore, in ABAQUS, no binary access to the output data files is provided other than the Python script, which is a programming language not recognized for its good computational efficiency. Consequently, extra CPU time can rapidly accumulate and lead to such a discrepancy shown in Fig. 4.7. The more refinement steps are utilized, the more extra CPU execution time is required. Thus the larger the discrepancy is observed for both of the proposed methods.

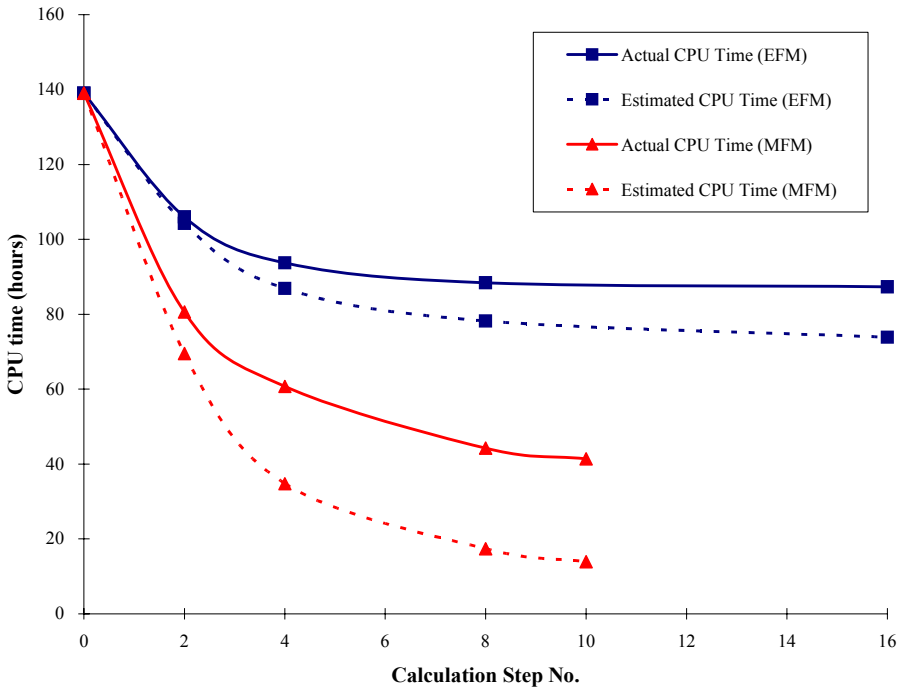

Fig. 4.7. Estimated (dotted line) and actual (solid line) CPU times of the EFM and the MFM methods.

For the EFM approach, because of the existing buffer zone in front of the fine mesh area, the element number for k^{th} step is actually larger than the estimated value of k/N. Thus a longer calculation time is expected. For the MFM method, a strain gradient criterion is used to decide the location from which either re-coarsening or virtual cutting will be performed. For an increasing normal load test where a higher load is applied, a larger remaining fine mesh region is needed to satisfy this criterion. As a result, the element numbers no longer follow the initially estimated value of 1/N; they become much larger as the load level is increased. While larger numbers of elements at the k^{th} step introduce longer CPU execution time, more discrepancies between the estimated and actual CPU execution time are expected for the MFM algorithm.

Using the two fine mesh methods mentioned above, better computational efficiencies can be achieved for modeling polymer scratch behavior. This, in turn, will lead to more extensive investigations of polymer scratch behavior as a function of various surface and material properties, such as ductility, strength, surface roughness, etc. Fundamental understanding on polymer scratch behavior can then be pursued. The parametric studies using FEM modeling, as well as experimental work, are then presented in next chapter to evaluate the key material mechanical and surface properties and the extent of their influence on polymer scratch performance.

CHAPTER V

PARAMETRIC STUDY OF MATERIAL PROPERTIES' EFFECT

For the scratch study, parametric study is particularly important for the material scientists whose common goal is to design high performance scratch-resistant polymers. The purpose of this research is to identify key material and surface properties that influence the scratch performance of polymers as well as examine their relative effect on scratch behavior. FEM modeling, as well as experimental work is executed to reveal the influence of the mechanical and surface properties of a polymer material on its scratch performance.

5.1 Introduction

The challenges facing polymer scratch researchers are the objective quantification of scratch performance and the identification of critical parameters which have significant effect on material scratch performance and hence can be modified to improve the scratch resistance of polymers. An earlier attempt was made to assess the effect of Young's modulus E and the radius of stylus tips on the scratch performance of polymers [12]. Adopting the analytical results by Goodman and Hamilton for elastic materials [7], it demonstrated the detrimental effect of lower modulus and scratch tip radius on scratch depths, whose results are reproduced in Fig. 5.1(a). With the establishment of an ASTM/ISO standard [1,2] on scratch testing and characterization of

polymers and coatings where the recommended diameter of spherical tip is 1 mm, this geometrical parameter shall not be looked into herein. It has also been indicated that for elastic material, a lower value of E can increase scratch depth which will recover after the tip passes by; this is particularly true only for E $\leqslant$ 1.25 GPa and becomes less significant when the modulus is high (Fig. 5.1(a)). Furthermore, the stress plot in Fig. 5.1(b) shows that higher Young's modulus gives rise to a more severe state of stress, which could promote further material damage. Owing to the treatment of a single parameter of Young's modulus for elastic materials, the parametric findings are hence limited in its ability to provide a more realistic prediction on scratch damage of polymers. This indicates a need to adopt a more realistic material constitutive model for polymers, which in turn promises difficulties in obtaining analytical scratch solution.

Considering the difficulty of controlling material properties during polymer processing, performing scratch parametric study via experimentation, although not impossible, demands meticulous planning and attention to testing details to avoid the combinatorial effect from various unintended factors. On the contrary, numerical computation techniques like the finite element method, if executed correctly, can suffice as useful tools in accomplishing such a parametric study with the convenience of changing parameters at ease. FEM modeling and experimental work have been performed to examine the effect of selected material mechanical properties such as Young's modulus, Poisson's ratio, and yield stress, as well as surface properties such as roughness and adhesive friction coefficient, on the scratch performance. The parametric

findings should give useful hints to material engineers in modifying material formulations for better scratch-resistant products.

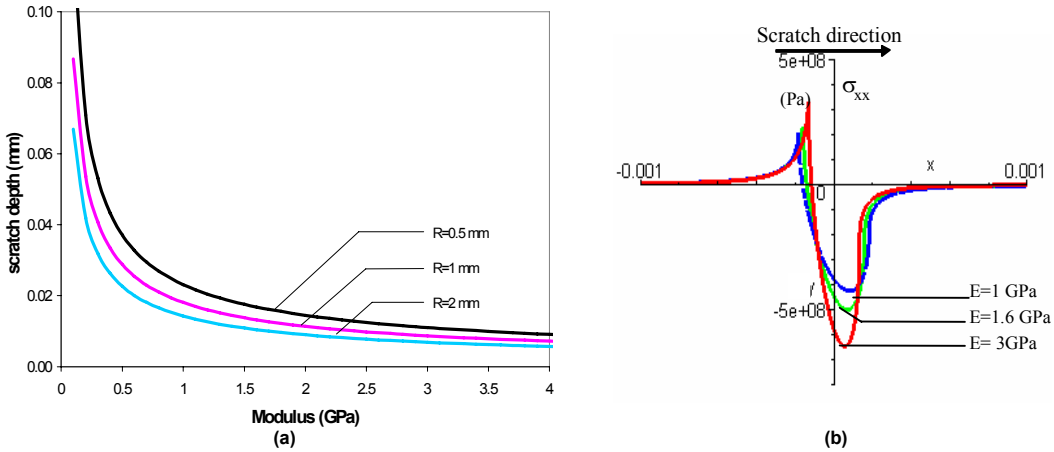

Fig. 5.1. Effect of various parameters on scratch behavior of elastic material: a) instantaneous scratch depth versus Young's modulus; and b) maximum tensile stress on the surface along the center of the scratch path [12].

5.2 Assessment criteria of scratch performance

For our parametric study, it is helpful to clearly define the meaning of scratch performance of materials. Just like in steel or concrete structural designs where ultimate strength design must be satisfied together with the serviceability requirement, scratch performance of materials can also be perceived with the same duality.

Scratch resistance is the inherent material resistance to scratch deformation and derives purely as a material response. An appropriate and straightforward measure of scratch resistance is the tangential force acted on the tip during the scratch process. This tangential force, F_t, arises from the resistance put up by the material against to the scratching action. Due to the presence of frictional force, f, between the tip and the

substrate, the normal force, F_n , and tangential force F_t applied on the tip can be expressed as follows,

$$F_n = \int R_z dA - \int \mu R_x dA$$

$$F_t = \int R_x dA + \int \mu R_z dA \qquad (5.1)$$

where the subscripts "*x*" and "*z*" denote the horizontal and vertical components of the forces, R is the substrate reaction force normal to the contact surface and μ is the coefficient of adhesive friction.

Scratch visibility, on the other hand, is the degree of visual perceptibility of scratch damage by human eyes and can be influenced by the types of surface damage and external factors like color and lighting. To measure scratch visibility of a material, evaluation and imaging tools like scanners, optical and electron microscopes and digital image analyzers like VIEEW® [15] have been used. In line with present work, the use of scratch geometry should suffice to compare scratch visibility. As a result, the residual scratch depth D, defined as the difference between the instantaneous scratch depth and the amount of recovered depth, is considered a useful quantity for numerical modeling to rank scratch visibility and is adopted this study.

As described in Chapter III, an evolution of surface damage can be observed at progressive normal load scratch test. After the initial small "mar", a periodic pattern called "fish-scale" takes place which will eventually become intense enough to scatter light and lead to scratch visibility. Finally, the tip penetrates and removes the material

from the surface. To assess the polymer scratch resistance against visibility and material removal, the onset of fish-scale formation and ploughing are also chosen as experimental criteria to assess polymer scratch performance.

5.3 Numerical parametric study of material properties' effect

Considering the difficulty of controlling the mechanical properties during polymer processing, parametric study of the effect of mechanical properties via experimentation, although not impossible, demands meticulous planning and attention of testing details to avoid the combinatorial effect from various unintended factors. On the contrary, numerical computation techniques like the finite element method, if executed correctly, can suffice as useful tools in accomplishing such a parametric study with the convenience of changing parameters at ease. The commercial finite element package ABAQUS® was utilized to perform the numerical analysis. The modeling technique adopted herein follows those discussed in Chapter III.

Three material parameters, *i.e.*, the Young's modulus, E, Poisson's ratio, ν, and yield stress, σ_y, are considered here. The surface property, described by the friction coefficient, μ, based on the Coulomb's friction law, is also included in this parametric study. Table 5.1 outlines the basis material system and the range of the material and surface properties. The selected parametric ranges are in general relevant to polypropylene. A 3-D elasto-plastic stress analysis was executed for the numerical study and the Von-Mises yielding criterion was used to describe the plastic flow.

Table 5.1. Range of material and surface properties.

Young's Modulus (*E*)	1.0 – 3.0 GPa	$\nu = 0.4$, $\sigma_y = 35$ MPa, $\mu = 0$
Yield Stress (σ_y)	30 – 60 MPa	E = 1.65 GPa, $\nu = 0.4$, $\mu = 0$
Poisson's Ratio (ν)	0.25 – 0.45	E = 1.65 GPa, $\sigma_y = 35$ MPa, $\mu = 0$
Coefficient of Friction (μ)	0 – 0.6	E = 1.65 GPa, $\nu = 0.4$, $\sigma_y = 35$ MPa
Basis material system: E = 1.65 GPa, $\nu = 0.4$, $\sigma_y = 35$ MPa, $\mu = 0$		

5.3.1 Constant normal load scratch

The constant normal-load scratch condition is studied *via* FEM modeling. In our numerical simulation, the normal load keeps 15 N throughout the scratch process.

Figures 5.2 and 5.3 show the effect of changing Poisson's ratio and Young's modulus on residual scratch depth and tangential force F_t, respectively. From these figures, there is negligible influence by the Poisson's ratio on the scratch residual depth and F_t, while a higher Young's modulus both increases residual scratch depth and F_t. As can be readily appreciated, a stiffer material requires more tangential force to move the indenter. For this constant normal load case, the resultant force applied on the scratch tip also increases accordingly, which will in turn influence the stress state and induce larger plastic deformation. With more plastic flow, extensive scratch damage inevitably occurs and can be observed in the form of deeper scratch depths. Therefore, an increase in Young's modulus of a material may not necessarily improve its scratch performance.

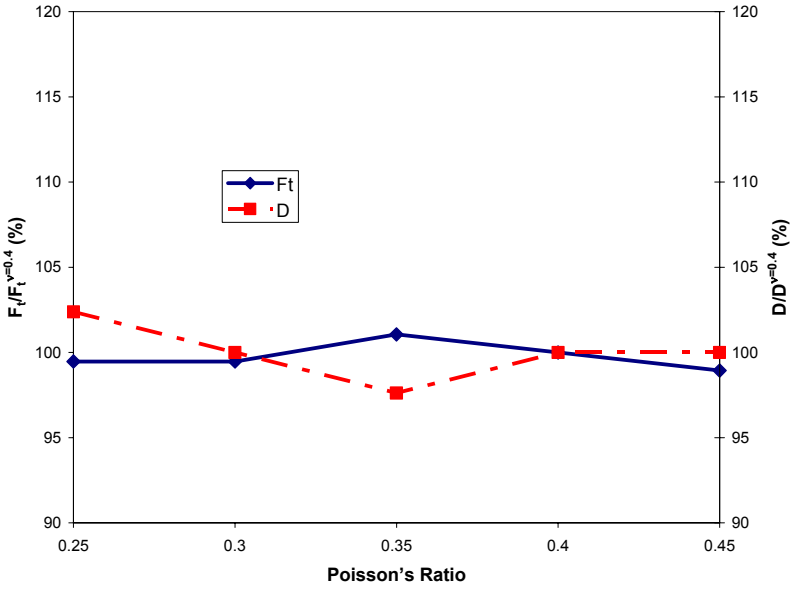

Fig. 5.2. Effect of Poisson's ratio (constant normal load).

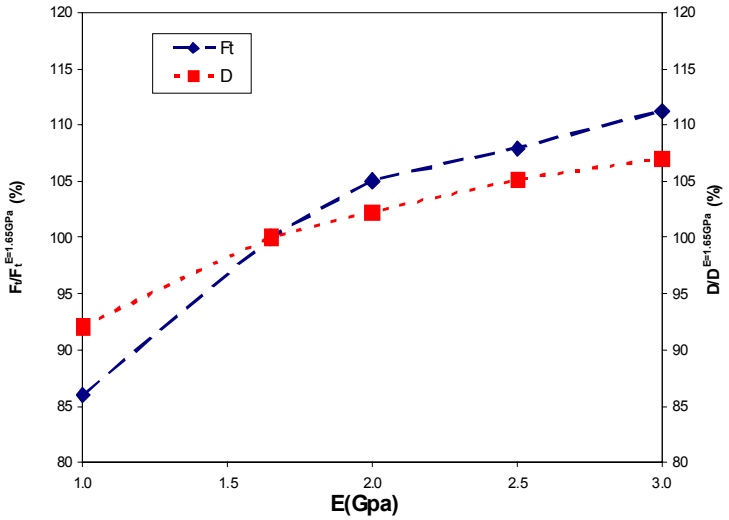

Fig. 5.3. Effect of Young's modulus (constant normal load).

The effect of yield strength on the residual scratch depth and F_t is presented in Fig. 5.4. It can be found that an increase in yield strength of a material results in smaller residual depth and F_t. Both the material strength and surface hardness are indicators of

material's resistance to plastic deformation. They are roughly proportional to each other [30]. Particularly for the elastic-perfectly-plastic material, the material strength is taken as the yield strength σ_y. With a higher yield strength, a better surface hardness can be achieved that in turn induces smaller scratch depths and hence improves the scratch performance of materials. From Fig. 5.3 and 5.4, as the curves level off, it can be observed that the effect of Young's modulus and yield stress become less significant as their magnitude increase.

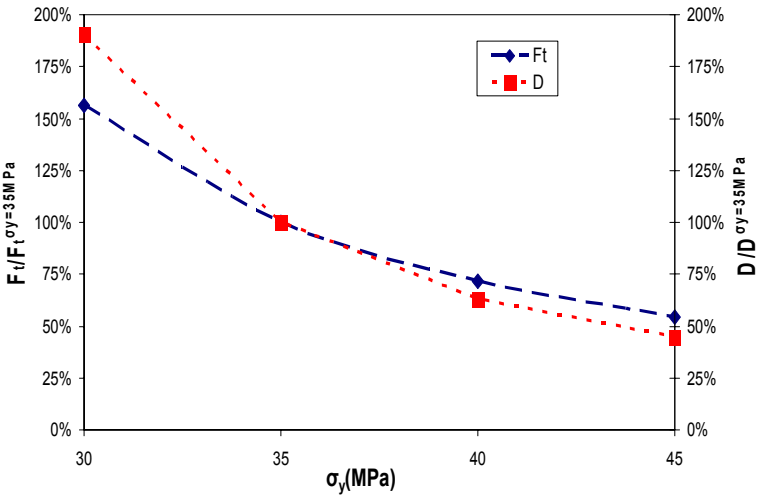

Fig. 5.4. Effect of yield strength (constant normal load).

The effect of the friction coefficient on the scratch performance is shown in Fig. 5.5. When there is more friction between the contacting surfaces, the scratch deformation will result in higher F_t and more residual scratch depth. From Equation (5.1), one can deduce that under the same normal load condition, the vertical component of material resistance force ($\int R_z dA = F_n + \int \mu R_x dA$) will increase with the contribution

of the coefficient of adhesive friction. Even without significant increase of the horizontal force component R_x, the increased resultant force will bring about more scratch deformation.

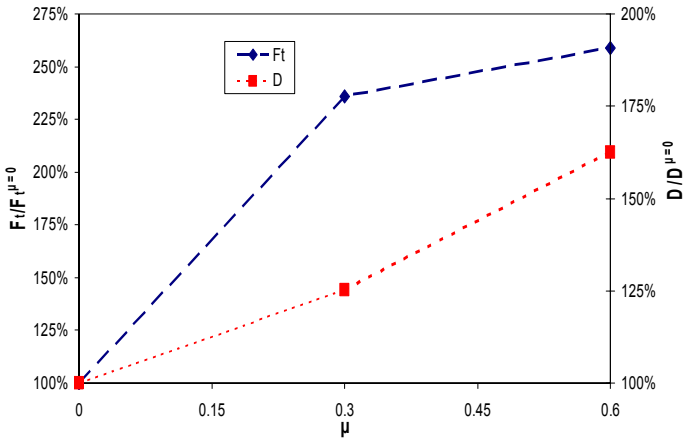

Fig. 5.5. Effect of friction coefficient (constant normal load).

5.3.2 Linearly increasing normal load scratch

As suggested in the ASTM/ISO test standard, the linearly-increasing-normal-load can reveal scratch damage evolution information under different load levels with one single scratch. It is hence of research interest to look into this particular load case. To mimic this load condition, the normal load applied on the indenter increases from 1N to 15N during the scratch stage.

From Figures 5.6-5.9, one can observe the following trends. Again, Poisson's ratio has negligible effect on scratch behavior. There is a direct proportionality between the magnitude of Young's modulus and the tangential force as well as residual scratch depths; higher yield stresses induce smaller F_t and D.

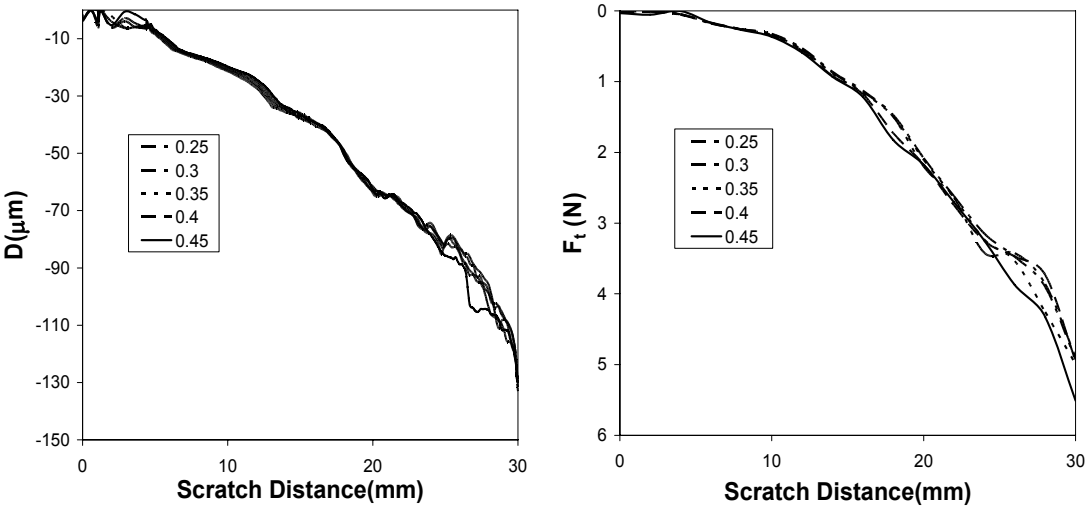

Fig. 5.6. Effect of Poisson's ratio (linearly increasing normal load).

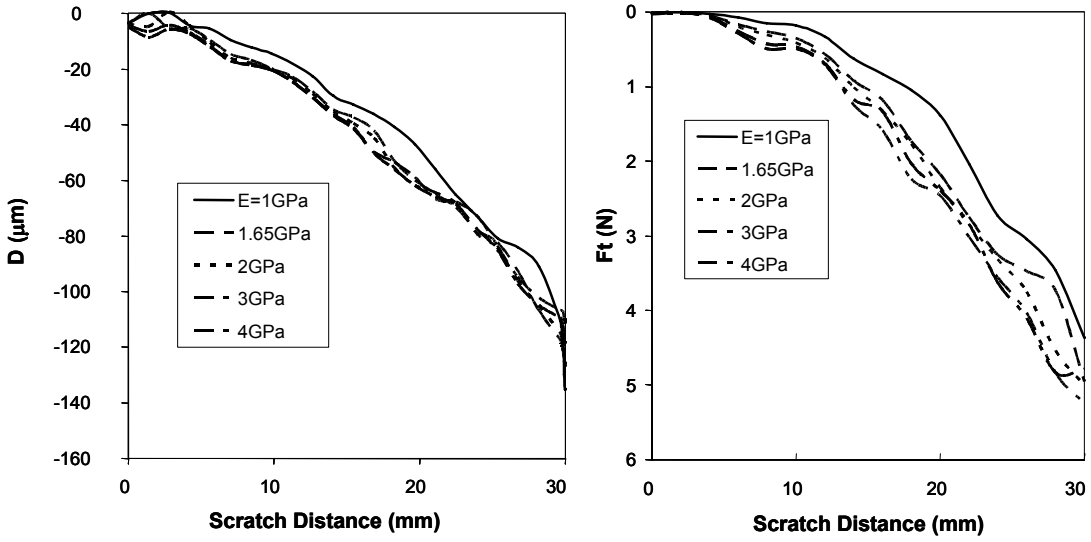

Fig. 5.7. Effect of Young's modulus (linearly increasing normal load).

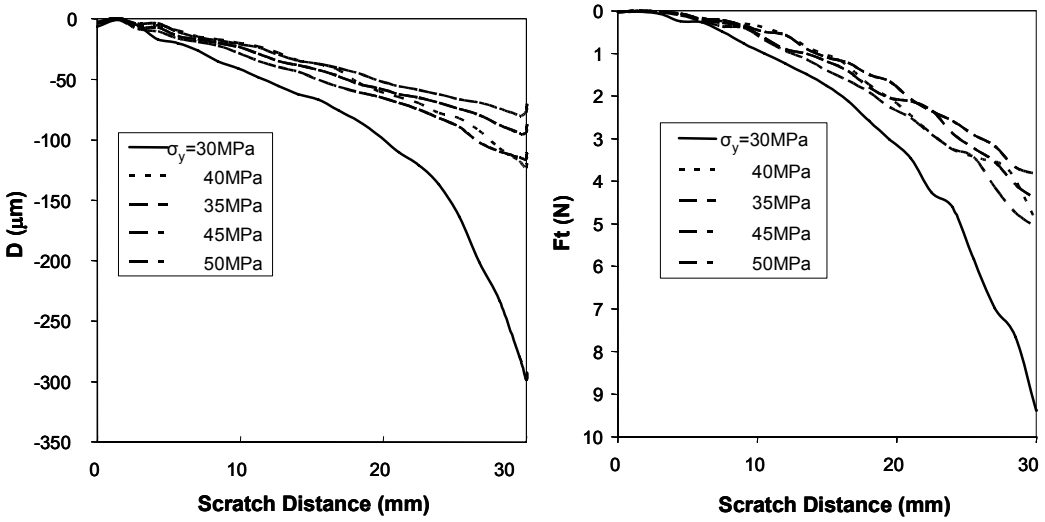

Fig. 5.8. Effect of yield strength (linearly increasing normal load).

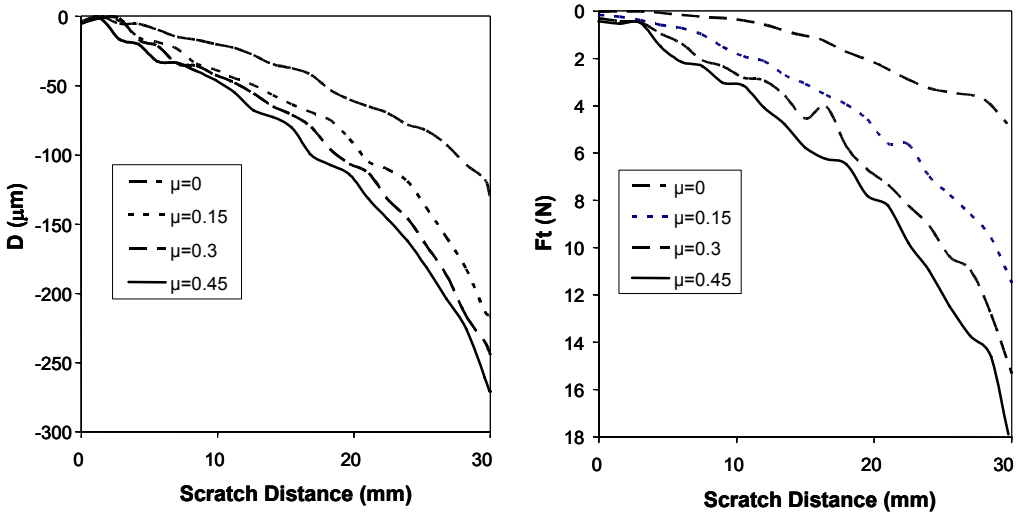

Fig. 5.9. Effect of friction coefficient (linearly increasing normal load).

In view of the results from the two loading cases, the general trend in the parametric effect of the identified material mechanical parameters on the scratch performance is independent of the discussed load conditions and range. The Poisson's ratio has negligible effect on scratch performance while increasing yield stress reduces scratch visibility and improves scratch resistance. However, a higher Young's modulus

may not necessarily bring about an improvement. Under the same normal load condition, a higher Young's modulus, which leads to an increase in the F_t, will induce a larger residual scratch depth. Also, it follows well that reducing the coefficient of adhesive friction has a positive impact on the scratch resistance and visibility of a material.

Experimentally, it is nontrivial to be able to vary only one material mechanical property without simultaneously altering other material parameters. An improvement in polymer scratch performance was observed when a slip agent was added [20]. This finding is qualitatively consistent with the modeling result. Next section, experimental study of the effect of surface characteristics on polymers scratch behavior is presented.

5.4 Experimental study of friction coefficient effect

Concerning scratch behavior of polymers in general, it is intuitively evident that surface characteristics can have significant effects on scratch behavior. In practice, a certain degree of surface roughness (R_a) may be necessary to achieve a specific functionality for certain applications, such as promoting gripping on surfaces or achieving a desired surface gloss. Meanwhile, the friction force is also well known to be strongly dependent of surface roughness. It is accepted by most researchers that the friction force is directly proportional to the actual contact area rather than the nominal one [48]. Here, the nature of asperity contact, which is mainly governed by the roughness characteristics of two surfaces, is the essential attribute to determine the friction behavior. Thus, it is important to identify how surface roughness affects the friction properties, thus the scratch behavior of polymers.

5.4.1 Model systems and surface preparation

Model TPO systems for this study were provided in the form of 3 mm thick injection-molded panels with 2% carbon black pigment to provide sufficient contrast for the scratch visibility investigation. The TPO panels exhibit a surface roughness of about 500 nm upon receipt before any further conditioning except for one system that exhibited a random surface texture referred to as "random animal skin". All the samples were molded and shipped by Advanced Composites, Inc.

To achieve well-controlled R_a, a computer-controlled motor-driven polisher (Struers Abramin 12" disc) was used. The as-received TPO panels were wet-grinded with silicon carbide grinding paper of different grit levels (C60, P180, P500). The sandpaper with coarser grit size was used first followed by the finer grit size paper. On the last grinding step for each achieved roughness level, a piece of fresh sandpaper was used to avoid any build-up of material and contamination. After grinding, the surfaces were cleaned with water and dried with compressed air.

A Dektak 3 surface profilometer (Veeco Metrology, Inc.) was used to characterize the average R_a of all specimens. The radius of the diamond stylus is 12.5 μm and the normal force applied to the stylus is factory-set to a value of 0.5 μN. The horizontal resolution is controlled by the scan speed and scan length. Analog electronics were equipped to detect and amplify the signal from the transducer. Five measurements were made at randomly chosen locations for each sample to obtain an average value of R_a. The summary of R_a of the model TPO systems prepared for this investigation can be seen in Table 5.2.

Table 5.2. Surface roughness values of model TPO systems.

	Surface Characteristic	R_a *(μm)*
Sample #1	As-received surface	0.5±0.02
Sample #2	Wet-grinded	1.7±0.07
Sample #3	Wet-grinded	2.5±0.11
Sample #4	Wet-grinded	4.5±0.21
Sample #5	As-received "Animal Skin" texture	17.8±0.92

5.4.2 Surface friction coefficient measurement and scratch test

To determine μ_s at the interface between TPO model systems and stainless steel scratch tip, it is easier to consider the movement of two flat surfaces in sliding contact. For this purpose, a flat stainless steel tip with 10 x 10 mm square in area and modified to ensure parallelism of the contact surfaces was employed as a friction probe. The friction probe surface has a R_a of 80 nm. The friction probe was installed on the apparatus described in ASTM D7027-05 and tests were conducted under constant normal load levels of 5, 10 and 20 N for a distance of 100 mm at a velocity of 100 mm/s. Three tests were conducted for each system to obtain an average value of μ_s.

Scratch test conditions for this study are in compliance with ASTM/ISO test standards. A commercially obtained stainless steel Grade 25 bearing ball with a diameter of 1mm was used as the scratch tip with a maximum R_a to be 50 nm. A scratching speed of 100 mm/s, a normal load range of 1–40 N, and a scratch length of 100mm were used in the experiments.

The sample surfaces were also scanned at a resolution of 3200dpi with an Epson 4870 Perfection Photo flatbed PC scanner to identify the location of scratch damage transitions. The onset of the normal load value at the point which a transition occurs can be estimated.

5.4.3 Effect of roughness and contact load on surface friction coefficient

The 2D laser confocal images were constructed into a 3D image where the dimensions of the constraining box are all the same. Fig. 5.10 presents the 3-D surface topographies for the prepared model TPO systems. The x- and y-axis length corresponded to the 1270 x 1270 μm scan area while the z-axis length was 126 μm for all constraining boxes. Although no quantitative values of R_a were obtained from these images, various R_a levels still can be easily observed.

Using the surface profilometer measurement results presented in Fig. 5.11, one can find that an increase in Ra results in a decrease of μs which is consistent with the literature [48].

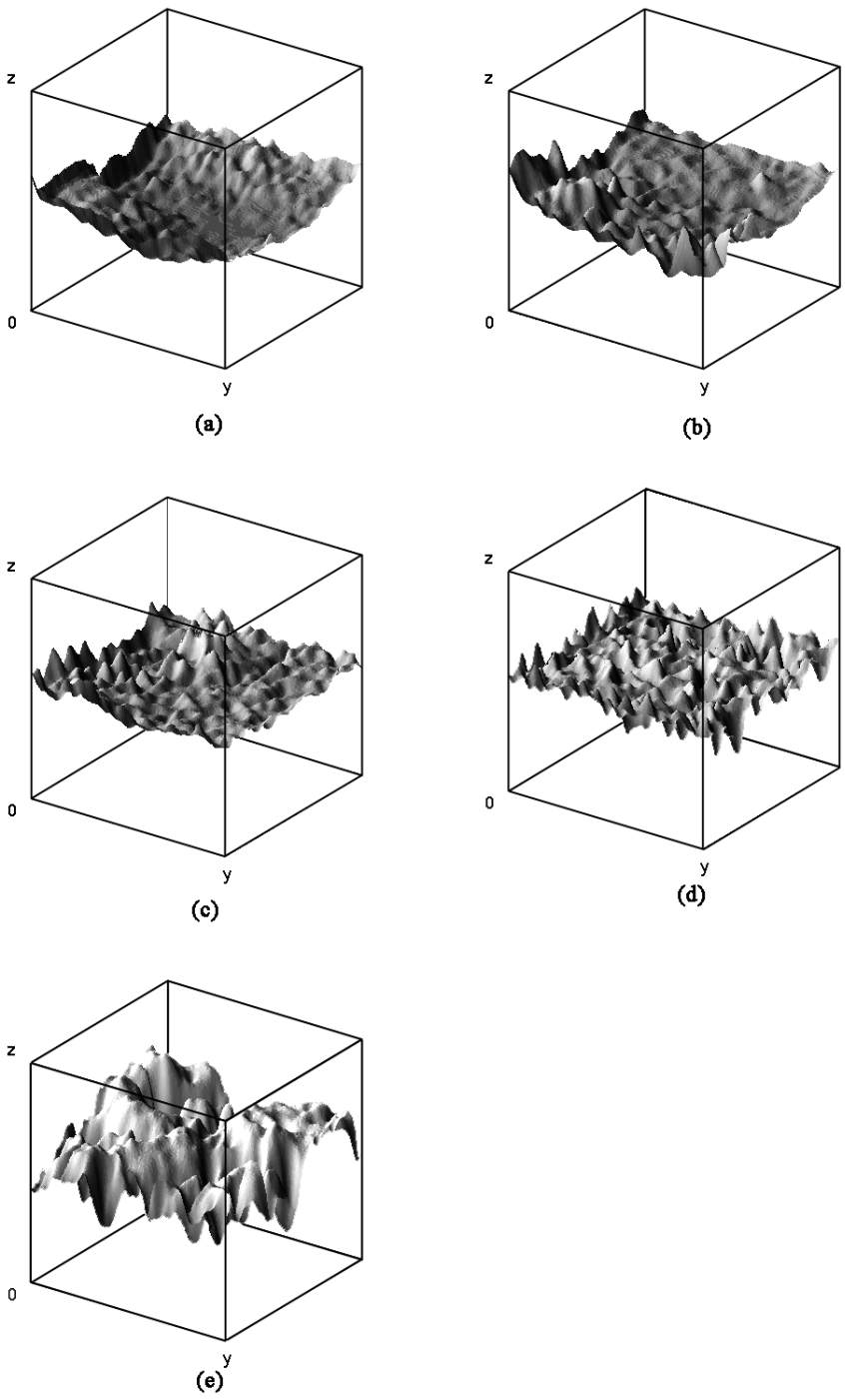

Fig. 5.10. Laser scanning confocal microscopy images of the surfaces of model TPO systems: a)-e) are Sample #1 – Sample #5.

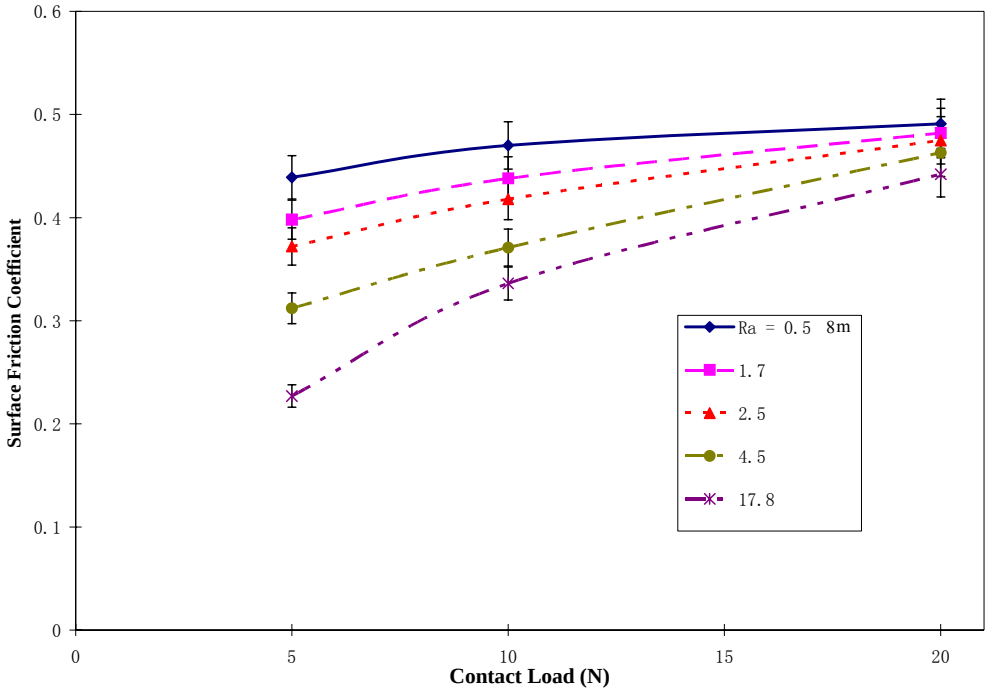

Fig. 5.11. Effects of roughness and contact load on surface friction coefficient.

In addition to R_a, the contact load between the sliding tip and polymer surface has an important influence on μ_s. For each value of R_a, as shown in Figure 5.11, μ_s increases as the contact load increases. For example, the μ_s of Sample #3 increases from 0.37 to 0.47 when the contact load increases from 5N to 20N. Meanwhile, as R_a increases, the magnitude of difference between μ_s increases. The roughest system (Sample #5) shows a 95% increase of μ_s while the least rough system (Sample #1) only exhibits an increase of 13%. It is also observed that at higher contact loads, there is less dependence of the μ_s on R_a. From these results, it is reasonable to expect that with further increase of contact load, the μ_s for all the model systems will eventually plateau to the same value. Similar

dependence of μ_s on contact pressure was also observed for lubricated, rough rolling/sliding between metallic contact surfaces [48].

Both the friction probe and the scratch tip are in the same roughness level and can be considered as smooth when compared to any of the other TPO substrates. As illustrated in Fig. 5.12, the surfaces will only experience contacts at asperity tips. The smooth tip and a substrate that has substantially higher surface roughness will have a less amount of physical contact points. Thus, a smaller contact area is experienced by the scratch tip. As a result, as the contact area decreases, so does the required tangential force. Therefore a smaller μ_s is observed.

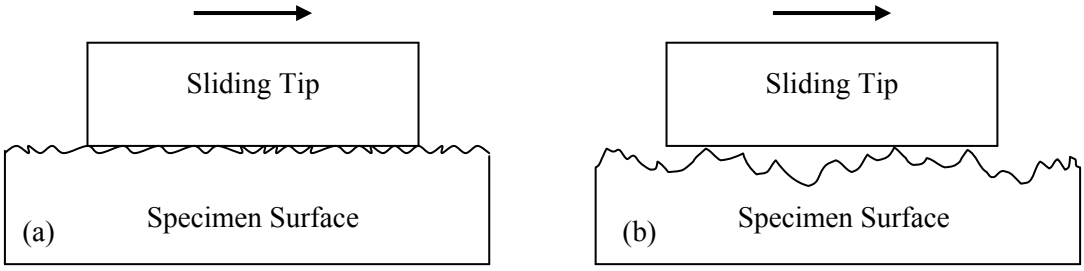

Fig. 5.12. Illustration of roughness effect on the contact area of a smooth sliding tip surface against a surface with: a) low surface roughness; and b) high surface roughness.

When a higher load is applied during the sliding contact, localized compressive deformation of asperities on the TPO surface by the steel tip will take place. Thus, the actual contact area between the sliding surface pair will increase, as will also be the case for μ_s. The smaller the initial contact area is, *i.e.*, the rougher the TPO surface, the more obvious the effect of raising contact load will be to increase μ_s. Eventually, with a high enough contact load, the asperities at the contact will be well-compressed similar to a

scenario where two smooth surfaces are in contact sliding. After this, R_a will show no more significant influence on μ_s.

5.4.4 Correlation of μ_s and SCOF with scratch behavior

To objectively assess the polymer scratch resistance against visibility and material removal, the onset of fish-scale formation and ploughing were chosen as criteria to assess polymer scratch performance. As illustrated in Fig. 5.13, despite the standard deviation increases, the average critical load for the onset of fish-scale formation increases as R_a increases and μ_s decreases. R_a and the onset of fish-scale show a fair correlation with coefficient of determination, R^2, equal to 0.72. This influence of μ_s on scratch performance has been shown not only in pervious numerical simulation but also in experimental work [20,54], where a reduction in μ_s greatly improves scratch performance. This effect is believed to be due to the reduction of contact area with increased R_a. With a decrease in μ_s, the tip will not be able to exert sufficient tangential force to cause drawing of material to form fish-scales under the same applied normal load.

The onset of ploughing shows little, if any, dependence on R_a (Fig. 5.13). The R^2 value between R_a and the onset of ploughing is 0.01. As stated before, a high contact load will bring out the same level of μ_s, regardless of the original R_a. Ploughing is where the scratch tip has penetrated through the surface and beyond the deformed asperities. Here, the main source of scratch resistant comes from the deformation of sub-surface material. Thus, R_a will have no direct influence on the onset of ploughing.

As for scratch visibility, it is noted that the brightness and contrast between the background and the scratch path during a progressive normal load test is, at first, quit subtle. With an increase of the applied normal load, the contrast increases to the extent that human eyes can detect it. The onset of scratch visibility is defined at this point. For a given surface background, the detection of scratch visibility is merely a matter to locate the first position at which the contrast is sufficient to be observed under controlled lighting condition. This onset of visibility becomes convoluted as the background R_a increases, which scatters more visible light and introduces "noise" to mask the onset point. A textured surface such as the "random animal skin" pattern clearly shows this characteristic.

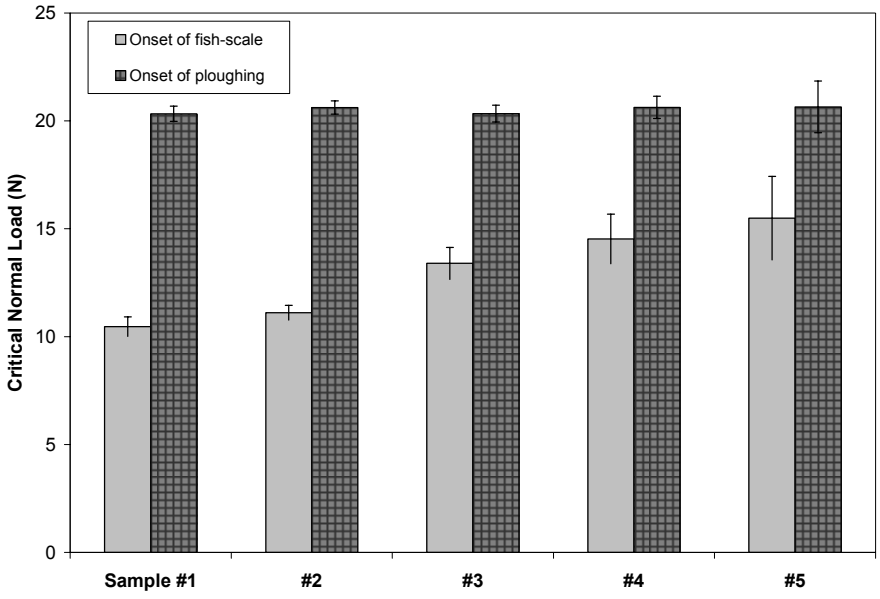

Fig. 5.13. Critical normal load of onset of fish-scale and ploughing for model TPO systems with variation in surface roughness.

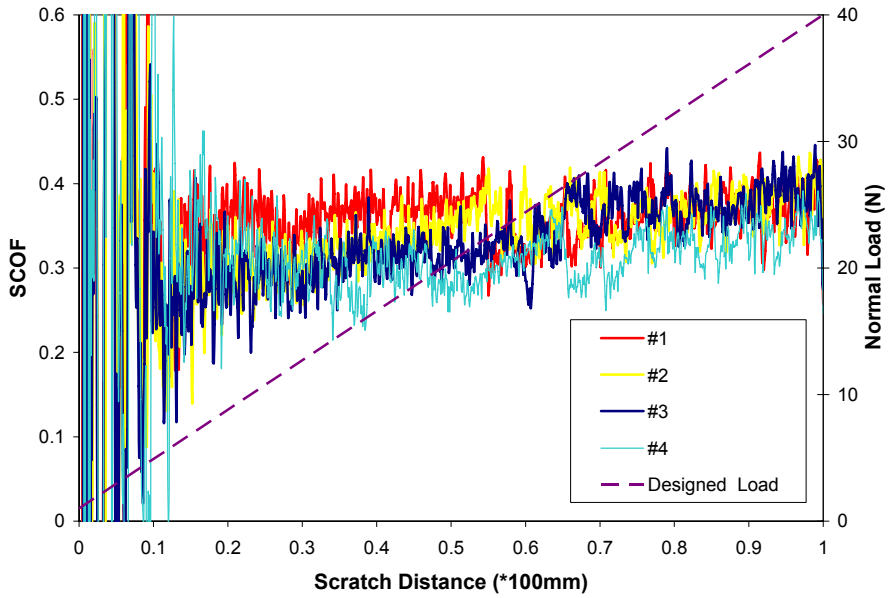

Fig. 5.14. Scratch Coefficient of Friction (SCOF) versus applied normal load for model TPO system with variation in surface roughness.

The plot of SCOF against the applied load clearly shows the effect of contact load on scratch behavior (Fig. 5.14). Sample #5 is not included here due to the fact that the high level of R_a introduces sufficient "noise" which masks the observable changes and conceals the information of other curves. For samples #1~4, a similar tendency can be readily observed. The SCOF increases gradually with the increase of applied normal load. It can be seen that the SCOF curves will finally converge where ploughing begins to take place.

As mentioned previously, SCOF consists of μ_s and μ_r. Under a lower level of applied normal load, the magnitude of scratch-induced deformation is subtle and the friction mainly occurs on the surface while the μ_s dominates. With increasing applied normal load, the SCOF increases not only due to the larger μ_s induced by increased level of

contact load but also the existence of μ_r from inherent material resistance. With the gradually increasing SCOF, the scratch tip will be able to exert sufficient tangential force to cause material drawing to form fish-scale damage above a certain critical normal load. Eventually, the tip will penetrate the surface under a higher level of normal load when the effect of μ_s and R_a diminish. The effect of μ_r, mainly from material ploughing resistance, will become dominant while the SCOF converges to the same value for varying surface R_a.

5.4.5 Approaches for improving polymer scratch performance

The experimental study clearly shows the importance of surface condition (Ra, μ_s and surface texture) on polymer scratch behavior. It is possible to prepare polymer surfaces with controlled Ra to reduce μ_s Doing so will consequently delay the onset of fish-scale and, in turn, the onset of scratch visibility. The inherent roughness of textured random patterns on polymer surfaces will further improve the material scratch performance by masking the scratch-induced visibility. Although more study is needed, optimal surface texture pattern conditions (shape, size and distribution) may exist to achieve good scratch resistance and can be decided upon for specific application using the approach discussed in this work.

This finding is believed to be applicable to other polymeric materials. Actually, surface texturing is a popular industrial practice for automobile interior components to maintain the aesthetic appeal and to "hide" the true onset of visible surface damage. So long as the surface Ra and texture will not compromise the functionality and aesthetics

of the polymer surfaces, it would be beneficial to introduce a surface texture that can withstand high scratch loads for improving scratch resistance against visibility.

5.5 Conclusion remarks

Using the commercial package ABAQUS®, finite element analysis was performed to study the parametric influence of material and surface properties on polymer scratch performance. It was concluded that the tendencies of the effect of the four parameters on the scratch performance is independent of the selected load conditions and range. The Poisson's ratio has minimal effect on scratch performance while increasing yield stress and reducing coefficient of adhesive friction are important ways to positively affect the scratch performance of polymer. The material systems with better scratch performance should induce lower tangential forces on the scratch tip under the same normal load condition.

The effect of R_a and μ_s on polymer scratch performance was studied experimentally. It shows that μ_s increases when contact load increases or R_a decreases. However, the effect of R_a becomes less significant under higher contact loads. At low values of μ_s, the onset of fish scale deformation leading to scratch visibility is delayed significantly. The μ_s and R_a show no obvious influence on the onset of ploughing at which the material ploughing resistance has a dominating effect on scratch behavior when the applied normal load is sufficiently high.

Undeniably, it is challenging for polymer producers to change a material property while maintaining a good control over other material and processing parameters.

This work demonstrates that numerical modeling and experimental work can provide useful guidelines to improve scratch performance of polymer material. The same method can also be employed to identify the combined effect of properties on material scratch performance.

CHAPTER VI

SCRATCH OF POLYMER COATING

To study the scratch behavior of polymeric coatings on soft and hard substrates, an ASTM/ISO standard scratch test is utilized. The stress and strain responses of scratch on polymeric coating are also analyzed using three-dimensional finite element simulation. Depending on different combination of polymeric coatings and substrates utilized, various damage modes can take place, which include coating delamination, transverse cracking and buckling failure. The analysis provides mechanistic insights for the observed polymer coating deformation mechanisms and failure modes.

6.1 Experimental observation

The ASTM/ISO standard for polymer scratch testing has been shown to be effective for bulk polymers. Although the scratch damage features for polymer coating systems are significantly different from the bulk, the standardized scratch test is still expected to be useful for the study of coating scratch behavior.

6.1.1 Model coating systems

To study the scratch behavior of polymer coatings, two model coating systems have been investigated. One is a soft coating on a hard substrate, i.e., an acrylic coating on steel substrate. The thickness of the acrylic coating layer is approximately 60 μm and that of the steel substrate is 813 μm. The details of the sample preparation can be found elsewhere [25]. The other is a hard coating on a soft substrate, i.e., a hard polyurethane

coating on a polypropylene substrate. The thickness of the polyurethane coating and the polypropylene substrate are approximately 70 μm and 3 mm, respectively. The samples were provided by Japan Polypropylene Corp., Yokkaichi, Japan.

6.1.2 Scratch testing and analysis

Scratch tests are performed at room temperature using a custom-built scratch machine described in Chapter III. A linearly increasing normal load from 1N to 50N is imposed on the scratch tip, which moves at a speed of 100 mm/s. The scratch length is set at 150 mm.

As described in previous chapters, the flatbed PC scanner, optical microscopy and scanning electron microscopy are utilized to investigate polymer coating damage mechanisms.

6.1.3 Acrylic coating on steel substrate

The scratch behavior for acrylic coating on steel substrate was experimentally investigated. A typical scratched surface is shown in Fig. 6.1. The discontinuity of material properties at the interface of coating system leads to scratch damage modes different from the bulk material. Three damage features, *i.e.*, delamination, transverse cracking and buckling-induced damage can be identified. In zone 1 (Fig. 6.1a), the coating layer begins to delaminate. In zone 2 (Fig.6.1b), the coating layer cracks under the center of the indenter tip and propagated outward at an angle. As the normal load increases, the buckling-induced delamination takes over as the main damage mechanism (zone 3). Subsequently, the coating layer is removed and the substrate is exposed directly to the contact with the indenter (Fig. 6.1c). It is noted that the occurrence

sequence of the transverse crack and adhesive delamination depends on coating ductility, adhesive strength, and coating thickness.

a)

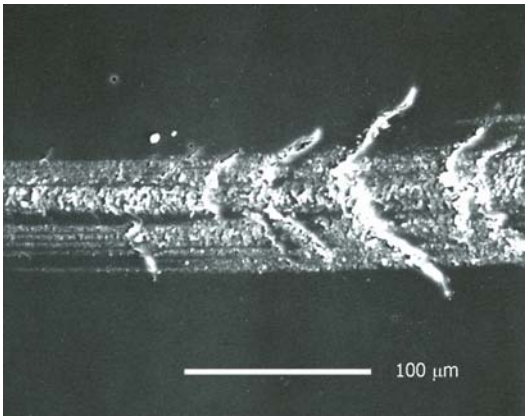

b)

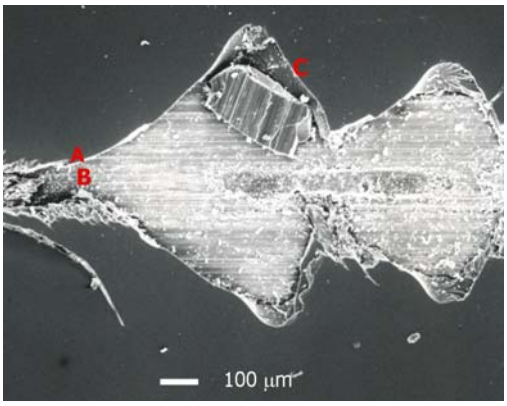

c)

Fig. 6.1. Typical scratch damage modes of the acrylic-steel coating system: a) three damage zones (zone 1: delamination, zone 2: transverse cracking, zone 3: buckling damage); b) onset of transverse cracking; and c) buckling damage.

6.1.4 Polyurethane coating on polypropylene substrate

For the polyurethane-polypropylene system, i.e., a hard coating on a soft substrate, it shows totally different scratch damage modes from the acrylic coating on steel (Fig. 6.2). Smooth indentation can be observed early in the scratch process (Fig. 6.2b). Neither delamination nor buckling-induced damage is observed. Two types of cracks, i.e., hair-line radial cracking and severe cracking (Fig. 6.2c), are observed before the ultimate failure of the coating system. As the load is further increased, the scratch tip will be ploughed into the substrate and subject it to scratch deformation and damage (Fig. 6.2d).

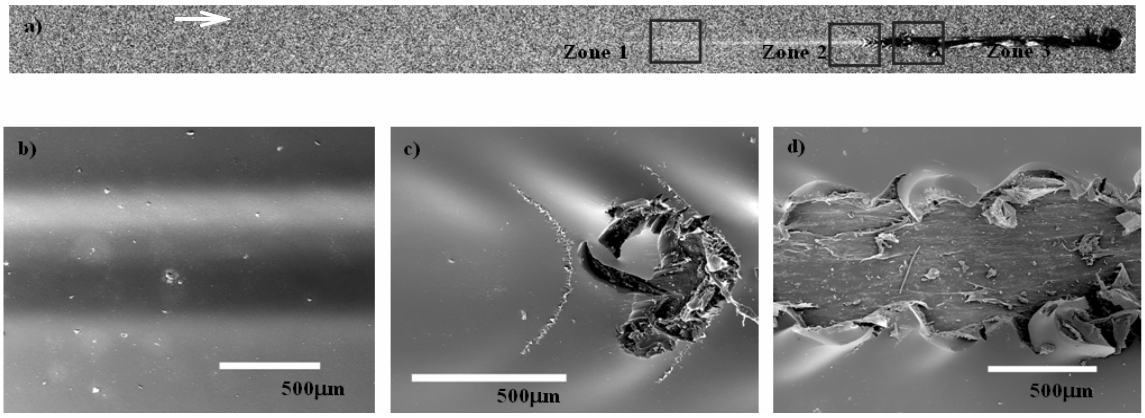

Fig. 6.2. Typical scratch damage modes of the polyurethane-polypropylene coating system. a) the scanned image of scratched sample; b) the smooth indentation (zone 1); c) the cracking (zone 2); and d) the tip penetration and scratch onto the substrate (zone 3).

As illustrated in Fig. 6.3, coating thinning occurs under the scratch tip, which moves outward, while the side groove pile-up exists due to the extrusion of the coating materials. For a soft coating on a hard substrate (Fig. 6.3a), only the coating layer experiences significant deformation. With the increase of applied normal load, the

adhesive interface between the coating and substrate will be severely strained and cause debonding. As shown in Fig. 6.3b, the absence of delamination here can be attributed to the combination of hard coating and soft substrate scenario. Here the underneath substrate significantly deforms and the stress can be easily dispersed underneath. Even under a high loading level, the strain magnitude of the interface between the coating and substrate is much smaller than those of a soft coating on a hard substrate. As a result, delamination of coating layer cannot easily occur here.

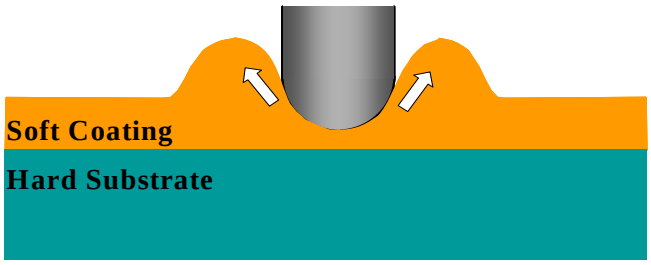

a)

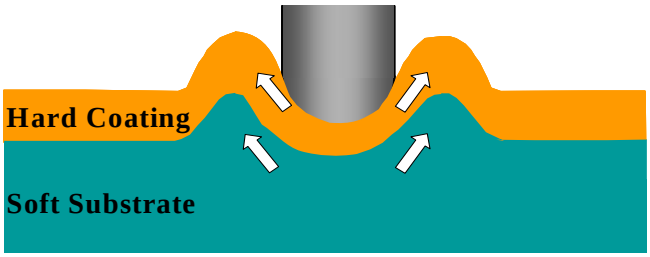

b)

Fig. 6.3. Illustration of the coating thinning and pile-up under scratch: a) a soft coating on a hard substrate; and b) a hard coating on a soft substrate.

6.2 Numerical modeling

Numerical modeling can provide insight into the mechanics that corresponds to the experimentally observed scratch phenomena of coating systems [69-76]. The 3-D

FEM models similar to previous chapters, with coating thickness of 60 μm and 70 μm for acrylic coating and polyurethane coating, respectively, are used here to understand the polymer coating scratch and to explore how the soft and hard substrates influence the scratch damage mechanisms.

To simulate the progressively increasing normal load scratch condition, the normal load applied on the indenter is linearly increased from 1N to 50N during the scratch process. Perfect bonding between the coating layer and substrate is assumed before the debonding happens. The friction coefficient between the indenter and coating is 0.25. The elastic-pure-plastic material type is adopted for the steel substrate, which is adequate since no yielding is expected. The acrylic coating, polyurethane coating and polypropylene substrate are described by piecewise linear elastic-plastic stress-strain curves. The key material properties, which provided by material manufacturers, are shown in Table 6.1.

Table 6.1. Material properties of polymer coating systems.

	Hard substrate		Soft substrate	
	Acrylic	Steel	Polyurethane	Polypropylene
E (GPa)	3	200	2.5	1.65
ν	0.35	0.3	0.35	0.4
σ_y (MPa)	100	300	104	50
ρ (g/cm3)	1.25	7.8	1.2	0.90

6.2.1 Acrylic coating on steel substrate

The variation of the Von-Mises stress field for the acrylic-steel coating system is shown in Fig. 6.4. The spherical tip is removed to clearly display the stress field. The initial position of interface between the coating layer and substrate is illustrated by the dashed line, which does not change since there is no significant deformation of the steel substrate. The coating is plastically deformed; the coating thinning and side groove pile-up become significant with the increase of the applied normal load level.

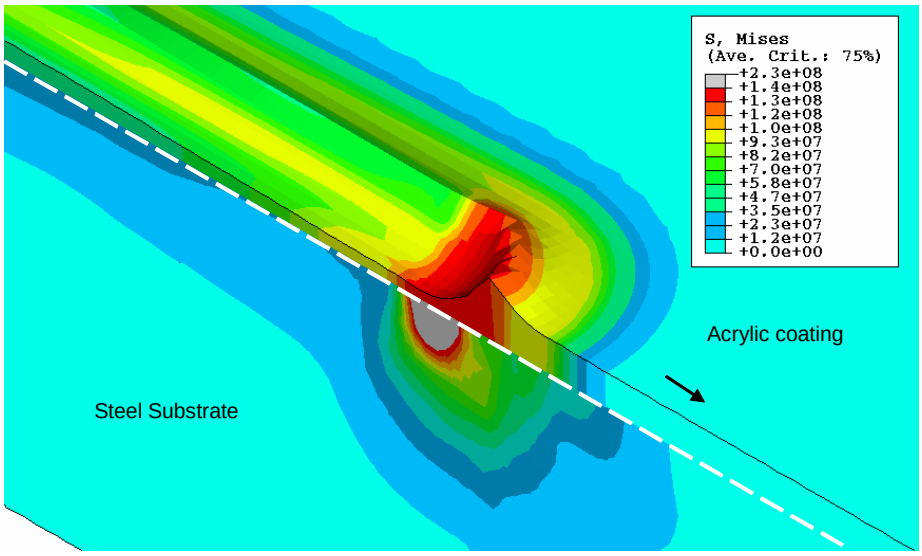

Fig. 6.4. Von-Mises stress field for the acrylic-steel coating system.

It is apparent that the size of the plastic deformation zone increases with the increased normal load while the severe plastic deformation of coating layer concentrates in the area under the tip and around it. The substrate deformation is negligible since steel is much stronger than the coating layer.

The maximum principal stress (σ_1) is used as the main failure indicator in this study. The stress fields at different scratch locations, i.e., normal load levels of 13N, 32N and 45N, are extracted from the FEM data and plotted in Figs. 6.5-6.7, respectively. For clear illustration, only the direction of the corresponding peak maximum principal stresses is shown.

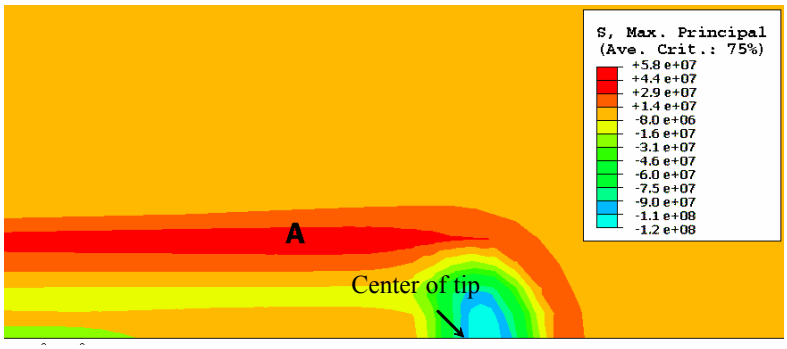

a)

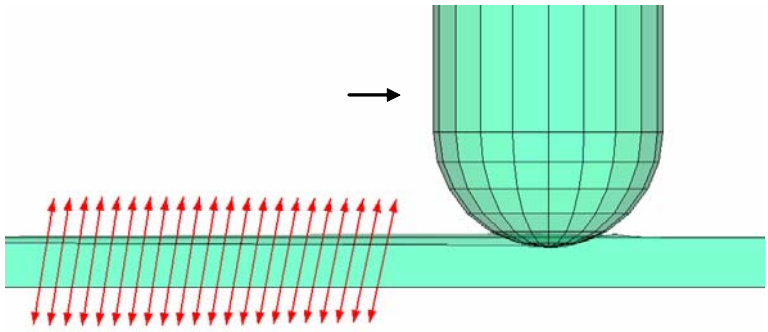

b)

Fig. 6.5. Maximum principal stress for the acrylic-steel coating system at 13N: a) the contour plot (top view); and b) the direction of stress (side view).

Under the normal load of 13 N, the peak value of σ_1 is located behind the scratch tip and is away from the middle of the scratch path (area A in Fig. 6.5a). The direction of the σ_1 is near normal to the interface plane (Fig. 6.5b). If it is higher than

the interfacial adhesive strength, the coating will be peeled off to cause delamination. The directionality of σ_1 also tells that the debonding induced by scratch is mixed mode damage other than a simple Mode I or Mode II failure.

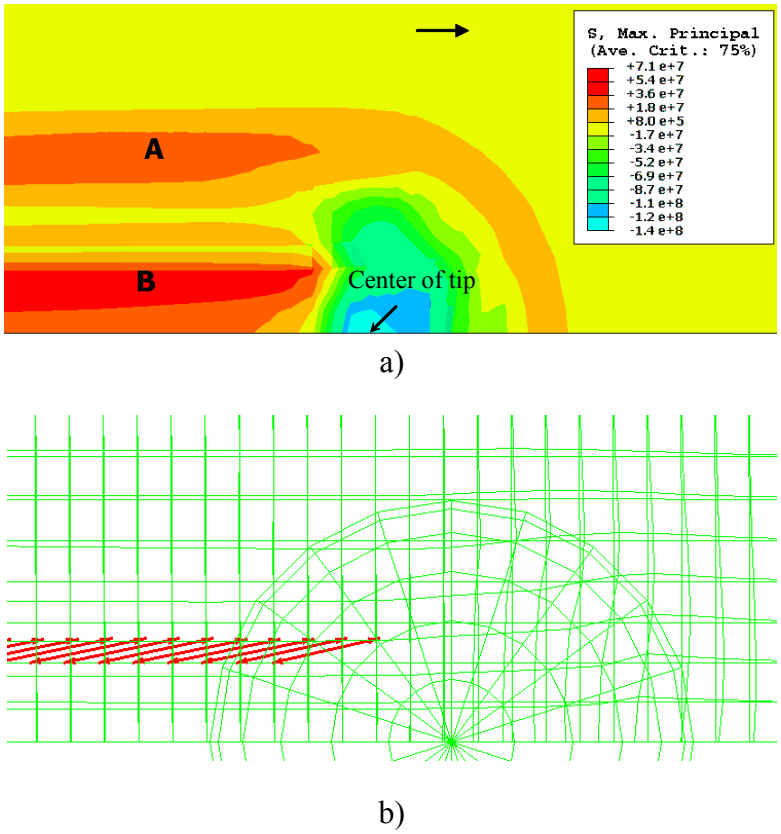

Fig. 6.6. Maximum principal stress for the acrylic-steel coating system at 32N: a) the contour plot (top view); and b) the direction of peak stress at area B (top view).

Under the normal load of 32 N, the second peak value of σ_1 develops behind the tip (area B in Fig. 6.6a). It is closer to the middle of the scratch path. Accordingly, possible damage is expected to occur near the scratch path. As illustrated in Fig. 6.6b, through the thickness of the coating layer right behind the indenter, σ_1 tilts at an out-of-plane angle of about 8º and at a transverse angle to the direction of scratch. This could

promote inlayer failure via transverse cracks which will propagate outward once occurred.

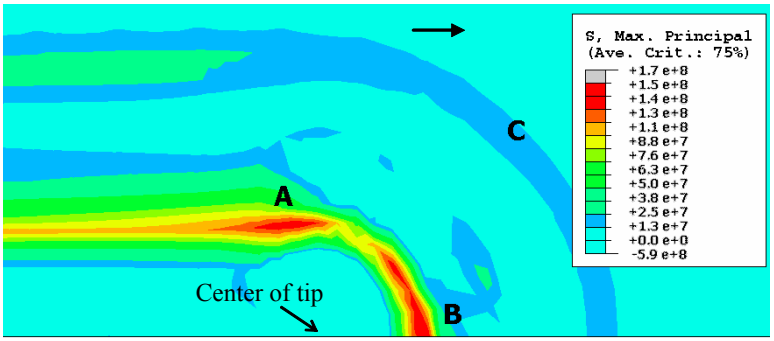

a)

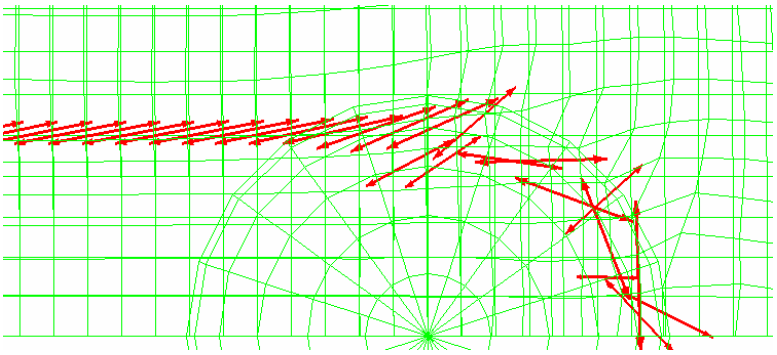

b)

Fig. 6.7. Maximum principal stresses for the acrylic-steel coating system at 45N: a) the contour plot (top view); and b) the direction of stress (top view).

At the normal load of 45 N, a complex stress state exists in the region close to the scratch tip where buckling-induced damage of the coating occurs. There are two peak values of σ_1, areas A and B, at which σ_1 exhibits a small out-of-plane angle tilt. Two possible damage initiation locations are expected (Fig. 6.7a). Area A is at the rear side of scratch path and area B is in front of the scratch tip. The σ_1 also exist a secondary peak (area C). The coating material at points A and B will crack and the damage will develop

from point A and propagates until arriving at area C, which shows an arc shape. Once transverse cracks and delamination coexist and are full developed, the buckling-induced delamination is most likely to become the main failure mode.

With a stronger interfacial adhesion, the transverse cracking in the coating layer could occur before debonding takes place. Furthermore, delamination and transverse crack will occur before the formation of buckling damage. If the interfacial adhesion is strong, which prevents delamination, or the coating is tough, which avoids transverse cracking, then buckling may not happen.

6.2.2 Polyurethane coating on polypropylene substrate

The Von-Mises stress fields of the polyurethane-polypropylene coating system at various load levels are shown in Fig. 6.8. The initial position of interface between the coating layer and substrate is marked by the dashed line. Other than the acrylic-steel coating system, plastic deformation of the polypropylene substrate cannot be neglected.

At a low loading level, the residual scratch depth is dominated by the deformation of coating layer. Actually, one can find that the stress distribution of polyurethane coating at a low load level is similar to that of the scratch on bulk polymers since the scratch tip cannot sense the substrate underneath the coating layer yet. At a higher load level, more contribution for scratch residual depth comes from the soft substrate plastic deformation since the load is transferred through the hard coating layer and dispersed into the substrate.

Fig. 6.9 shows the top view of the σ_1 field at different scratch normal load levels, i.e., 13N, 32N and 45N, respectively. The location of the peak σ_1 migrates with the

increase of normal load. The peak area formed in front of the tip contact (area A in Figs. 6.9a and 6.9b) will induce hair-line radial cracks. The second peak area of σ_1, which is tilted at a small out of plane angle, gradually develops behind the scratch tip as the normal load increases (area B in Fig. 6.9b).

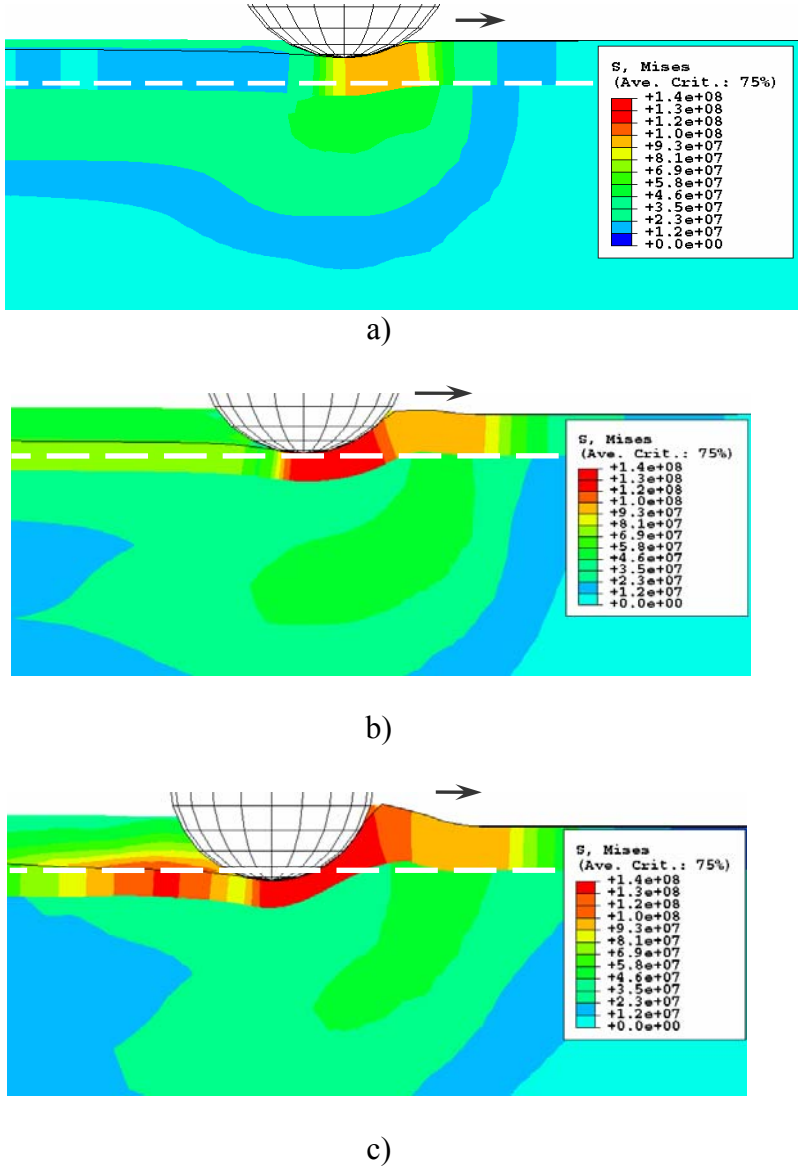

Fig. 6.8. Von-Mises stress field for the polyurethane-polypropylene coating system at the normal load of (side view): a) 13N; b) 32N; and c) 45N.

At a high load level (45 N), the second peak area of σ_1 becomes dominant with a direction shown in Fig. 6.10. This large tensile stress behind the indenter will promote severe inlayer failure through the thickness of the coating layer. Then, the scratch tip will penetrate through the coating layer and scratch the underneath substrate directly.

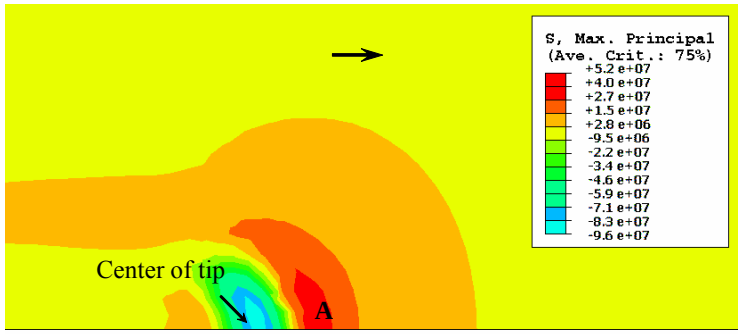

a)

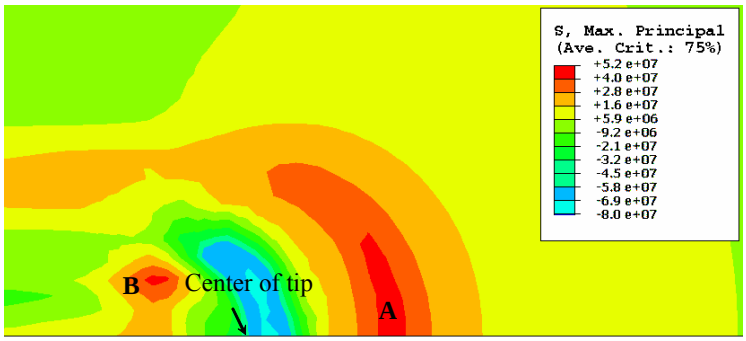

b)

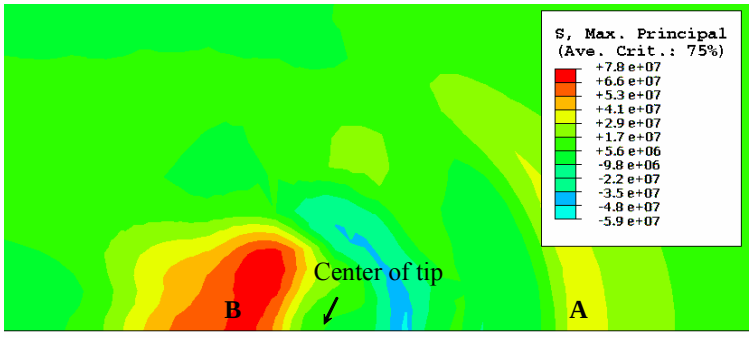

c)

Fig. 6.9. Maximum principal stress for the polyurethane-polypropylene coating system at the normal load of (top view): a) 13N; b) 32N; and c) 45N.

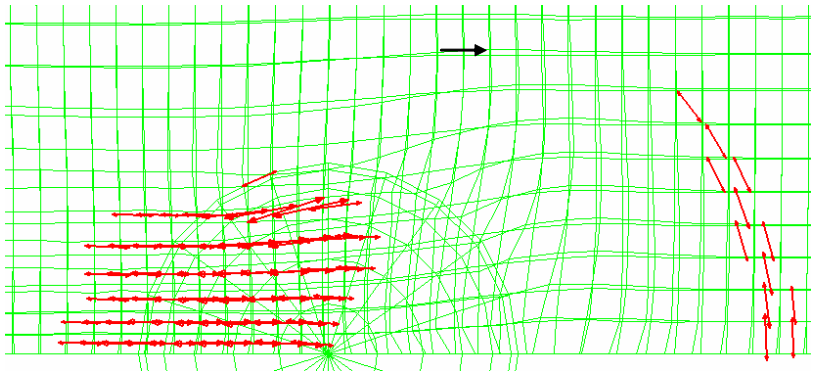

Fig. 6.10. Direction of the maximum principal stress of the polyurethane-polypropylene coating system at a normal load of 45N (top view).

It is worthwhile to mention that the possible damage modes of the polyurethane-polypropylene system were first predicted by the modeling work and then validated by the scratch experiment.

6.2.3 Quantitative evaluation method of polymer coating scratch resistance

Since the stress distribution and deformation obtained from numerical simulation are well correlated with the scratch experiment observation, it is possible to quantitively evaluate the polymer coating performance with the help of the scratch test and the FEM simulation.

First, the critical scratch normal load value of the specific damage mode is determined experimentally. For a linearly progressive normal load scratch test, the following equation can be employed [20]:

$$F_c = F_0 + \frac{x}{L}(F_f - F_0) \qquad (6.1)$$

where F_c is the value of the critical normal load, L is the total scratch length, x is the distance from the beginning of the scratch to the onset location at which a scratch

damage transition is observed, and F_0 and F_f are the initial and final applied normal loads, respectively.

While it is not possible to experimentally determine the local critical stress values, FEM modeling is useful for estimating the corresponding stresses based on the specific experimentally observed damage modes and their locations. As an illustration, the calculated strengths for various damage modes of the acrylic-steel coating system are shown in Fig. 6.11, together with the corresponding critical normal loads at the onset of damage. The values of the damage strengths calculated *via* FEM appear to be reasonable.

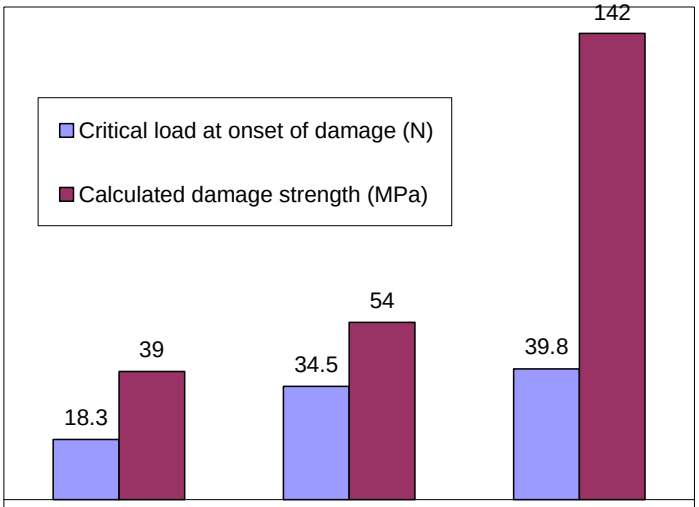

	Delamination	Transverse Cracking	Buckling
Critical load at onset of damage (N)	18.3	34.5	39.8
Calculated damage strength (MPa)	39	54	142

Fig. 6.11. Critical load and strength of various damage modes for the acrylic-steel coating.

It should be noted that there are still many factors to be considered for the above approach to become quantitatively accurate. These factors include: (1) refined

constitutive equations and accurate material properties for the coating and substrate, (2) appropriate algorithm to describe interfacial debonding, and (3) valid failure criteria for the coating and substrate. Additional experimental and modeling work is underway to address the above concerns.

6.3 Conclusion remarks

The linearly progressive normal load scratch test is effective for the understanding and evaluation of polymer coating performance. The scratch damage mechanisms of two polymeric coating systems, i.e., acrylic-steel (soft coat on hard substrate) and polyurethane-polypropylene (hard coat on soft substrate), are studied. With the aid of FEM modeling, the mechanisms of various scratch damage modes are correlated with the material properties and the corresponding stress fields. The location and occurrence of specific scratch damage can be predicted based on the known material properties. Combining ASTM/ISO scratch method and FEM modeling, a quantitative evaluation methodology of polymer coating system is proposed. The critical strength for the occurrences of various scratch damage modes can be obtained accordingly.

CHAPTER VII

SCRATCH DAMAGE MECHANISM

It is important to note that, during the ASTM/ISO based linearly increasing normal load scratch test, the stress and strain magnitudes exerted along the scratch path do not increase linearly, even for linear elastic material [12]. For polymers with complex material constitutive behaviors, the development of stress and strain fields throughout the scratch test is inevitably much more complicated and can only be described numerically. To elucidate the evolution of the scratch damage formation, numerical analysis, such as FEM, is essential.

7.1 Stress state of polymer scratch

The stress and strain states experienced by the polymer substrate are extremely complex. To understand the mechanistic origins behind the various observed scratch damage features, 3D FE analysis was performed to simulate the polymer scratch process. To model generic polymer material, a piecewise linear stress-strain curve was constructed based on the experimental data of TPO (Fig. 7.1) [64]. The stress softening and strain-hardening characteristics are clearly illustrated.

The maximum principal stress contours and their orientations under low, moderate and high scratching normal loads are plotted in Fig. 7.2. Here, only the top layer of the material elements is plotted and the scratch tip is removed for better visualization. The location of the tip center is indicated by the bold arrow.

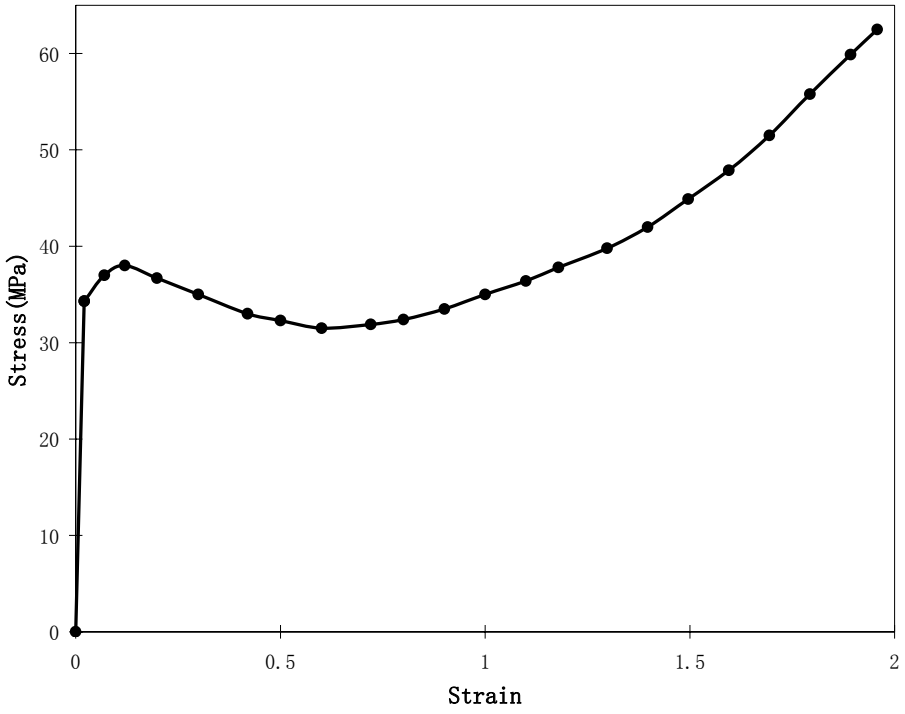

Fig. 7.1. Piece-wise linear stress-strain curve for a model TPO.

The material beneath the front portion of the scratch tip (region A) always experiences a compression. The compressive stress magnitudes are 23, 34 and 37 MPa for the applied normal loads of 8, 14 and 20N, respectively. Meanwhile, a maximum principal stress of 17 MPa under the normal load of 8 N is developed behind the scratch tip (region B) and increases to 35 and 40 MPa as the normal load is further increased to 34 and 37 N, respectively. As has been shown in an actual scratch test and the numerical simulation here, the material is raised in front of the scratch tip during the scratch process (region C). As the applied normal load is further increased, another barely noticeable tensile region under small normal loads has now become significant here. It

increases to 18 and 48 MPa at normal loads of 14 and 20N, respectively, and develops as another possible region for the formation of brittle-type of scratch damage.

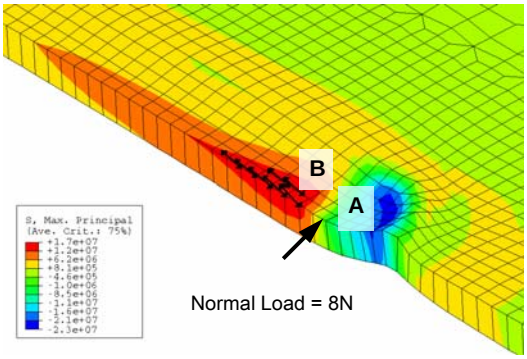

a)

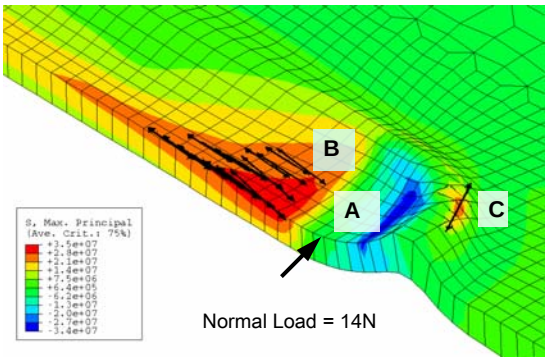

b)

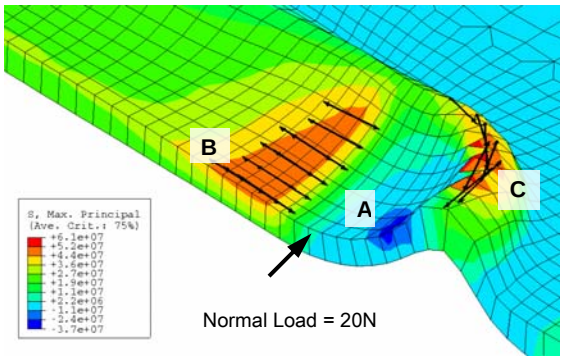

c)

Fig. 7.2. Maximum principal stress contour plots at normal loads of: a) 8N, b) 14N, and c) 20N.

Due to the scratch tip movement, the material in front of the tip quickly transits from a tensile condition (region C) to a compressive condition (region A), and then back to a tensile condition (region B). Inherent to the polymer scratch process, the scratch-induced damage mechanism(s) incurred will likely be influenced by the stress state, stress magnitude, and material characteristics the polymer experiences and possesses. These factors are discussed in detail below.

7.2 Ductile deformation vs. brittle damage

To study the different damage modes and their evolution processes with an increasing normal load, knowledge on the stress state and magnitude the material experiences near the scratch tip is necessary. The relationship between the scratch normal load and the Von-Mises stress at region A, which is closely related to the experimentally observed ductile deformation, is plotted in Fig. 7.3. To illustrate the size of the permanent deformation zone, the residual scratch depth and width are also presented in Fig. 7.3.

While the Von-Mises stress increases with the normal load from the very beginning and quickly reaches beyond the yield point under a relatively small normal load due to a small tip contact area, the scratch-induced plastic deformation is quite subtle at this stage, exhibiting only 20 μm of residual scratch depth and 120μm of residual width at 5N of normal load. This level of deformation is barely visible to the naked eyes. This is the reason why at most only mar damage can form at the beginning of the scratch process. When the applied normal load is increased, the Von-Mises stress

magnitude will reach a maximum and drop slightly due to the strain softening nature of the polymer after yielding. Then, the stress magnitude increases again because of the strain hardening effect. The fish-scale damage tends to occur between the yielding and strain hardening region. Finally, the stress level reaches the ultimate strength of the material and the material removal process begins. For the utilized numerical model, the scratch-induced plastic deformation, reflected by the observed residual scratch depth and scratch width, will continue to evolve since the elements do not fail as the normal load is further increased. However, in reality, the material will fail and lead to material removal.

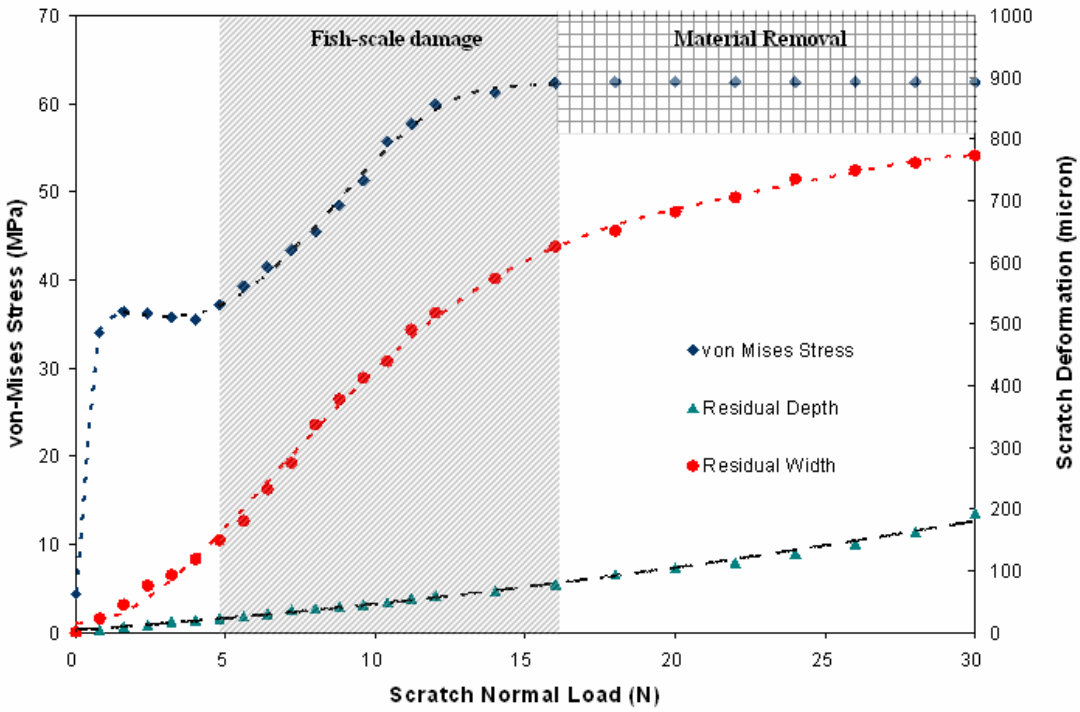

Fig. 7.3. Von-Mises stresses and residual scratch depths and widths as a function of applied normal load.

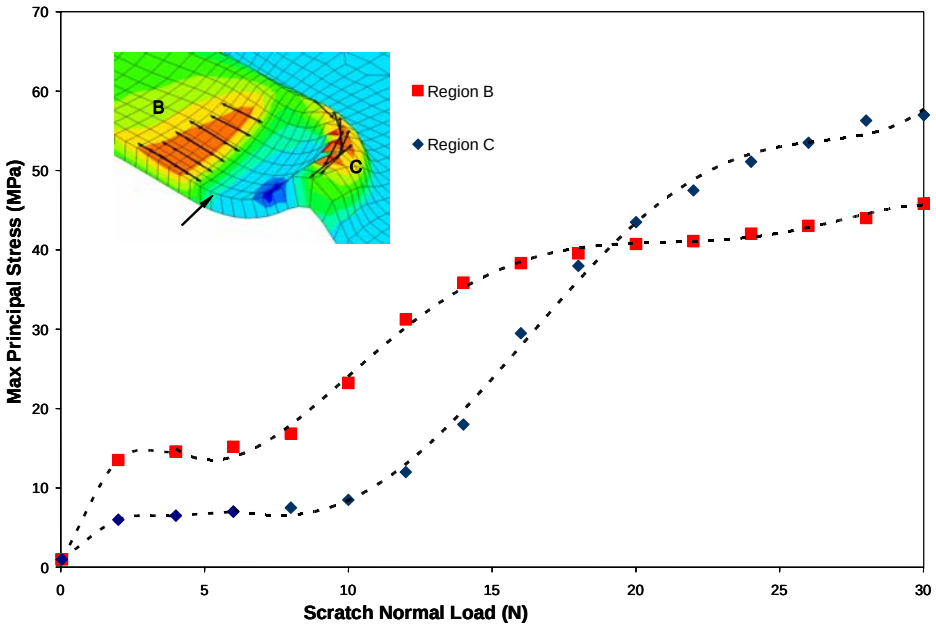

a)

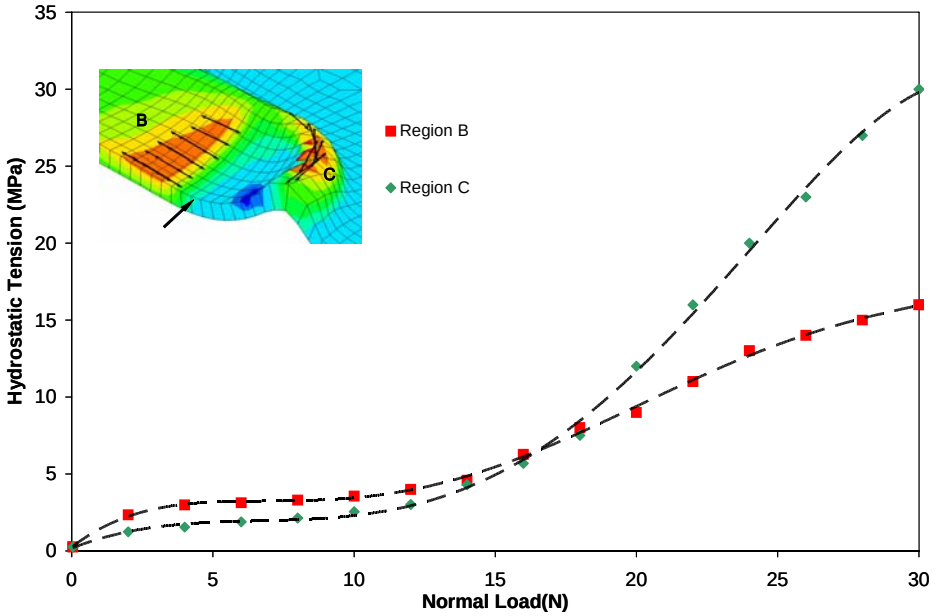

b)

Fig. 7.4. Stress magnitude in regions B and C as a function of applied normal load: a) maximum principal stresses; and b) hydrostatic tension.

For the formation of brittle damage, the evolution of the maximum principal stress in regions B and C were plotted in Fig. 7.4(a). After an early increase of the maximum principal stress magnitude, it is found that the stress magnitude for both regions levels off to a low magnitude of 15 MPa and 6 MPa for regions B and C, respectively. The yielding related damage may dominate in this load range if the material is relatively ductile. The maximum principal stress magnitude then increase for both regions and the rate of increase slows down at a higher normal load range. When a moderate normal load is applied, the maximum principal stress magnitudes in regions B and C increase to such a magnitude that it can no longer be ignored. For brittle and weak polymers, cracking and voiding are favored now. Because of the higher maximum principal stress experienced in region B, the brittle types of damage mechanisms tend to occur there first, which leads to the formation of the parabolic crack zone observed in PC and epoxy. Under a high level of normal load, the maximum principal stress in region C becomes larger than that in region B. Consequently, brittle damage will dominate in region C, which resembles a cutting process.

Hydrostatic tension is known to be responsible for the volume increase within a material, thus is strongly related to the brittle damage mechanisms, such as cracking, crazing, voiding, and interfacial debodning [42]. To assess the probability of the occurrence and location of brittle damage, the hydrostatic tension components in regions B and C were also plotted to address the possible brittle damage during scratch (Fig. 7.4(b)). Similar to the maximum principal stress trends, it is found that the hydrostatic tension levels off to about 3 MPa and 2 MPa in regions B and C, respectively, after an

initial sharp increase. Given the high Von-Mises stress magnitude and the low hydrostatic tension level in the early stage of scratch, ductile yielding is likely to dominate. However, if the polymer is brittle and weak, cracking, crazing, and other types of brittle damage may still take place at low loads. When the applied normal load is further increased, the hydrostatic tension magnitude begins to increase significantly and help facilitate the formation of brittle damage. For the strong polymers, brittle types of damage become more dominant as the applied normal load is further increased. Since the FEM modeling here does not take into account of element separation or removal after damage, it is likely that the material removal will take place at this later stage, which has been experimentally observed (Fig. 3.2).

The competition between ductile deformation and brittle damage always exists throughout the entire scratch process. Depending on the material properties, i.e., ductile vs. brittle and strong vs. weak, and the corresponding stress state and magnitude under the prescribed loading conditions, either ductile deformation or brittle damage will become the dominant damage mechanism. The above factors are responsible for the various damage modes observed during polymer scratch. Extensive research efforts are still needed to understand the scratch behavior of polymers exhibiting different constitutive behaviors.

7.3 Periodic scratch-induced damage features

For all the scratch tests, regardless of the type of damage mode involved, the same damage feature will usually repeat itself until the normal load level is high enough

to trigger the next damage mode. To explain this periodic occurrence of scratch damage, it is necessary to analyze the scratch process in a greater depth.

When the scratch tip ploughs through the material ahead of it, the material will be either pushed forward or piled up sideways [19]. This phenomenon is usually observed for relatively ductile polymers, where ironing and plastic deformation take place readily. In addition to the surface friction between the substrate and the scratch tip, the material accumulated ahead of the tip also introduces resistance against the tip movement [26]. An increased normal load causes deeper tip penetration into the substrate (Fig. 7.5(a)), which causes further increase of frictional force. In turn, the tip will drag the material along with it during scratch (region B in Fig. 7.2). When the induced stress magnitude becomes greater than the onset value for yielding, the fish-scale damage pattern will be formed through plastic drawing of the material (Fig. 7.5(b)). Eventually, the exerted tensile stress will become high enough to cause the next stage of scratch damage – material removal.

The "stick-slip" phenomenon [33-34, 50, 63] occurs when the indenter experiences periodic changes in resistance during the tip movement. The scratch tip is designed to move at a constant speed. However, the actual velocity of the tip movement relative to the material surface oscillates due to the physical nature of surface contact between a non-rigid tip and the substrate, where formation and breakage of a local scale adhesion between tip and material occur repeatedly. When the velocity of the tip relative to the material surface drops, the sticking phenomenon occurs. This phenomenon becomes more significant when the tip penetrates deep in the substrate, which introduces

additional resistance force. The stored strain energy continues to build up due to the increasing applied normal load and the inertia exerted from the fixed testing rate (Fig. 7.5(a)). If the exerted stress on the material is lower than the ultimate strength of the material, the scratch tip will drag the material along (Fig. 7.5(b)) and slip over the ridge of the pile-up region (Fig. 7.5(c)). The tip may lose its full contact with the material surface during the slip process. Because of the decrease in resistance for the tip movement, the tip can push forward in full speed again. By the sheer action of the applied normal load, the scratch tip will soon reestablish its surface contact and begin to compress the material again. The stick stage occurs again until the next slipping action repeats itself.

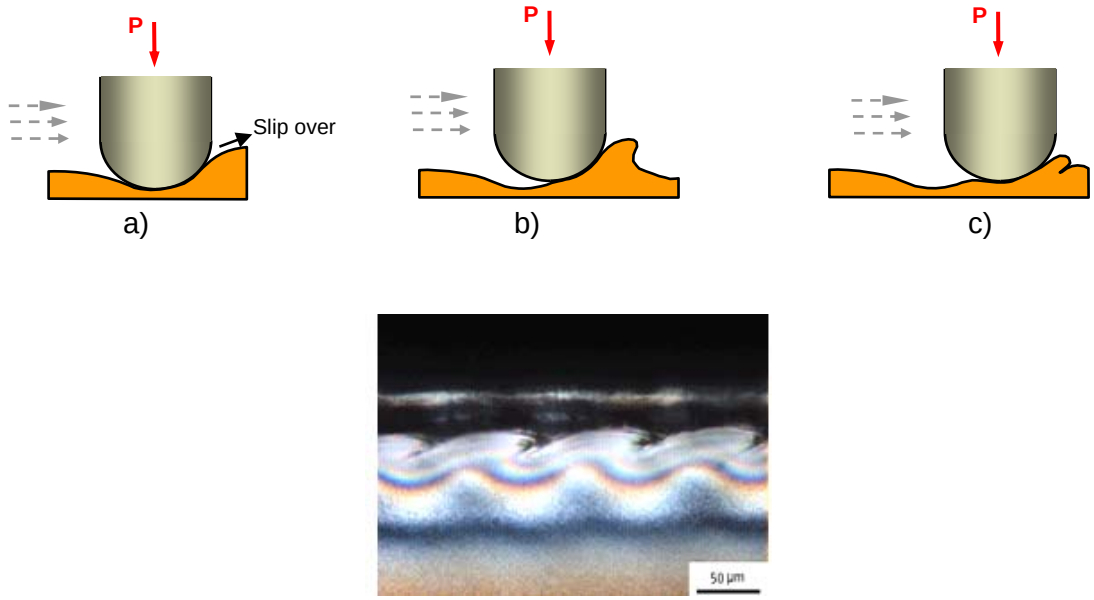

Fig. 7.5. Fish-scale formation mechanisms: a) slipping; b) drawing; c) substrate compression; and d) longitudinal-section of OM of the fish-scale along the scratch path for TPO.

Two possible mechanisms are involved in the stick-slip step. For ductile and weak polymers, the repeated surface contact and substrate compression by the scratch tip after each stick-slip step introduces the observed periodic damage feature. An OM image of a longitudinal section along the scratch path of TPO is shown in Fig. 7.5 d). The repeated fish-scale mechanism can be easily observed. Meanwhile, for brittle and strong polymers, a similar strain energy accumulation during the stick step occurs (Fig. 7.6 a)). Before the indenter loses its full contact with the substrate and slips over as described above, the tensile stress magnitude in the region behind the scratch tip may have already reached its ultimate strength. Then, brittle fracture takes place to release the accumulated strain energy. Afterwards, the resistance decreases. Thus, the tip can slip over and move again (Fig. 7.6 b) and c)). The repeated energy release process by the brittle damage behind the tip leads to the formation of the observed parabolic crack zone. The longitudinal section along the scratch path of the model epoxy clearly shows this type of damage caused by the scratch tip stick-slip phenomenon ((Fig. 7.6 d)).

For the brittle and weak polymers, the fish-scale pattern cannot be well developed because of the easy formation of brittle damage before the slip-over. Instead, numerous micro cracks, crazes, and/or voids are formed. The pseudo fish-scale contains a mixture of micro-cracks, crazes, or voids.

Under a high normal load level, large tensile stress magnitude will induce brittle damage as a dominant damage feature as discussed in the above section. The scratch tip can easily move forward directly through the pile-up, resembling a plowing process. Material removal due to the brittle damage is observed.

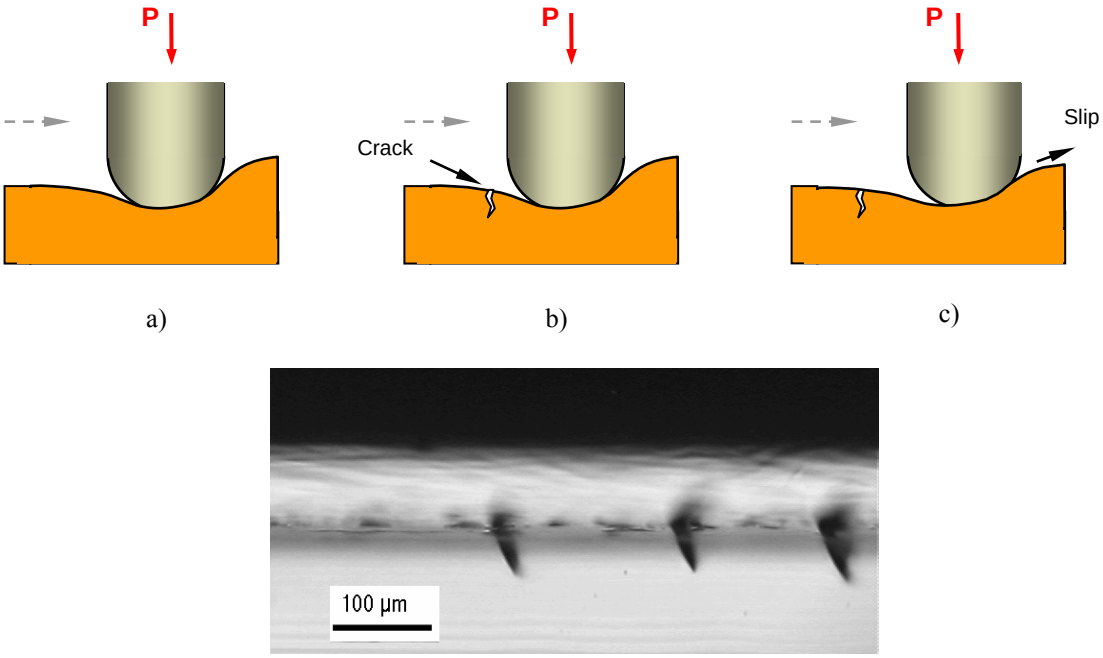

Fig. 7.6. Parabolic crack formation mechanisms: a) stick; b) crack formation; c) slip; and d) longitudinal-section OM of the parabolic crack along the scratch path for epoxy.

It is shown herein that the periodic scratch damage phenomena induced by the stick-slip process is not only related to the adhesive forces between the indenter and the substrate but also to the material type, indenter shape, scratch speed, and applied normal load. At low normal loads, where there is little material accumulation, the stick-slip steps are easily overcome by the inertia of the tip movement and by the low kinetic frictional resistance of the surface. With a larger normal load imposed onto the material, the scratch depth increases and more material builds up around the indenter. Hence, the stick-slip process becomes more dominant and must be accounted for. Research effort on

the mechanics responsible for the observed stick-slip during scratch is now under way and presented in Appendix.

Based on the knowledge gained above, it becomes clear how the material properties, the stress state, and its magnitude are profoundly important to affect the scratch-induced damage mechanisms. It is possible to promote or suppress certain damage mechanisms exerted by scratch. Depending on the scratching load expected and the type of material utilized, one can begin to predict the material properties needed to prevent the formation of undesirable scratch damage mechanisms.

The ASTM/ISO standard linearly increasing normal load scratch test have been performed on four categories of polymers: (I) ductile and strong, (II) ductile and weak, (III) brittle and weak, and (IV) brittle and strong. Various scratch damage modes have been identified. With an aid of finite element modeling, various damage mechanism evolution processes are described. The stick-slip process during polymer scratch is found to be responsible for the observed periodic fish-scale pattern and parabolic crack formations. Relationship among the scratch damage modes and their evolution, material type, testing rate, and applied scratch load has been discussed.

CHAPTER VIII

CONCLUSION AND FUTURE RESEARCH PLAN

8.1 Summary of present scratch research

Both experimental and numerical efforts were carried out to fundamentally study the complicated scratch-induced deformation and damage behaviors of polymeric materials. The research was performed based on five aspects:

1) Experimental scratch work on a wide range of polymers to assess the generic scratch behaviors of polymers,
2) Implementation and validation of FEM modeling for polymer scratch and optimization of computational efficiency,
3) Parametric study on the effect of material and surface properties on polymer scratch behavior,
4) Experimental and numerical study of scratching of polymer coatings,
5) Categorization of polymer scratch damage mechanisms and their evolution processes according to material types and mechanistic responses.

Taking into account important physical and computational considerations of the polymer scratch, FEM modeling is shown to be an adequate tool for describing the mechanistic response of polymer materials during a scratch process. With the introduction of two remeshing algorithms, i.e., the EFM and the MFM methods, the computational efficiency of polymer scratch modeling has been significantly improved.

This allows for a systematic, comprehensive investigation of polymer scratch behavior using numerical approach.

FEM modeling, as well as experimental efforts, has been employed to conduct parametric studies for evaluating the effect of mechanical and surface properties of polymers on scratch performance. It is found that Poisson's ratio has a negligible effect on scratch performance, while increasing the Young's modulus of a material does not necessarily improve its overall scratch performance. On the other hand, modification of the yield strength of a material will have a major impact on scratch resistance as a higher yield stress reduces the residual scratch depth and delay the formation of fish-scales. Reducing the friction coefficient, either by altering the surface roughness or by introduction of slip agent, can significantly improve scratch resistance.

The scratch behaviors of polymeric coatings on soft and hard substrates were also investigated. Depending on different combinations of polymeric coatings and substrates utilized, various damage modes can occur, including coating delamination, transverse cracking and buckling failure. A soft coating on a hard substrate will give rise to an entirely different scratch damage pattern from those of a hard coating on a soft substrate. The numerical analysis provides mechanistic insights for the observed polymer coating deformation mechanisms and failure modes. Usefulness of the scratch method and finite element modeling to evaluate polymer coating scratch behavior is also discussed.

With an aid of the numerical findings, fundamental knowledge about the damage mechanism evolution during scratch is gained. Plastic yielding and brittle damage, the

two important modes of polymer damage, induced during scratch were carefully investigated and correlated with FEM findings. It is found that the occurrence of these two modes of damage depends on the material properties, the surface characteristics, and the imposed stress state and magnitude under the scratch tip. The scratch damage modes and evolution process with respect to the normal load level is described and discussed for different material types. A generic scratch damage evolution map is constructed. Relationships among the material type, testing rate, and applied scratching load on the scratch damage modes and their evolution have been discussed.

In summary, this dissertation has helped us gain fundamental knowledge on the underlying mechanics responsible for the occurrence of various scratch-induced damage features. It has also contributed to the fundamental understanding of coating scratch behavior. It has further provided evaluation and design tools for the polymers industry to accelerate its production of scratch resistant polymers and coatings.

8.2 New scratch research directions

The study of polymer scratch behavior is a relatively new research field for both the industry and the academia. Opportunities are still abundant. Three important future research directions are recommended as follows.

8.2.1 Development of a material constitutive law

The first future research area to focus on is to implement an appropriate material constitutive law for polymer scratch numerical analysis so that the accurate mechanical

response under complex deformation can be captured [77-85]. The key emphasis will be to establish the relationship between material science and mechanics during scratch.

As presented in Appendix A, the current research accomplishments on modeling the scratch behavior of amorphous polymers allows for a better understanding of how mechanical properties affect scratch behavior. Although promising results have shown capability to describe the occurrence of plastic deformation and crazing for amorphous polymeric materials, more work is still needed to confirm if the same can be applied to semi-crystalline polymers and composites. A comprehensive material-dependent damage criterion is also needed to allow for the prediction of occurrence of the two important polymer damage modes, i.e., shear yielding and crazing/cracking, during scratch.

A comprehensive experimental work is also necessary to provide essential parameters for developing the constitutive models that can accurately represent the polymer scratch response and correctly characterize the type and extent of material damage. Experimental efforts are also important for validating the numerical analysis results. Once the constitutive models and damage criterion have been constructed successfully, they can be implemented into in the numerical analysis procedure. By establishing a correlation between experimental observation and numerical simulation, the research can provide a more accurate understanding of polymer scratch behavior. Some preliminary study based on semi-crystalline polymers is presented in Appendix 2.

8.2.2 Mechanical modeling of the stick-slip process

As presented in Chapter VII, the periodic occurrence of scratch damage regardless of the type of polymer is the result of the stick-slip phenomenon when the

indenter experiences periodic changes in resistance during its movement [33-34, 50, 63]. It is necessary to analyze this process in a greater depth.

The phenomenological cause for stick-slip is the existence of a horizontal degree of freedom and the effects of the physical difference between static friction and kinetic friction. Meanwhile, the vertical degree of freedom plays an important role, especially when the effective stiffness of the system is involved, which can be manifested as the difference between a dead-load test method and a load-controlled test method. For the scratch process, in addition to the oscillation from the static friction to sliding friction, the material accumulated ahead of the tip also introduces resistance against the scratch tip movement. The deeper the tip penetrates into the surface, the higher the material resistance becomes. Another important factor here is the geometric shape and size of the scratch tip, which has a significant effect on resistance force and the resulting scratch damage mode. New mechanical modeling efforts of the stick-slip process attempting to address the above issues are presented in Appendix 2. Once the stick-slip phenomenon can be reasonably explained, it can provide fundamental understanding of the scratch behavior under various scratch conditions.

8.2.3 Automated evaluation of scratch visibility

In addition to the complex damage mechanisms, the scratch-induced visibility due to surface deformation and/or damage of polymeric materials represents a critical technological problem since the aesthetic consideration becomes one of the primary concerns for many durable goods applications, such as automobile instrument panels and appliance housings. Traditional visual surveys of scratch performance are based on a

combination of numerous complex visual clues and prior experience with little understanding of the optical processes involved. Because of the complex nature of human perception of “visibility”, many factors, including environment light condition, the lighting angle, and distance from sample to inspectors’ eye, just to name a few, can significantly bias the determination of scratch-induced visibility [86-88]. Some researchers have proposed a so-called “brightness-threshold” method to obtain the information of onset scratch visibility [20]. While this method is effective for smooth, moderately low-gloss substrates, it is not applicable for high-gloss, textured surfaces, or colored samples.

Quantitative evaluation of scratch visibility resistance of a polymer can be challenging, and is perceived as a subjective matter. To consistently and reliably obtain scratch resistance of polymer samples regardless of sample surface texture characteristics, a method that utilizes relevant optical parameters based on human physiology to alleviate biases arising from human observers and environment is needed [89]. The preliminary effort on the scratch visibility determination methodology is presented in Appendix 3.

REFERENCES

[1] ASTM International, ASTM D7027-05, Annual Book of ASTM Standards (2005), ASTM International, West Conshohocken, PA, USA.

[2] International Organization for Standardization, ISO 19252(2008), International Organization for Standardization, Geneva, Switzerland.

[3] B.J. Briscoe, P.D. Evans, S.K. Biswas and S.K. Sinha, Polym. Eng. Sci. 36(1996), p.2996.

[4] Y.N. Liang, S.Z. Li, D.F. Li, and S. Li, Wear 199(1996), p.66.

[5] B.J. Briscoe, P.D. Evans, E. Pelillo, and S.K. Sinha, Wear 200(1996), p.137.

[6] K. Hiromi, M. Maki, K Tsunetoshi. and K. Takashi, ANTEC 2004-Annual Technical Conference Proceedings 2 (2004), p.1938.

[7] G.M. Hamilton and L.E. Goodman, J. Appl. Mech. 33(1966), p.371.

[8] J.A. Williams, Tribol. Int. 29(1996), p.675.

[9] O. Vingsbo and S. Hogmark, Wear 100(1984), p.489.

[10] C. Gauthier, S. Lafaye and R. Schirrer, Tribol. Int. 34(2001), p.469.

[11] J. L. Bucaille and E. Felder, Philos. Mag. A 82(2002), p.2003.

[12] C. Xiang, H.-J. Sue, J. Chu and B. Coleman, J. Polym. Sci. B 39(2001), p.47.

[13] J. Chu, C. Xiang, H.-J. Sue and H. R. Damon, Polym. Eng. Sci. 40(2000), p.944.

[14] C. Xiang, H.-J. Sue, J. Chu and K. Masuda, Polym. Eng. Sci. 41(2001), p.23.

[15] M. Wong, G.T. Lim, A. Moyse, J.N. Reddy and H.-J. Sue, Wear 256(2004), p.1214.

[16] M. Wong, A. Moyse, F. Lee, and H.-J. Sue, J. of Mat. Sci. 39 (2004), p.3293.

[17] G.T. Lim, J.N. Reddy and H.-J. Sue, Stimuli-Responsive Polymeric Films and Coatings, Chap. 10(2005), Ed. by M. Urban, American Chemical Society, Washington, DC, USA.

[18] G.T. Lim, M. Wong, J.N. Reddy and H.-J. Sue, J. Coat. Tech. Res. 2(2005), p.361.

[19] G.T. Lim, Ph.D. Dissertation, Texas A&M University, College Station, TX, 2005.

[20] R. Browning, G. T. Lim, A. Moyse, L. Sun and H.-J. Sue, Polym. Eng. Sci. 46(2006), p.601.

[21] E. Moghbellia, R. Browning, W.-J. Boo, S.F. Hahn, L.J.E. Feick and H.-J. Sue, Tribol. Int. 41(2008), p.425.

[22] E. Moghbelli, L. Sun, H. Jiang, W. J. Boo and H.-J. Sue, Polym. Eng. Sci. 49(2009), p.483.

[23] R. L. Browning, H. Jiang and H.-J. Sue, Tribology of Polymeric Nanocomposites 1st ed, Chapt. III (2008), Elsevier, Amsterdam, Netherland.

[24] R. Browning, H. Jiang, A. Moyse and H.-J. Sue, Y. Iseki, K. Ohtani, Y. Ijichi, J. Mat. Sci. 43(2008), p.1357.

[25] R. Browning, G.T. Lim, A. Moyse, H.-J. Sue, H. Chen, J.D. Earls, Surf. Coat. Tech. 201 (2006), p.2970.

[26] H. Jiang, R. Browning, A. Moyse and H.-J. Sue, Appl. Surf. Sci. 254(2008), p.4494.

[27] H. Jiang, G.T. Lim, J.D. Whitcomb and H.-J. Sue, J. Polym. Sci. B 45(2007), p.1435.

[28] H. Jiang, R. Browning, J.D. Whitcomb, M. Ito, M. Shimouse, T.A. Chang and H.-J. Sue, Tribol. Let.(under review)

[29] H. Jiang, R. Browning, E. Moghbelli, Y. Song and H.-J. Sue, Polym.(under review)

[30] Callister W. D., Material Science and Engineering, 6th ed.(2004), John Wiley & Sons, Inc., New York, USA.

[31] S.J. Bull, Tribol. Int. 30 (1997), p.491.

[32] S. Ducret, C. Pailler, V. Jardret, R. Vargiolu and H. Zahouani, Wear 255 (2003), p.1093.

[33] K. Li, B.Y. Ni and J.C.M. Li, J. Mat. Res. 11(1996), p.1574.

[34] K. Li, Y. Shapiro and J.C.M. Li, Act. Mat. 46(1998), p.5569.

[35] K. Holmberg, H. Ronkainen, A. Laukkanen, K. Wallin, E. Ali and E. Osman, Wear 264 (2008), p.877.

[36] K. Holmberg, A. Laukkanen, H. Ronkainen, K. Wallin, S. Varjus and J. Koskinen, Wear 254 (2003), p.278.

[37] K. Holmberg, A. Laukkanen, H. Ronkainen, K. Wallin, S. Varjus and J. Koskinen, Surf. Coat. Tech. 200 (2006), p.3793.

[38] H. Pelletier, C. Gauthier and R. Schirrer, Tribol. Let. 32 (2008), p.109.

[39] V. Jardret and P. Morel, Prog. Org. Coat. 48 (2003), p.322.

[40] H.-X. Tang and D.C. Martin, J. Mat. Sci. 38 (2003), p.803.

[41] A.J. Kinloch and R.J. Young, Fracture Behavior of Polymers(1983), Elsevier Co., New York, USA.

[42] A.G. Atkins and Y-W. Mai, Elastic and Plastic Fracture – Metals, Polymers,

Ceramics, Composites, Biological Materials (1985), Ellis Horwood Ltd., Chichester, UK.

[43] C.B. Bucknall, Polym. 48 (2007), p.1030.

[44] L. Anand and N.M. Ames, Int. J. Plast. 22 (2006), p.1123.

[45] L. Anand and M.E. Gurtin, Int. J. Solids.Struct. 40(2003), p.1465.

[46] B. P. Gearing, Ph.D. Dissertation, Massachusetts Institute of Technology, Cambridge, MA, USA, 2002.

[47] ABAQUS®, Inc., ABAQUS® Analysis User's Manual V. 6.4(2003), Pawtucket, Rhode Island, USA.

[48] B. R. Lawn, S. M. Wiederhorn and D. E. Roberts, J. Mat. Sci. 19(1984), p.2561.

[49] S. Ramasamy, J. Mark, H. Kiyoshi and W. Kanemastsu, J. Euro. Ceram. Soci. 26(2006), p.351.

[50] R. Smith, D. Mulliah, S.D. Kenny, E. McGee, A. Richter and M. Gruner, Wear 2005 (259), p.459.

[51] A.M. Hodge and T.G. Nieh, Intermetal. 12(2004), p.741.

[52] J.S.S. Wong, H.-J. Sue, K.-Y. Zeng, R.K.Y. Li and Y.-W. Mai, Act. Mat. 52(2004), p.431.

[53] W. Brostow, A. Hinze and R. Simoes, J. Mat. Res. 19 (2004), p. 851.

[54] H. Pelletier, C. Gauthier and R. Schirrer, J. Eng. Tribol., 2008(222), p.221.

[55] Super Computer Center, Cosmos User's Manual (2003), Texas A&M University, College Station, Texas, USA.

[56] L. G. Moreau, H. Borouchaki and A. Cherouat, 10th ESAFORM Conference on

Material Forming, Zaragoza, Spain, 2007.

[57] A. Tradegard, F. Nilsson and S. Ostlund, Comput. Meth. Appl. Mech. Eng. 160(1998), p.115.

[58] H. Borouchaki, P. Laug, A. Cherouat and K. Saanouni, Int. J. Num. Meth. Eng. 63(2005), p.1.

[59] T. A. Maxian, T. D. Brown, D.R. Pedersen and J. J. Callaghan, ASME International Mechanical Engineering Congress and Exposition, San Francisco, USA,1995.

[60] T.C. Ovaert and B.R. Kim, Proceedings of the World Tribology Congress III (2005), Washington, DC , USA. p.405.

[61] C. Gauthier, A.-L. Durier, C. Fond and R. Schirrer, Tribol. Int. 39 (2006), p.88.

[62] J. Li, and W. Beres, Wear 260 (2006), p.1232.

[63] S.L. Zhang and J.C.M. Li, Mat. Sci. Eng.: A 344(2003), p.182.

[64] H.-J. Sue and A.F. Yee, Polym. 29(1988), p.1619.

[65] G. Dhondt, The Finite Element Method for Three-dimensional Thermomechanical Applications (2004), John Wiley and Sons, West Sussex, England.

[66] G. Allaire and S. M. Kaber, Numerical Linear Algebra (2007), Springer, New York, USA.

[67] E. W. Cheney and D. R. Kincaid, Numerical Mathematics and Computing, 6th ed.(2007), Brooks Cole, New York, USA.

[68] G. H. Golub, C. F. V. Loan, Matrix Computations, 3rd ed.(1996), The Johns Hopkins University Press, Baltimore, MD, USA .

[69] R.S. Hadal and R.D.K. Misra, Mat. Sci. Eng.: A 398(2005), p.252.

[70] S.J. Bull and E.G. Berasetegui, Tribol. Int. 39 (2006), p.99.

[71] J. Malzbender, and G. With, Surf. Coat. Tech. 135 (2001), p.202.

[72] H. Ronkainen, A. Laukkanen and K. Holmberg, Wear 263 (2007), p.1315.

[73] S. Oliveira and A. F. Bower, Wear 198 (1996), p.15.

[74] D. Diao and A. Kandori, Tribol. Int. 39 (2006), p.849.

[75] P. B. Lambotte, J.L. Loubet, C. Verpy and P. Pavan, Thin Solid Films 420/421 (2002), p.281.

[76] I. Demirci, C. Gauthier and R. Schirrer, Thin Solid Films 479(2005), p.207.

[77] B.J. Briscoe, A. Delfino and E. Pelillo, Wear, 225-229(1999), p.319.

[78] R.S. Kody, and D.C. Martin, Polym. Eng. Sci. 36(1996), p.298.

[79] M.H. Blees, G.B. Winkelman, A.R. Balkenende and J.M.J. Toonder, Thin Solid Films, 359(2000), p.1.

[80] R.S. Hadal and R.D.K. Misra, , Mat. Sci. Eng. A 398(2005), p.252.

[81] J.S. Bergstrom, S.M. Kurtza, C.M. Rimnac and A.A. Edidin, Biomat. 23 (2002), p. 2329.

[82] E.M. Arruda, S. Azhi, Y. Li and A. Ganesan, J. Eng. Mat. Tech. 119(1997), p.216.

[83] T. Yamamoto and H. Furukawa, Polym. 36(1995), p.2393.

[84] M. C. Boyce, D. M. Parks and A. S. Argon, Mech. Mat. 7(1998), p.15.

[85] E. M. Arruda and M. C. Boyce, Int. J. Plast. 9(1993), p.697.

[86] A. Michelson, Studies in Optics(1927), U. of Chicago Press, Chicago, USA.

[87] W.H. Buchsbaum, Color TV Servicing, 3rd ed. (1975), Prentice Hall, New York,

USA.

[88] M. Roberts, Biology: A Functional Approach, 4th ed.(1986), Nelson Thornes, New York, USA.

[89] H. Jiang and H.J. Sue, ASV© User's Manual V.1.0 (2008), College Station, Texas, USA.

APPENDIX A

This appendix contains the brief discussion of constitutive model of amorphous polymers. Amorphous glassy polymers, such as Poly(methyl methacrylate) (PMMA) and polycarbonate (PC), are chosen as the model materials. With the introduction of a representative material constitutive law, the implementation of a set of damage criteria of polymer material, a descriptive analysis model will be constructed as a powerful quantitative tool to study polymer scratch behavior and other possible applications.

A.1 Representative material constitutive law

The first research objective is to identify a more representative polymer material constitutive law so that a more accurate mechanical response of the polymer under the complex stress/strain stress condition can be described. This is an essential effort to bridge the gap between material science and mechanics in scratch research. So far, preliminary effort has already been initiated to model amorphous glassy polymers, such as PMMA, following the research works described in [79-81].

The shear-yielding of amorphous polymers is modeled following the Boyce theory [79]. Using an internal-state variable that represents the local free-volume, the highly non-linear stress–strain behavior that precedes the yield-peak and post-yield strain softening can be captured. Our preliminary work shows that the stress-strain behavior of numerical simulation fits well with the result of the uniaxial compression

test for PMMA [79]. The representative constitutive model was implemented in ABAQUS using user defined material type (VUMAT) which is given in A1.4.

However, the relevance of this constitutive relationship for tensile, shear, plane strain compression and other more complex modes of deformation need to be further examined. Once those validations are established, it will become certain that this model can be applied correctly to amorphous polymers. Concurrently, the necessary experiments will be performed to provide material parameters for constructing the material constitutive relationship of model polymer material.

A.2 Damage criterion

The constitutive relationship must allow the two important damage modes, i.e., shear yielding and crazing/cracking, to compete against each other before ultimate failure. Anand's model shows the possibility to introduce a continuum constitutive relationship containing crazing initiation, thickening, and breakdown [79-81]. Once the crazing criterion is reached, the transition from shear-flow to craze-flow occurs by the changing in damage flow rules. Although the local maximum principal tensile stress was adopted by Anand's work as the crazing initiation criterion, other possible crazing criterions such as the local maximum principal strain, the local maximum hydrostatic stress, the local maximum hydrostatic strain and the criterion based linear elastic fracture mechanics appear to have more physic meaning and need to be examined.

After the careful validation, a set of damage criteria (yield vs. crazing) then can be implemented in ABAQUS. The user defined material subroutine will check the stress

state against these damage initiation criteria and determine the type of damage mode and the corresponding damage evolution following the respective flow rule. For the material losing its load-carrying capability, the subroutine will monitor the damage evolution and decide the magnitude of degradation of the material. At a critical stage where the ultimate failure has been reached, a total loss of stiffness in the material will be assigned to the portion of the meshes involved.

With a well-controlled scratch test, the transitions in material damage behavior can be well examined under various loading conditions. This allows us to affirm the validity of the numerical modeling and establish a reasonable quantitative correlation with experimental findings.

A.3 Construction of descriptive analysis model

With an appropriately established constitutive model and damage criterion, using the new simulation strategy mentioned above, the analysis for polymer scratch can be performed more efficiently and accurately. Validating the numerical simulation results by scratch experimental findings, the physics-based mechanical analysis model can be constructed and the fundamental knowledge of polymer scratch can be obtained. The quantitative prediction power shall be utilized for performing further investigation to help researchers to understand the mechanics mechanisms behind the complicate polymer damage modes and its relationship with material properties. It can also be used to identify the key scratch parameters and their influence on scratch performance of

polymers which provide important guidelines for the design of material with good scratch resistance.

After above proposed research approaches are accomplished with reasonable success, its collective impact on the academic and industrial research on polymer material will be significant. It can provide a comprehensive and versatile analysis tool allowing not only for fundamental understanding of polymers scratch behavior but also for various fields of applications, e.g., study of surface deformation and damage, micro/nano-indentation.

A.4 FORTRAN code of implementing Anand's model

This part contains the FORTRAN program that implement the Anand's constitutive model of amorphous polymer.

```
Subroutine vumat(
C Read only -
     1  nblock, ndir, nshr, nstatev, nfieldv, nprops, lanneal,
     2  stepTime, totalTime, dt, cmname, coordMp, charLength,
     3  props, density, strainInc, relSpinInc,
     4  tempOld, stretchOld, defgradOld, fieldOld,
     3  stressOld, stateOld, enerInternOld, enerInelasOld,
     6  tempNew, stretchNew, defgradNew, fieldNew,
C Write only -
     5  stressNew, stateNew, enerInternNew, enerInelasNew )
       include 'vaba_param.inc'
C
C    MODEL FOR THE SHEAR DEFORMATION AND CRACK OF POLYMERS
C    SHEAR MODEL: SPRING+BURGERS ELEMENT+PLASTIC ELEMENT
C    CRACK MODEL: S11>S11_CR WHEN SKK>0
C
C
C
C All arrays dimensioned by (*) are not used in this algorithm
```

```
  dimension props(nprops), density(nblock),
     1  coordMp(nblock,*),
     2  charLength(*), strainInc(nblock,ndir+nshr),
     3  relSpinInc(*), tempOld(*),
     4  stretchOld(*), defgradOld(nblock,ndir+nshr),
     5  fieldOld(*), stressOld(nblock,ndir+nshr),
     6  stateOld(nblock,nstatev), enerInternOld(nblock),
     7  enerInelasOld(nblock), tempNew(*),
     8  stretchNew(*), defgradNew(nblock,ndir+nshr), fieldNew(*),
     9  stressNew(nblock,ndir+nshr), stateNew(nblock,nstatev),
     1  enerInternNew(nblock), enerInelasNew(nblock)
C      strain components stored as state variables
       dimension eelas(ndir+nshr),eplas(ndir+nshr),deplas(ndir+nshr)
       dimension evisco(ndir+nshr),devisco(ndir+nshr),veint(ndir+nshr)
       dimension effstrn(ndir+nshr),ps(ndir),an(ndir,ndir),s(ndir+nshr)
        dimension dr(3,3),f_old(6),f_new(6)

         data newton,toler/10,1.0E-6/
         character*80 cmname

       parameter( zero = 0., one = 1., two = 2., three = 3.,
     1  third = one/three, half = .5, twoThirds = two/three,
     2  threeHalfs = 1.5 )

C -------------------------------------------------------------
C     PROPS(1) - E
C     PROPS(2) - NU
C     PROPS(3) - E1
C     PROPS(4) - ETA1
C     PROPS(5) - ETA0
C     PROPS(6) - PHAI
C     PROPS(7) - PHAI2   FOR NON-ASSOCIATIVE FLOW
C     PROPS(8) - B       FOR EYRING MODEL
C     PROPS(9) - C1
C     PROPS(10)- C2
C     PROPS(11)- M
C     PROPS(12)- SCRAZE
C     PROPS(13)- ZETA0
C     PROPS(14)- CRAZE STRAIN LIMIT
C     PROPS(15)- SHEAR STRAIN LIMIT
C     PROPS(16)- Y0
C     PROPS(17)... PLASTIC CURVE
C     CALLS AHARD FOR CURVE OF SYIELD VS. PEEQ
C -------------------------------------------------------------
C
      if (ndir .NE. 3) then
```

```
        write(6,1)
  1      format(//,30X,'***ERROR - THIS VUMAT MAY ONLY BE USED FOR ',
     1         'ELEMENTS WITH THREE DIRECT STRESS COMPONENTS')
      endif
C
C     ELASTIC PROPERTIES
      ntens=ndir+nshr

      bniu=props(2)
      if(bniu.GT.0.4999.AND.bniu.LT.0.5001) bniu=0.499

C PARAMETERS FOR THE KELVIN UNIT

      phai=props(6)
        phai2=props(7)
        B=props(8)
        c1=props(9)
        c2=props(10)
        c3=three*bniu/(one+bniu)
        bm=props(11)
        scraze=props(12)
        zeta0=props(13)
        craze_cr=props(14)
        shear_cr=props(15)
c     loop the material block
do 350 i = 1,nblock
        c_factor=stateOld(i,4*ntens+4)
        if(c_factor .EQ. 0)  c_factor=1.0
      q_factor=c_factor

        e0=props(1)
        e1=props(3)
        eta1=props(4)
        eta0=props(5)

      e0=e0*q_factor
      bk=e0/(one-two*bniu)/three
      g=e0/(one+bniu)/two
        e1=e1*q_factor
        g1=e1/(2.0*(1.0+bniu))
        eta1=eta1*q_factor
        eta0=eta0*q_factor
        coef1=1.0+eta1/eta0+1.0/4.0*g1/eta0*dt
      coef2=g1+2.0*eta1/dt
        coef3=1.0/4.0*g1/eta0*dt
        coef=1.0+g*coef1/coef2
C     RECOVER AND ROTATE DEVIATORIC SHEAR STRAIN & TOTAL STRESS
```

```
 c      CALL ROTSIG(STATEV(1),DROT,EELAS,2,NDI,NSHR)
c      CALL ROTSIG(STATEV(NTENS+1),DROT,EPLAS,2,NDI,NSHR)
c      CALL ROTSIG(STATEV(2*NTENS+3),DROT,EVISCO,2,NDI,NSHR)
      do 10 j=1,ntens
         eelas(j)=stateOld(i,j)
         eplas(j)=stateOld(i,j+ntens)
         evisco(j)=stateOld(i,j+3+2*ntens)
         veint(j)=stateOld(i,j+3+3*ntens)
         deplas(j)=0.0
         f_old(j)=defgradOld(i,j)
         f_new(j)=defgradNew(i,j)
10       continue
c     get rotation tensor and rotate old strain tensor
      call getdr(f_old,f_new,dr)
      call ROTTENSOR(eelas,dr,3,3)
      call ROTTENSOR(eplas,dr,3,3)
       call ROTTENSOR(evisco,dr,3,3)
      eqplas_shr=stateOld(i,1+2*ntens)
       eqplas_crz=stateOld(i,2+2*ntens)
           vplas=stateOld(i,3+2*ntens)

C     CALCULATE DEVIATORIC STRESS
      oldstresskk=0.0
       dstrankk=0.0
       strankk=0.0
        do 20 j=1,ndir
          oldstresskk=oldstresskk+stressOld(i,j)
          dstrankk=dstrankk+strainInc(i,j)
        strankk=strankk+eelas(j)+eplas(j)+evisco(j)+strainInc(i,j)
20       continue
C     CALCULATE EFFECTIVE STRAIN
      do 30 j=1,ndir
         effstrn(j)=eelas(j)+(strainInc(i,j)-dstrankk/3.0)-
     1       (0.5*(coef1+2.0*coef3)*(stressOld(i,j)-oldstresskk/3.0)+
     1           g1/eta0*veint(j)-2.0*g1*evisco(j))/coef2
30       continue
      do 31 j=ndir+1,ntens
         effstrn(j)=eelas(j)+strainInc(i,j)/2.0-
     1             (0.5*(coef1+2.0*coef3)*stressOld(i,j)+
     1             g1/eta0*veint(j)-2.0*g1*evisco(j))/coef2
31       continue
C     UPDATED DEVIATORIC STRESS
      do 40 j=1,ntens
         stressNew(i,j)=2.0*g/coef*effstrn(j)
40    continue
C     CALCULATE BULK STRESS & PRESSURE
```

```
      stresskk=oldstresskk+3.0*bk*dstrankk
       p=-stresskk/3.0
C    UPDATE DIRECT STRESS
     do 45 j=1,ndir
       stressNew(i,j)=stressNew(i,j)-p
45       continue
C    DETERMINE SHEAR YILED OR CRAZE YIELD
     do 50 j=1,ntens
        s(j)=stressNew(i,j)
50       continue
C    PRINCIPAL STRESS AND
     call PRINCIPAL(s,ps,an,ndir,nshr,1.0E-6)
       ps1=ps(1)
       nmax=1
       if(ps(2) .GT. ps1) then
         ps1=ps(2)
         nmax=2
       endif
       if(ps(3) .GT. ps1) then
         ps1=ps(3)
         nmax=3
       endif
       bms=-p
       cs=c1+c2/bms+c3*bms
       if (bms .GT. 0 .AND. ps1 .GT. 0 .AND. ps1 .GT. cs) then
          flow=one
       else
          flow=zero
       endif
C    CRAZE FLOW,calculate deplas
     if (flow .EQ. one .AND. c_factor .GT. 1.0E-4) then
         do 60 j=1,ndir
            deplas(j)=zeta0*(ps1/scraze/q_factor)**(1.0/bm)*dt*
    1                  an(j,nmax)**2
60          continue
        do 61 j=ndir+1,ntens
            n1=j-ndir
            n2=j-ndir+1
            if(n2 .GT. ndir) then
                  n2=n2-ndir
              endif
            deplas(j)=zeta0*(ps1/scraze/q_factor)**(1.0/bm)*dt*
    1                  an(n1,nmax)*an(n2,nmax)
61        continue
     eqplas_crz=eqplas_crz+zeta0*(ps1/scraze/q_factor)**(1.0/bm)*dt
       if(eqplas_crz .GT. craze_cr .AND. c_factor .GT. zero) then
       c_factor=c_factor*0.1*craze_cr/eqplas_crz
       endif
```

```
 c     update stress

         dvplaskk=deplas(1)+deplas(2)+deplas(3)
         vplas=vplas+dvplaskk
         stresskk=oldstresskk+3.0*bk/q_factor*c_factor*
       1           (dstrankk-dvplaskk)
          do 70 j=1,ndir
            deplas(j)=deplas(j)-dvplaskk/3.0
          stressNew(i,j)=2.0*g/q_factor*c_factor*
       1                    (effstrn(j)-deplas(j))/coef
          stressNew(i,j)=stressNew(i,j)+stresskk/3.0
70       continue
         do 71 j=ndir+1,ntens
            stressNew(i,j)=2.0*g/q_factor*c_factor*
       1                    (effstrn(j)-deplas(j))/coef
71       continue
        endif

C     SHEAR YIELD FLOW,CALCULATE DEPLAS
c     test crack-->shear yielding
c     if crack and shear yielding can not coexist,delete the following the command
c       flow=zero
      if(nprops.GT.15 .AND. props(16).GT. 0.0 .AND. flow .EQ. zero) then
C
C       MISES STRESS
C
        smises=(s(1)-s(2))*(s(1)-s(2)) +
     1         (s(2)-s(3))*(s(2)-s(3)) +
     1         (s(3)-s(1))*(s(3)-s(1))
   do 90 j=ndir+1,ntens
            smises=smises+6.0*s(j)*s(j)
90       CONTINUE
        smises=sqrt(smises/2.0)
C       SHEAR STRAIN RATE
        effrate=0.0
          do 95 j=1,ndir
            effrate=effrate+(strainInc(i,j)-dstrankk/3.0)*
     1                  (strainInc(i,j)-dstrankk/3.0)
95          continue
        do 100 j=ndir+1,ntens
            effrate=effrate+2.0*strainInc(i,j)*strainInc(i,j)
100           CONTINUE
         effrate=sqrt(effrate/2.0)/dt
         if (effrate .LT. 1.0E-6) then
           effrate=1.0E-6
         endif
C       HARDENING CURVE, GET YIELD STRESS
```

```
C      CALCULATE HOW MANY POINTS FOR THE PLASTIC CURVE
C       COEF5  DEPQ=COEF5*LAMTA
        coef5=sqrt(1.0+phai2*phai2/2.0)
       NVALUE=nprops/2-7
       CALL AHARD(syiel0,HARD,eqplas_shr*coef5,props(16),NVALUE)
C      DETERMINE IF ACTIVELY YIELDING
C
C
      effyield=syiel0+B*log10(effrate)+phai*p
       if (smises .GT. (1+toler)*effyield ) then
C      CALCULATE EQUIVALENT STRAIN
       equie=0.0
       do 110 j=1,ndir
         equie=equie+effstrn(j)*effstrn(j)
110          continue
       do 111 j=ndir+1,ntens
         equie=equie+2*effstrn(j)*effstrn(j)
111          continue
       equie=sqrt(2.0/3.0*equie)
C
C
C      SOLVE FOR EQUIV STRESS, NEWTON ITERATION
C      Maybe unnecessary for explicit solver
        syield=syiel0
        deqpl=0.0
        do 130 j=1,newton
          rhs=3.0*g*(equie-deqpl)-coef*(syield+B*log10(effrate)
     1             -phai*bk*(strankk-vplas-phai2*deqpl))
          deqpl=deqpl+rhs/(3.0*g+coef*(HARD*coef5+bk*phai*phai2))
      call AHARD(syield,HARD,(eqplas_shr+deqpl)*coef5,props(16),NVALUE)
        if(abs(rhs).LT.toler*effyield) goto 140
130      continue
          write(6,2) newton
2        format(//,30X,'***WARNING - PLASTICITY ALGORITHM DID NOT ',
    1       'CONVERGE AFTER ',I3,' ITERATIONS')
140      continue

        stresskk=3.0*bk*(strankk-vplas-phai2*deqpl)
            p=-stresskk/3.0
         effyield=syield+phai*p+B*log10(effrate)
            coef4=3.0*g*deqpl/effyield+coef
        do 150 j=1,ndir
          stressNew(i,j)=2.0*g*effstrn(j)/coef4
          deplas(j)=3.0*stressNew(i,j)*deqpl/(2.0*effyield)
          stressNew(i,j)=stressNew(i,j)+stresskk/3.0
150      continue
```

```
          do 160 j=ndir+1,ntens
           stressNew(i,j)=2.0*g*effstrn(j)/coef4
           deplas(j)=3.0*stressNew(i,j)*deqpl/(2.0*effyield)
160       continue
         eqplas_shr=eqplas_shr+deqpl
           vplas=vplas+phai2*deqpl
              if(eqplas_shr .GT. shear_cr .AND. c_factor .GT. zero) then
           c_factor=c_factor*0.1*shear_cr/eqplas_shr
           endif
        endif
        endif
C
C UPDATE STATE VARIABLES
C CALCULATE DEVISCO
C
      do 260 j=1,ndir
         devisco(j)=(0.5*coef1*(stressOld(i,j)-oldstresskk/3.0+
     1   stressNew(i,j)-stresskk/3.0)+coef3*(stressOld(i,j)-
     1   oldstresskk/3.0)+g1/eta0*veint(j)-2*g1*evisco(j))/coef2
260        continue
      do 265 j=ndir+1,ntens
         devisco(j)=(0.5*coef1*(stressOld(i,j)+stressNew(i,j))+
     1              coef3*stressOld(i,j)+g1/eta0*veint(j)-
     1                        2*g1*evisco(j))/coef2
265        continue
C
C STORE STATE VARIABLE ARRAY
C
       do 300 j=1,ndir
          stateNew(i,j)=eelas(j)+strainInc(i,j)-dstrankk/3.0-devisco(j)-
     1             deplas(j)
          stateNew(i,j+ntens)=eplas(j)+deplas(j)
          stateNew(i,j+3+2*ntens)=evisco(j)+devisco(j)
         stateNew(i,j+3+3*ntens)=veint(j)+0.5*dt*(stressOld(i,j)-
       1            oldstresskk/3.0+stressNew(i,j)-stresskk/3.0)
300        continue
do 310 j=ndir+1,ntens
       stateNew(i,j)=eelas(j)+strainInc(i,j)/2.0-devisco(j)-deplas(j)
         stateNew(i,j+ntens)=eplas(j)+deplas(j)
         stateNew(i,j+3+2*ntens)=evisco(j)+devisco(j)
       stateNew(i,j+3+3*ntens)=veint(j)+0.5*dt*(stressOld(i,j)+
       1                                  +stressNew(i,j))
310  continue
     stateNew(i,1+2*ntens)=eqplas_shr
     stateNew(i,2+2*ntens)=eqplas_crz
     stateNew(i,3+2*ntens)=vplas
       stateNew(i,4*ntens+4)=c_factor
```

```
   if(c_factor .LT. 1.0E-4) then
         stateNew(i,4*ntens+5)=zero
       else
        stateNew(i,4*ntens+5)=one
       endif
350  continue
C
     return
     end

C
C     CALCULATE EQUIVALENT STRESS
     SUBROUTINE AHARD(SYIELD,HARD,EQPLAS,TABLE,NVALUE)
C
     INCLUDE 'ABA_PARAM.INC'
     DIMENSION TABLE(2,NVALUE)
C
C    SET YIELD STRESS TO LAST VALUE OF TABLE, HARDENING TO ZERO
     SYIELD=TABLE(1,NVALUE)
     HARD=0.0
C   IF MORE THAN ONE ENTRY, SEARCH TABLE
C
     IF(NVALUE.GT.1) THEN
       DO 10 K1=1,NVALUE-1
         EQPL1=TABLE(2,K1+1)
         IF(EQPLAS.LT.EQPL1) THEN
           EQPL0=TABLE(2,K1)
           IF(EQPL1.LE.EQPL0) THEN
             WRITE(6,1)
1            FORMAT(//,30X,'***ERROR - PLASTIC STRAIN MUST BE ',
    1               'ENTERED IN ASCENDING ORDER')
C              CALL XIT
            ENDIF
C           CURRENT YIELD STRESS AND HARDENING
           DEQPL=EQPL1-EQPL0
           SYIEL0=TABLE(1,K1)
           SYIEL1=TABLE(1,K1+1)
           DSYIEL=SYIEL1-SYIEL0
           HARD=DSYIEL/DEQPL
           SYIELD=SYIEL0+(EQPLAS-EQPL0)*HARD
           GOTO 20
           ENDIF
10         CONTINUE
20         CONTINUE
     ENDIF
     RETURN
     END
```

```
C    ROUNTINE TO CALCULATE EIGENVALUES AND EIGENVECTORS
       SUBROUTINE PRINCIPAL(S,PS,V,NDIR,NSHR,TL)
C        IMPLICIT REAL*8 (A-H,O-Z)

       DIMENSION A(NDIR,NDIR),V(NDIR,NDIR),S(NDIR+NSHR),PS(NDIR)

       NEQ=NDIR
C    EIGENVALUE SOLUTION BY JACOBI METHOD -
C    A - MATRIX (ANY RANK) TO BE SOLVED ---
C        EIGENVALUES ON DIAGONAL
C    V - MATRIX OF EIGENVECTORS PRODUCED
C    TL- NUMBER OF SIGNIFICANT FIGURES
C---- INITIALIZATION ----------------------
     ZERO = 0.0D0
     SUM = ZERO
     TOL = ABS(TL)
      A(1,1)=S(1)
      A(2,2)=S(2)
      A(3,3)=S(3)
     A(1,2)=S(NDIR+1)
      A(2,1)=S(NDIR+1)
      IF(NSHR .GT. 1) THEN
      A(1,3)=S(NDIR+3)
      A(3,1)=S(NDIR+3)
      A(2,3)=S(NDIR+2)
      A(3,2)=S(NDIR+2)
      ENDIF
C---- SET INITIAL EIGENVECTORS -------------
     DO 200 I=1,NEQ
      DO 190 J=1,NEQ
       IF (TL.GT.ZERO) V(I,J) = ZERO
190      SUM = SUM + ABS(A(I,J))
     IF (TL.GT.ZERO) V(I,I) = 1.0
200  CONTINUE
C---- CHECK FOR TRIVIAL PROBLEM ------------
     IF (NEQ.EQ.1) RETURN
      IF (SUM.LE.ZERO) RETURN
      SUM = SUM/FLOAT(NEQ*NEQ)
C-------------------------------------------
C---- REDUCE MATRIX TO DIAGONAL ------------
C-------------------------------------------
400  SSUM = ZERO
     AMAX = ZERO
     DO 700 J=2,NEQ
     IH = J-1
     DO 700 I=1,IH
C---- CHECK IF A(I,J) IS TO BE REDUCED -----
```

```
       AA = ABS(A(I,J))
      IF (AA.GT.AMAX) AMAX = AA
      SSUM = SSUM + AA
      IF (AA.LT.0.1*AMAX) GO TO 700
C---- CALCULATE ROTATION ANGLE ----------
      AA=ATAN2(2.0*A(I,J),A(I,I)-A(J,J))/2.0
      SI = SIN(AA)
      CO = COS(AA)
C---- MODIFY "I" AND "J" COLUMNS --------
      DO 500 K=1,NEQ
      TT = A(K,I)
      A(K,I) = CO*TT + SI*A(K,J)
      A(K,J) = -SI*TT + CO*A(K,J)
      TT = V(K,I)
      V(K,I) = CO*TT + SI*V(K,J)
500   V(K,J) = -SI*TT + CO*V(K,J)
C---- MODIFY DIAGONAL TERMS -------------
      A(I,I) = CO*A(I,I) + SI*A(J,I)
      A(J,J) =-SI*A(I,J) + CO*A(J,J)
      A(I,J) = ZERO
C---- MAKE "A" MATRIX SYMMETRICAL -------
      DO 600 K=1,NEQ
      A(I,K) = A(K,I)
      A(J,K) = A(K,J)
600   CONTINUE
C---- A(I,J) MADE ZERO BY ROTATION ------
700   CONTINUE
C---- CHECK FOR CONVERGENCE -------------
      IF(ABS(SSUM)/SUM .GT.TOL)GO TO 400
        DO 900 I=1,NDIR
          PS(I)=A(I,I)
900       CONTINUE
      RETURN
      END
```

```
C**********************************************************************
      SUBROUTINE ROTTENSOR(TENSOR,DR,NDIR,NSHR)
C     ROTATE A TENSOR:  TENSOR=DR.TENSOR.trans(DR)
C     TENSOR IS STORED IN A VETOR(NDIR+NSHR)
C**********************************************************************
C      IMPLICIT REAL*8(A-H,O-Z)
       DIMENSION TENSOR(NDIR+NSHR),DR(NDIR,NDIR)
       DIMENSION STENSOR(3,3),TEMP(3,3),TDR(3,3)
       CALL TRANS(DR,TDR)
       CALL GETU(TENSOR,STENSOR,NDIR,NSHR)
       CALL MUL(DR,STENSOR,TEMP,NDIR)
       CALL MUL(TEMP,TDR,STENSOR,NDIR)
C     REARRANGE AND STORE IN A VECTOR
      TENSOR(1)=STENSOR(1,1)
       TENSOR(2)=STENSOR(2,2)
       TENSOR(3)=STENSOR(3,3)
       TENSOR(4)=STENSOR(1,2)
       TENSOR(5)=STENSOR(2,3)
       TENSOR(6)=STENSOR(1,3)
     RETURN
       END

C**********************************************************************
      SUBROUTINE GETDR(FO,FN,DR)
C     CALCULATE DELTA_R  DF=DR.DU
C     DU=TRANSPOSE(DU)   DR.TRANSPOSE(DR)=I
C**********************************************************************
C      IMPLICIT REAL*8(A-H,O-Z)
       DIMENSION FOLD(6),FNEW(6),DR(3,3)
     DIMENSION FO(3,3),FN(3,3),FOINV(3,3),DF(3,3),DC(3,3),TRANSDF(3,3)
       DIMENSION V(3,3),DU(3,3),DUINV(3,3)
       CALL GETF(FOLD,FO,3,3)
       CALL GETF(FNEW,FN,3,3)
C     FOLD^-1
     CALL KMINV(FO,FOINV,DET)
C     DF=FNEW.FOLD^-1
     CALL MUL(FN,FOINV,DF,3)
C     TRANSPOSE(DF)
     CALL TRANS(DF,TRANSDF)
C     CALCULATE TRANSPOSE(DF).DF
     CALL MUL(TRANSDF,DF,DC,3)
C     CALCULATE THE EIGENVALUES AND EIGENVECTORS OF DC
     CALL EIGEN(DC,V,3,1.0e-6)
C     CALCULATE DU
```

```
      DO 20 I=1,3
        DO 10 J=1,3
          DU(I,J)=SQRT(DC(1,1))*V(I,1)*V(J,1)+
     1              SQRT(DC(2,2))*V(I,2)*V(J,2)+
     1           SQRT(DC(3,3))*V(I,3)*V(J,3)
10         CONTINUE
20    CONTINUE
C     CLACULATE DU^-1
      CALL KMINV(DU,DUINV,DET)
C     DR=DF.DU^-1
      CALL MUL(DF,DUINV,DR,3)
      RETURN
      END

C*****************************************************************
      SUBROUTINE EIGEN(A,V,NEQ,TL)
C      IMPLICIT REAL*8 (A-H,O-Z)
      DIMENSION A(NEQ,NEQ),V(NEQ,NEQ)
C     EIGENVALUE SOLUTION BY JACOBI METHOD -
C     A --MATRIX (ANY RANK) TO BE SOLVED ---
C        EIGENVALUES ON DIAGONAL
C     V - MATRIX OF EIGENVECTORS PRODUCED
C     TL- NUMBER OF SIGNIFICANT FIGURES
C---- INITIALIZATION ----------------------
      ZERO = 0.0D0
      SUM = ZERO
      TOL = ABS(TL)
C---- SET INITIAL EIGENVECTORS -------------
      DO 200 I=1,NEQ
       DO 190 J=1,NEQ
       IF (TL.GT.ZERO) V(I,J) = ZERO
190    SUM = SUM + ABS(A(I,J))
      IF (TL.GT.ZERO) V(I,I) = 1.0
200   CONTINUE
C---- CHECK FOR TRIVIAL PROBLEM -----------
      IF (NEQ.EQ.1) RETURN
      IF (SUM.LE.ZERO) RETURN
      SUM = SUM/FLOAT(NEQ*NEQ)
C-----------------------------------------
C---- REDUCE MATRIX TO DIAGONAL ------------
C-----------------------------------------
400   SSUM = ZERO
      AMAX = ZERO
      DO 700 J=2,NEQ
      IH = J -1
      DO 700 I=1,IH
C---- CHECK IF A(I,J) IS TO BE REDUCED -----
```

```
      AA = ABS(A(I,J))
      IF (AA.GT.AMAX) AMAX = AA
      SSUM = SSUM + AA
      IF (AA.LT.0.1*AMAX) GO TO 700
C---- CALCULATE ROTATION ANGLE ----------
      AA=ATAN2(2.0*A(I,J),A(I,I)-A(J,J))/2.0
      SI = SIN(AA)
      CO = COS(AA)
C---- MODIFY "I" AND "J" COLUMNS --------
       DO 500 K=1,NEQ
        TT = A(K,I)
        A(K,I) = CO*TT + SI*A(K,J)
        A(K,J) = -SI*TT + CO*A(K,J)
        TT = V(K,I)
        V(K,I) = CO*TT + SI*V(K,J)
500     V(K,J) = -SI*TT + CO*V(K,J)
C---- MODIFY DIAGONAL TERMS -------------
        A(I,I) = CO*A(I,I) + SI*A(J,I)
        A(J,J) =-SI*A(I,J) + CO*A(J,J)
        A(I,J) = ZERO
C---- MAKE "A" MATRIX SYMMETRICAL -------
      DO 600 K=1,NEQ
        A(I,K) = A(K,I)
        A(J,K) = A(K,J)
600   CONTINUE
C---- A(I,J) MADE ZERO BY ROTATION ------
700   CONTINUE
C---- CHECK FOR CONVERGENCE -------------
      IF(ABS(SSUM)/SUM .GT.TOL)GO TO 400

      RETURN
      END
C*****************************************************************
       SUBROUTINE KMINV(A,AINV,DET_AINV)
C        calculates the inverse of a {3 x 3} matrix and the
C        determinant of the inverse
C*****************************************************************
C      IMPLICIT REAL*8(A-H,O-Z)

       DIMENSION A(3,3), AINV(3,3)


       PARAMETER(ZERO=0.D0, ONE=1.D0)

       DET_A = A(1,1)*(A(2,2)*A(3,3) - A(3,2)*A(2,3)) -
     +             A(2,1)*(A(1,2)*A(3,3) - A(3,2)*A(1,3)) +
     +             A(3,1)*(A(1,2)*A(2,3) - A(2,2)*A(1,3))
```

```
          IF (DET_A .LE. ZERO) THEN
         WRITE(80,*) 'WARNING: DET OF MAT IS ZERO/NEGATIVE !!'
        ENDIF

        DET_AINV = ONE/DET_A

        AINV(1,1) = DET_AINV*(A(2,2)*A(3,3) - A(3,2)*A(2,3))
        AINV(1,2) = DET_AINV*(A(3,2)*A(1,3) - A(1,2)*A(3,3))
        AINV(1,3) = DET_AINV*(A(1,2)*A(2,3) - A(2,2)*A(1,3))
        AINV(2,1) = DET_AINV*(A(3,1)*A(2,3) - A(2,1)*A(3,3))
        AINV(2,2) = DET_AINV*(A(1,1)*A(3,3) - A(3,1)*A(1,3))
        AINV(2,3) = DET_AINV*(A(2,1)*A(1,3) - A(1,1)*A(2,3))
        AINV(3,1) = DET_AINV*(A(2,1)*A(3,2) - A(3,1)*A(2,2))
        AINV(3,2) = DET_AINV*(A(3,1)*A(1,2) - A(1,1)*A(3,2))
        AINV(3,3) = DET_AINV*(A(1,1)*A(2,2) - A(2,1)*A(1,2))

        RETURN
        END

C*****************************************************************
      SUBROUTINE MUL(A,B,C,N)
C MULTIPLICATION OF SQUARE MATRIX A,B. THE RSULTE IS STORED IN C
C N IS THE DIMENSION OF THE MATRIX
C*****************************************************************
C     IMPLICIT REAL*8(A-H,O-Z)
      DIMENSION A(N,N),B(N,N),C(N,N)
        DO 30 I=1,N
          DO 20 J=1,N
            C(I,J)=0
           DO 10 K=1,N
              C(I,J)=C(I,J)+A(I,K)*B(K,J)
10            CONTINUE
20    CONTINUE
30   CONTINUE

      RETURN
        END

C*********************************************************************
      SUBROUTINE TRANS(A,ATRANS)
C       THIS SUBROUTINE CALCULATES THE TRANSPOSE OF AN 3 BY 3
C       MATRIX [A], AND PLACES THE RESULT IN ATRANS.
C*********************************************************************
C       REAL*8 A(3,3),ATRANS(3,3)
      dimension A(3,3),ATRANS(3,3)
        DO 1 I=1,3
         DO 2 J=1,3
```

```
            ATRANS(J,I) = A(I,J)
  2         CONTINUE
  1  CONTINUE
       RETURN
       END
C***********************************************************
      SUBROUTINE GETF(F,SF,NDIR,NSHR)
C     REARRANGE DEFORMATION GRADIENT
C***********************************************************
C      IMPLICIT REAL*8(A-H,O-Z)
      DIMENSION F(NDIR+2*NSHR),SF(NDIR,NDIR)
      IF (NSHR .LT. 3) THEN
        WRITE(80,*) 'WARNING: CAN ONLY BE USED IN 3D MODEL '
       ENDIF
       SF(1,1)=F(1)
       SF(1,2)=F(4)
       SF(1,3)=F(9)
       SF(2,1)=F(7)
       SF(2,2)=F(2)
       SF(2,3)=F(5)
       SF(3,1)=F(6)
       SF(3,2)=F(8)
       SF(3,3)=F(3)
       RETURN
       END
C***********************************************************
      SUBROUTINE GETU(U,SU,NDIR,NSHR)
C     REARRANGE STRETCH TENSOR
C***********************************************************
C      IMPLICIT REAL*8(A-H,O-Z)
      DIMENSION U(NDIR+NSHR),SU(NDIR,NDIR)
      IF (NSHR .LT. 3) THEN
        WRITE(80,*) 'WARNING: CAN ONLY BE USED IN 3D MODEL '
       ENDIF
       SU(1,1)=U(1)
       SU(1,2)=U(4)
       SU(1,3)=U(6)
       SU(2,1)=U(4)
       SU(2,2)=U(2)
       SU(2,3)=U(5)
       SU(3,1)=U(6)
       SU(3,2)=U(5)
       SU(3,3)=U(3)
       RETURN
       END
```

APPENDIX B

This appendix contains the brief introduction of mechanical modeling of stick-slip mechanism during scratch process. As presented in Chapter VII, the periodic occurrence of scratch damage regardless of the type of polymer is the result of the stick-slip phenomenon when the indenter experiences periodic changes in resistance during its movement [39-41,50].

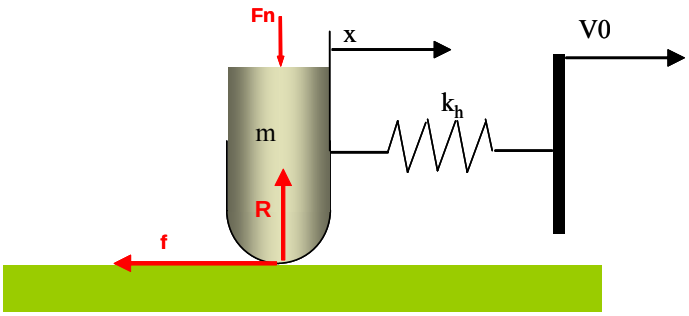

Fig. B.1. Simple mechanical model of scratch system.

A simple mechanical model of scratch system is shown in Fig. B.1. Here, the test head which is connected to scratch tip via an effective spring system with stiffness k_h, moves at constant velocity V_0. m is the total mass of scratch tip. F_n is the applied scratch normal load and f is the resistance force at tangential direction. The force balance equations are:

$$k_h(V_0 t - x) - f = mx$$
$$R \equiv Fn \qquad \text{(B.1)}$$

Obviously, at stick stage, $x = x = x = 0$. The resistance force f equals to the static friction force($\mu_s F_n$). The initial instance of slip then can be obtained:

$$t = t_0 = \frac{\mu_s F_n}{k_h V_0} \tag{B.2}$$

At slip stage, f equals to the kinetic friction force($\mu_k F_n$). The motion equation now is:

$$mx + k_h x = k_h V_0 t - \mu_k F_n$$

$$x + \omega^2 x = \omega^2 V_0 t - Q \tag{B.3}$$

here $\omega^2 = \frac{k_h}{m}; Q = \frac{\mu_k F_n}{m}$, the general solution of this equation is :

$$x = C_1 \cos \omega t + C_2 \sin \omega t + V_0 t - \frac{Q}{\omega^2} \tag{B.4}$$

Considering the initial condition $x = x = 0$ at $t = t_0 = \frac{\mu_s F_n}{k_h V_0}$ and t-t0<<1, the solution of the motion equation is:

$$k_h (V_0 t - x) = \mu_k F_n + (\mu_s - \mu_k) F_n \cos(\omega (t - t_0)) \tag{B.5}$$

It can be found that the tangential force (Ft) oscillates between μsFn and (2μk-μs)Fn. The amplitude is 2(μs-μk)*Fn. The frequency of stick-slip, depends on the effective spring constant/stiffness, scratch velocity, normal load level and the effective mass of the scratch tip.

$$T = \frac{2(\mu_s - \mu_k) F_n}{k_h V_0}, \qquad \omega = \sqrt{\frac{k_h}{m}} \tag{B.6}$$

The moving distance of each stick-slip cycle, i.e., fish-scales should increase with larger effective mass of the scratch tip or higher normal load. A simple test was

conducted to validate this. Without modification of test machine, the mass of scratch tip was altered and same velocity was used in the progressive increasing normal load scratch test. Then the distance between two adjunct fish-scale was measured. As shown in Fig. B.2, a larger effective tip mass leads to a lower stick-slip frequency, thus lager amplitude of the distance between two adjunct fish-scale. Stick-slip time period is also found to be proportional to the normal load level.

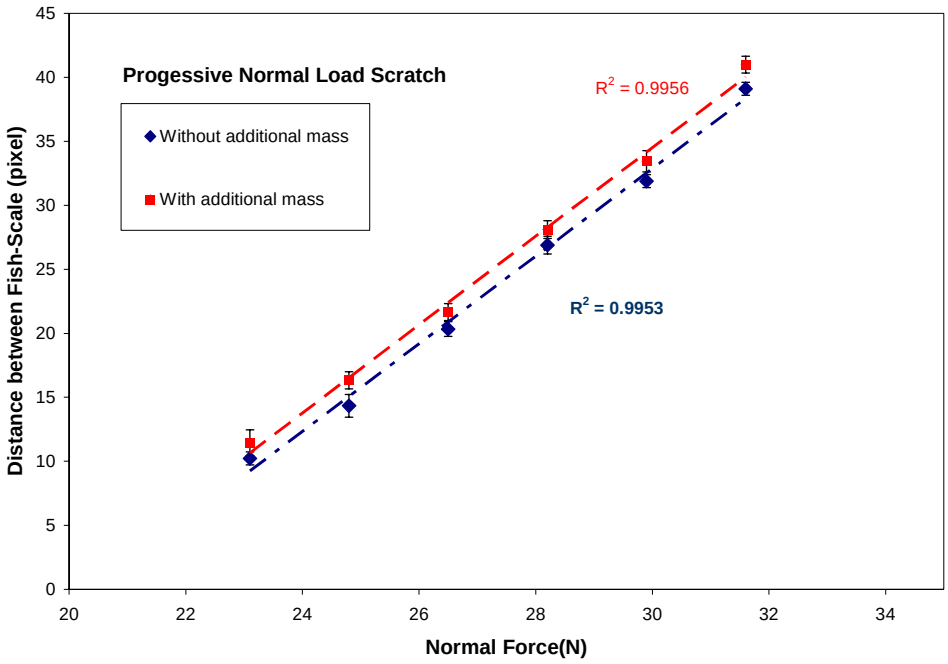

Fig. B.2. Effect of normal load and tip mass on stick-slip time period.

In above discussion, no vertical degree of freedom is included. In the actual stick-slip phenomena, it plays an important role since the scratch tip may lose its full contact to underneath surface, especially when the vertical effective stiffness is involved which is the main difference between a dead-load and a load-controlled test method. Furthermore, the geometric shape and size of the scratch tip also has a significant effect

on resistance force. With all those factors considered, a more realistic mechanical model for stick-slip can be constructed which can provide fundamental understanding of scratch behavior under various conditions.

APPENDIX C

This appendix contains the brief introduction of an automated Quantitative Scratch Visibility Determination method. The new proposed approach utilizes relevant optical parameters based on human physiology to alleviate biases arising from human observers and environment.

Currently, there is no generally accepted methodology to quantify the onset of visibility of polymer scratched surfaces. The observers' judgment is based on a combination of numerous complex visual clues and prior experience with little understanding of the optical processes involved. Many factors, including environment light condition, the lighting angle, and distance from sample to inspectors' eye, just to name a few, can significantly bias the observation without even mentioning the different eye acuteness of individual observers.

The algorithm of automated determination of onset scratch visibility (ASV) method with minimal human intervention is discussed. The principle underlying ASV technology is based on biological knowledge of human eye's visual recognition process. People are more sensitive to sharp contrast rather than in absolute brightness levels. The contrast sensitivity is defined as follows [87],

$$C_{ontrast} = \frac{B_o - B_b}{B_o + B_b} \times 100\ \% \tag{C.1}$$

Here B_o and B_b are the brightness values of the object and background, respectively. An object becomes visible when its contrast satisfies sensitivity criterion, which is 2% for the sharpest human eyes [87].

While the contrast sensitivity criterion is enough for dark samples, different substrate colors can obscure visual inspection on polymer scratch visibility even having the same material and contrast criterion. For example, the green surface generally shows a lower load onset of scratch visibility, when compared to the red one when other conditions are the same. The color bias is from the varying color sensitivity of retina cells in human eyes to different light wavelengths (i.e., green color is more sensitive than red one). To address the influence of color on contrast values, the brightness of the sample surfaces can be calculated as follows [88],

$$Brightness = R \times 0.299 + G \times 0.587 + B \times 0.114 \tag{C.2}$$

Here R, G and B are the intensity level of red, green and blue color component, respectively.

In viewing a scratch, the size of the scratch is important, too. The visual acuity is the ability to resolve a spatial pattern separated by a visual angle (θ), which is about 1/60º for normal human eyes [89]. With a typical inspection distance of 12 inches from the eyes to the inspected samples, the minimal visible size for typical human eyes is about 90 μm. Anything smaller than this size is not detectable even it satisfies the contrast sensitivity criterion.

Due to its dynamic nature, the stick-slip phenomena at low loads caused by the transition from static to dynamic movement of the indenter head is commonly found on scratched polymer surfaces. This discontinuous mode of scratch cannot be counted as the onset of scratch visibility. Additionally, presence of dust particles along the scratch path and irregular surface roughness can also induce discontinuity in scratch pattern. The

continuity criterion for onset scratch visibility is therefore introduced to remove these discrete visible scratches for polymer scratch resistance evaluation. The scratch pattern has to satisfy this criterion to qualify as continuous visible scratch. For typical flat, smooth and low gloss substrate, the continuity criterion is chosen to be 90% in a range of 2mm of consecutive scratch path length. Here, twice the diameter of the scratch tip is adopted as the measurement range.

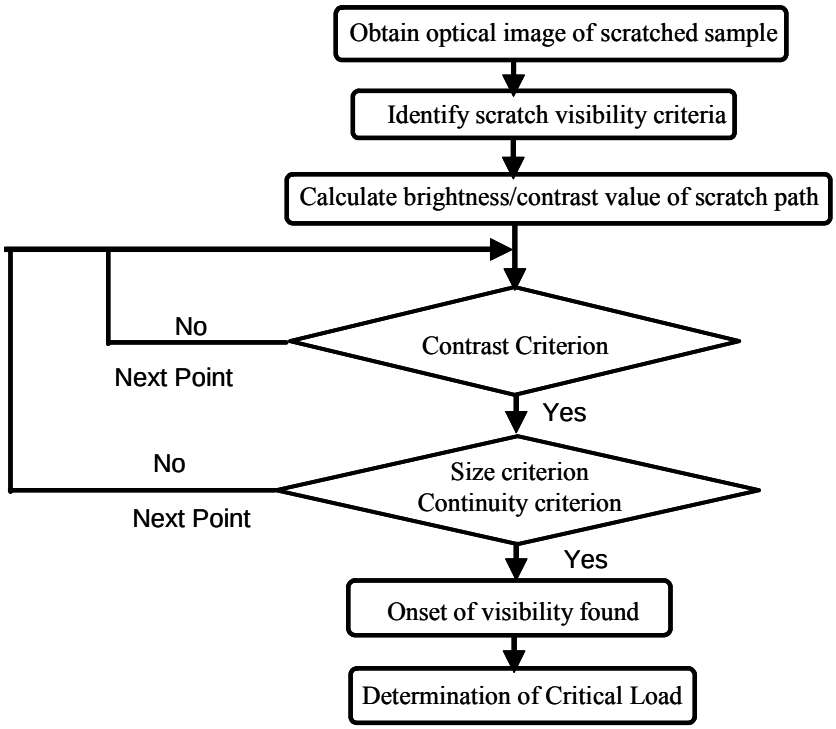

Fig. C.1. Flowing chart of auto-determination of onset of scratch visibility

Based on the above discussion, the onset of scratch visibility is the very first point on the scratch path that satisfies the contrast, size and continuity criteria at the same time. Once the optical image of scratched sample is obtained, logical steps, as illustrated via the flow chart shown in Fig. C.1, can be applied to locate the onset of

scratch visibility. A new Auto-determination of Scratch Visibility (ASV©) [90] software was developed according to this algorithm and adopted to locate the onset of scratch visibility of typical polymer surfaces.

Independent of the sample attributes (gloss, color, and texture) and inspection attributes (light source and distance), this new ASV methodology can consistently and reliably obtain quantitative scratch resistance values of polymers in an objective manner. Considering the optical evaluation criterion adopted for mar/abrasion resistance evaluation, this methodology can be easily developed to evaluate polymer mar/abrasion performance with some modifications.

VITA

Mr. Han Jiang had his early education in his home country. Mr. Han Jiang earned his Bachelor of Engineering in engineering mechanics with honors from Chongqing University, China in 1992. Mr. Jiang continued his graduate research under Professor Zhang in the same university in a study "Asymmetric Constitutive and Structure Relationships of Biocomposites" and earned his Master of Engineering in solid mechanics in 1995. He worked in China, France and the USA before his Ph.D. graduate research under Professor Sue at Texas A&M University.

Mr. Jiang's contact address is: Polymer Technology Center, Department of Mechanical Engineering, Texas A&M University, College Station, TX, 77843 USA. His email address is: jianghantamu@gmail.com.